

See discussions, stats, and author profiles for this publication at: <https://www.researchgate.net/publication/226340056>

SQUID magnetometers for low-frequency applications

Article in Journal of Low Temperature Physics · September 1989

DOI: 10.1007/BF00681735

CITATIONS
194

READS
608

4 authors, including:



Tapani Ryhänen

Emberion Oy

80 PUBLICATIONS 5,926 CITATIONS

[SEE PROFILE](#)



Heikki Seppä

VTT Technical Research Centre of Finland

255 PUBLICATIONS 4,478 CITATIONS

[SEE PROFILE](#)



Risto J Ilmoniemi

Aalto University

473 PUBLICATIONS 30,131 CITATIONS

[SEE PROFILE](#)

Some of the authors of this publication are also working on these related projects:



Time constants and length constants in the brain [View project](#)



Navigated Transcranial Magnetic Stimulation in Neurosurgery [View project](#)

SQUID Magnetometers for Low-Frequency Applications

Tapani Ryhänen and Heikki Seppä

*Metrology Research Institute, Helsinki University of Technology
and Technical Research Centre of Finland, Espoo, Finland*

and

Risto Ilmoniemi and Jukka Knuutila

Low Temperature Laboratory, Helsinki University of Technology, Espoo, Finland

(Received March 16, 1989)

We present a novel formulation for SQUID operation, which enables us to evaluate and compare the sensitivity and applicability of different devices. SQUID magnetometers for low-frequency applications are analyzed, taking into account the coupling circuits and electronics. We discuss nonhysteretic and hysteretic single-junction rf SQUIDS, but the main emphasis is on the dynamics, sensitivity, and coupling considerations of dc-SQUID magnetometers. A short review of current ideas on thin-film, dc-SQUID design presents the problems in coupling and the basic limits of sensitivity. The fabrication technology of tunnel-junction devices is discussed with emphasis on how it limits critical current densities, specific capacitances of junctions, minimum linewidths, conductor separations, etc. Properties of high-temperature superconductors are evaluated on the basis of recently published results on increased flux creep, low density of current carriers, and problems in fabricating reliable junctions. The optimization of electronics for different types of SQUIDS is presented. Finally, the most important low-frequency applications of SQUIDS in biomagnetism, metrology, geomagnetism, and some physics experiments demonstrate the various possibilities that state-of-the-art SQUIDS can provide.

CONTENTS

1. Introduction
2. Basic Phenomena in Josephson Devices
 - 2.1. Model of the Josephson Junction
 - 2.2. Quantization of Magnetic Flux
3. Single-Junction (rf) SQUIDS
 - 3.1. General

- 3.2. rf SQUID in the Nonhysteretic Mode: The Inductive SQUID
 - 3.2.1. Introduction
 - 3.2.2. Operation of the Inductive SQUID
 - 3.2.3. Noise in the Inductive SQUID
 - 3.2.4. Discussion
- 3.3. rf SQUID in the Hysteretic Mode
 - 3.3.1. Operation of the rf SQUID in the Dissipative Regime
 - 3.3.2. Noise in the Hysteretic rf SQUID
 - 3.3.3. Discussion
- 3.4. rf SQUID in the High-Frequency Regime
 - 3.4.1. Introduction
 - 3.4.2. Operation of the Microwave SQUID
 - 3.4.3. Discussion
- 3.5. Resistive rf SQUID
 - 3.5.1. Introduction
 - 3.5.2. Theory of Operation
 - 3.5.3. Noise Properties of the R-SQUID
 - 3.5.4. Discussion
- 4. Double-Junction (dc) SQUIDs
 - 4.1. Operation
 - 4.1.1. Model of an Autonomous dc SQUID
 - 4.1.2. Simplified Model of the dc SQUID
 - 4.1.3. Dynamics of the dc SQUID
 - 4.1.4. Effect of Thermal Noise
 - 4.1.5. Energy Resolution of the Autonomous dc SQUID
 - 4.1.6. Sensitivity of the dc SQUID Magnetometer
 - 4.2. Problems with Practical Devices
 - 4.2.1. Origins of Parasitic Effects
 - 4.2.2. Model for Practical dc SQUIDs
 - 4.2.3. Effect of Parasitic Capacitances
 - 4.3. The State of the Art of dc SQUIDs
 - 4.3.1. General
 - 4.3.2. Square-Washer dc SQUID
 - 4.3.3. Capacitively Shunted dc SQUID
 - 4.3.4. Resistively Shunted dc SQUID
 - 4.3.5. Inductively Shunted dc SQUID
 - 4.3.6. Multiloop dc SQUID
 - 4.3.7. dc SQUID with a Matching Transformer
 - 4.3.8. Optimized dc SQUID
- 5. Fabrication of Tunnel-Junction SQUIDs: Limitations to the Design
 - 5.1. Materials
 - 5.2. Film Deposition and Patterning

- 5.3. Formation of the Junction Barrier
- 5.4. Discussion
- 6. SQUIDs Made of High-Temperature Superconductors
 - 6.1. General
 - 6.2. Examples of Existing High- T_c SQUIDs
 - 6.3. Noise in High- T_c SQUIDs
 - 6.4. Discussion
- 7. Electronics
 - 7.1. General
 - 7.2. rf SQUID in the Hysteretic Mode
 - 7.3. rf SQUID in the Nonhysteretic Regime
 - 7.4. Microwave SQUID
 - 7.5. dc SQUID
- 8. Comparison of Different Types of SQUIDs: Performance Limits
 - 8.1. Main Features
 - 8.2. Fundamental Constraints of the SQUID Response
 - 8.3. Practical Constraints Set by Electronics
 - 8.4. 1/f Noise
- 9. Applications
 - 9.1. Biomagnetic Applications
 - 9.2. Metrology
 - 9.3. Other Applications
 - 9.3.1. Geomagnetism
 - 9.3.2. Accelerometers, Gravimeters, Displacement Sensors
 - 9.3.3. Monopole Detectors
 - 9.3.4. Other Physical Experiments
- 10. Conclusions

1. INTRODUCTION

The Superconducting QUantum Interference Device (SQUID), formed by interrupting a superconducting ring by one or more Josephson junctions, has made a significant impact on experimental physics, precision metrology, and biomagnetic measurements.^{1-7,*} SQUIDs have been studied intensively both theoretically and experimentally after the first analysis of a double-junction interferometer by Jaklevic *et al.*,^{8,9} the construction of the SLUG and the first dc SQUIDs by Clarke and his coworkers,¹⁰⁻¹² and, particularly, after the invention of the rf SQUID by Silver and Zimmerman.¹³ SQUID research has recently made a comeback, due to the discovery of high-temperature superconductivity by Bednorz and Müller.¹⁴ In our companion paper,¹⁵ we discuss recent developments in devices having several SQUIDs operating simultaneously.

*See also the recent review by Koch.⁴²⁸

In this article, several different types of SQUIDS are briefly reviewed, a novel formulation of their operation is presented, and problems associated with their use are discussed. Both the dynamics of and the noise in all types of SQUIDS are well understood and widely discussed in the literature. However, in spite of their outstanding properties as magnetic sensors and null-detectors, with many straightforward applications, SQUIDS have had only a modest impact outside research laboratories. Problems due to the need for low temperatures, the complicated dynamics, and the lack of natural damping often discourage the use of SQUIDS in practical applications.

Most studies of SQUID dynamics are based on the resistively shunted junction (RSJ) model for the Josephson contact. In addition to the RSJ model in weak links and tunnel junctions, we discuss flux quantization in superconducting rings before the treatment of complete SQUIDS. Since the dynamics of the nonhysteretic rf SQUID is easy to understand on the basis of the RSJ model, it is presented first. After having introduced the hysteretic rf SQUID, properties of the microwave SQUID are briefly discussed. The resistive, nonhysteretic SQUID, which is used for determining the absolute temperature, follows next. Because of the popularity of dc SQUIDS, our main emphasis is on their dynamics. Advantages and disadvantages of specific SQUID types are discussed at the end of each section; the most important applications are mentioned as well.

To facilitate the evaluation of the different SQUID types as low-frequency magnetic field sensors, we introduce figures-of-merit, such as signal bandwidth, intrinsic and extrinsic energy sensitivity, and energy-to-power conversion efficiency.

Although the Josephson junction in a SQUID can be a microbridge, a point contact, or a tunnel junction, only the parameters of resistively shunted tunnel junctions are sufficiently well controlled for complete device optimization. Therefore, only the fabrication of tunnel-junction SQUIDS is discussed. High- T_c materials and their applications are treated next; we focus on the most important results and on general problems in the design and fabrication of low-noise high- T_c magnetometers. The design of electronics is discussed. Before examples of applications, a comparison of different types of SQUIDS is summarized, and the performance limits are analyzed.

2. BASIC PHENOMENA IN JOSEPHSON DEVICES

2.1. Model of the Josephson Junction

Soon following the development of the microscopic theory of superconductivity by Bardeen, Cooper, and Schrieffer (BCS theory),¹⁶ Josephson¹⁷

predicted the existence and properties of Cooper-pair tunneling between two superconductors that are separated by a thin insulating barrier. When a voltage V is applied across this junction and the transmission coefficient for quasiparticles (normal electrons) is small, the current is¹⁷⁻²⁰

$$I = I_c \sin \theta + (\sigma_0(V, T) + \sigma_1(V, T) \cos \theta) V \quad (1)$$

where I_c and θ are the critical current and the phase difference of the junction, respectively. σ_0 and σ_1 are voltage- and temperature-dependent conductivities. The term $I_c \sin \theta$ determines the basic properties of the junction. Josephson also predicted that V is proportional to the time derivative of the phase difference¹⁷

$$V = \frac{\hbar}{2e} \frac{d\theta}{dt} \quad (2)$$

This is the ac Josephson effect. Experiments^{8,21-27} soon showed that the behavior of many different types of junctions can be described by Eqs. (1) and (2). The early history of the Josephson effect has been reviewed by Lowell.²⁸

From Eqs. (1) and (2),

$$I = I_c \sin \theta + R_q^{-1}(1 + \kappa \cos \theta) \frac{\hbar}{2e} \frac{d\theta}{dt} \quad (3)$$

where $R_q = \sigma_0^{-1}$ is the quasiparticle resistance, and $\kappa = \sigma_1/\sigma_0$. Several groups^{26,29-35} have studied the magnitude of κ . I_c and κ are related to the BCS gap parameter $\Delta(T)$.^{18,30}

A useful model for Josephson junctions was independently suggested by McCumber³⁶ and by Stewart³⁷:

$$I = I_c \sin \theta + \frac{\hbar}{2e} \frac{1}{R} \frac{d\theta}{dt} + \frac{\hbar}{2e} C \frac{d^2\theta}{dt^2} + I_n \quad (4)$$

This is the resistively shunted junction (RSJ) model; C is the capacitance across the junction and R is the resistance formed by R_q in parallel with any external shunt resistance. Shunted tunnel junctions, where $R \ll R_q$ and κ is negligible, are accurately described by Eq. (4). I_n is the thermal noise current in the resistance; its autocorrelation function is $\langle I_n(t+\tau)I_n(t) \rangle = 2k_B T \delta(\tau)/R$, where $\delta(\tau)$ is the Dirac delta function. In dimensionless form, Eq. (4) reads

$$\beta_c \frac{d^2\theta}{dt^{*2}} + \frac{d\theta}{dt^*} = -\frac{d}{d\theta}(-i\theta - \cos \theta) + i_n(t^*) \quad (5)$$

where $t^* = (2\pi I_c R / \Phi_0)t$ and $\beta_c = 2\pi I_c R^2 C / \Phi_0$; $\Phi_0 = h/2e = 2.068 \cdot 10^{-15}$ Wb is the flux quantum, and β_c is called the Stewart-McCumber parameter.

Equation (5) is analogous to the equation of motion of a particle in a force field described by the potential energy $-i\theta - \cos \theta$. Parameter β_c is analogous to mass; it is inversely proportional to damping in the system. The Langevin function $i_n(t^*) = I_n/I_c$ describes the thermal noise; $\langle i_n(t^* + \tau^*) i_n(t^*) \rangle = 2\Gamma \delta(\tau^*)$, where $\Gamma = 2\pi k_B T / I_c \Phi_0$ is the normalized thermal energy.

The effect of thermal noise on the characteristics of the Josephson junction was first numerically analyzed by Kurkijärvi and Ambegaokar.³⁸ In Fig. 1 we present the dimensionless average voltage $\bar{v} = \langle v \rangle = \langle V \rangle / RI_c$ as a function of current through the junction. For the noiseless case ($\Gamma = 0$), the characteristics are hysteretic when^{36,37,39} $\beta_c > 0.7$: $\bar{v}(i)$ is double-valued when $i < 1$. In the nonhysteretic case, $\beta_c < 0.7$, only supercurrent exists when $i < 1$. Thermal noise causes a rounding in $\bar{v}(i)$ at the beginning of the voltage state. This is due to thermal activation^{40,41} and hopping between different voltage states^{38,42,43} (see Sec. 4.1.4). If β_c is large, the normalized dynamic resistance $\partial \bar{v} / \partial i$ is very large after the voltage state appears.

For point-contact junctions with no shunt resistance, it is necessary to augment the RSJ model with the $\cos \theta$ term of Eq. (3)^{30,34,35}

$$\beta_c \frac{d^2 \theta}{dt^{*2}} + (1 + \kappa \cos \theta) \frac{d\theta}{dt^*} = -\frac{d}{d\theta} (-i\theta - \cos \theta) + i_n(t^*) \quad (6)$$

When the $\cos \theta$ term is used to explain the properties of nonhysteretic point-contact rf SQUIDs and resistive rf SQUIDs, it improves the agreement

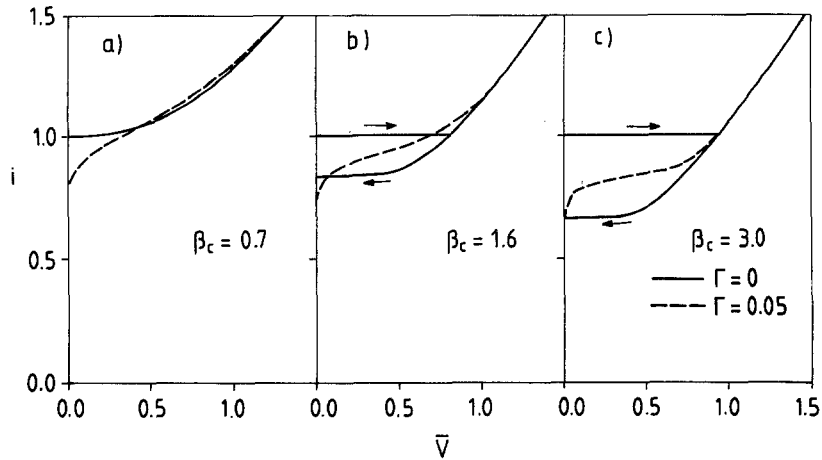


Fig. 1. Numerically calculated current-voltage characteristics of Josephson junctions with $\beta_c = 0.7, 1.6$, and 3.0 at zero temperature, i.e., $\Gamma = 0$ (solid lines), and with $\Gamma = 0.05$ (dashed lines).

of the model with experimental results.^{35,44,45} Furthermore, to avoid the discrepancy between the RSJ model and the observed leakage current at small voltages, a voltage-dependent normal resistance $R_n(V, T)$ is used.^{29,46–48} This so-called nonlinear-resistive model also improves the description of tunnel junctions that are poorly damped. Note that β_c , κ , and i_n in Eq. (6) are thus affected by the voltage and temperature dependence of the quasiparticle damping.

With expressions derived from the BCS theory for the normal current and the supercurrent, the so-called tunnel junction microscopic model^{49–54} gives a very accurate description. The microscopic theory also predicts how the junction current fluctuates.^{55–60} When $eV \ll k_B T$, thermal noise dominates; for high external voltage, the fluctuations are due to shot noise, determined by the Poisson process of the voltage-dependent arrival of electrons to the junction. At very low temperatures, with $\hbar\omega \gg k_B T$, quantum fluctuations are detected.

For the purpose of SQUID simulations, microscopic models are, however, too complex and time-consuming. In this article, we discuss only the thermal noise and the RSJ model, sometimes augmented with the $\cos \theta$ term. Josephson junction models have been reviewed by Likharev.^{4,61}

2.2. Quantization of Magnetic Flux

In Ginzburg–Landau theory, the macroscopic wave function for a superconductor is written as $\psi = \sqrt{n_s} e^{i\phi}$, where n_s is the density of Cooper pairs and ϕ is the phase. The integration of the supercurrent density $\mathbf{j} = (e\hbar/2im)[\psi^*\nabla\psi - \psi\nabla\psi^*] - (2e^2/m)|\psi|^2\mathbf{A}$ along a closed path \mathcal{L} around the ring containing a Josephson junction yields^{1,7}

$$\frac{2e}{\hbar}\Phi + \theta \equiv \frac{2e}{\hbar} \oint_{\mathcal{L}} \mathbf{A} \cdot d\mathbf{l} + \frac{2m}{n_s e \hbar} \int_{\text{junction}} \mathbf{j} \cdot d\mathbf{l} = n2\pi \quad (7)$$

where Φ is the flux in the ring, θ is the phase difference across the junction, and \mathbf{A} is the vector potential of the magnetic field \mathbf{B} , $\mathbf{B} = \nabla \times \mathbf{A}$. If $\theta = 0$, the circulating shielding current $I = I_c \sin \theta = 0$ and $\Phi = nh/2e = n\Phi_0$.

In general, $\Phi = \Phi_a + LI$, where Φ_a is the applied flux and L is the ring inductance. Combining Eqs. (1) and (7) and assuming that $d\Phi/dt = 0$, we can write an adiabatic expression

$$\Phi = \Phi_a - LI_c \sin(2\pi\Phi/\Phi_0) \quad (8)$$

or

$$\varphi = \varphi_a - \beta_L \sin \varphi \quad (9)$$

where $\varphi = 2\pi\Phi/\Phi_0$ and $\varphi_a = 2\pi\Phi_a/\Phi_0$ are the normalized total and applied fluxes enclosed by the SQUID ring, respectively; $\beta_L = 2\pi LI_c/\Phi_0$. Figure 2 shows Φ as a function of Φ_a .

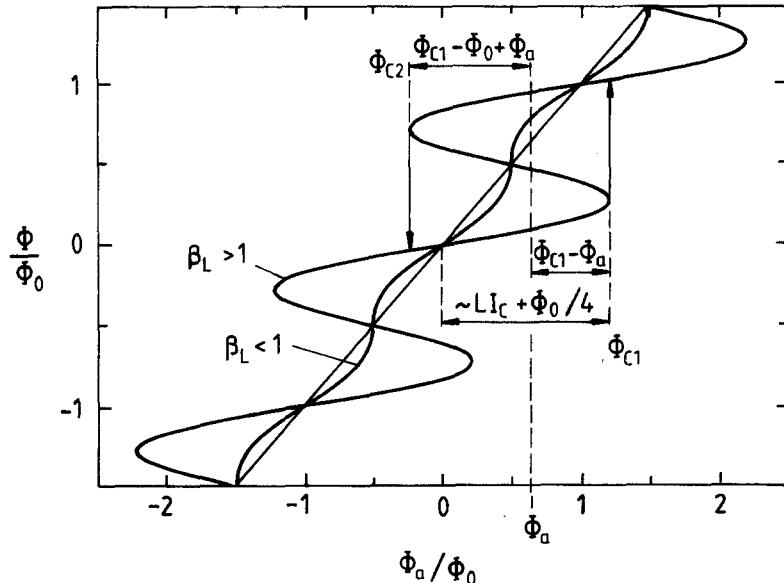


Fig. 2. The internal flux Φ of an rf SQUID as a function of the applied flux Φ_a in a ring with $\beta_L < 1$ (nonhysteretic) and with $\beta_L > 1$ (hysteretic). When $\beta_L \gg 1$, the SQUID is strongly hysteretic and the transitions occur at $\Phi_c \approx \pm [LI_c + (n + \frac{1}{4})\Phi_0]$.

Jaklevic *et al.*^{8,9} demonstrated an interference between two Josephson junctions in a superconducting ring. Because of coherence, the phase differences θ_1 and θ_2 across the two junctions are related by

$$\theta_1 - \theta_2 = \frac{2e}{\hbar} \oint_{\mathcal{L}} \mathbf{A} \cdot d\mathbf{l} = \frac{2\pi\Phi}{\Phi_0} \quad (10)$$

Quantum interference occurs also in normal metal rings that are smaller than the coherence length.⁶²⁻⁶⁵

3. SINGLE-JUNCTION (rf) SQUIDS

3.1. General

In rf SQUIDs the low-frequency external flux is measured with the help of a superposed radio-frequency flux in a resonant tank circuit. The amplitude of the rf voltage is monitored by a preamplifier, which is matched to the SQUID by the tank circuit. The equivalent circuit of Fig. 3, neglecting the resistive section ($R = 0$), can be described with

$$\left(\frac{1}{\omega_s^2} \frac{d^2}{dt^2} + \frac{1}{\omega_c} \frac{d}{dt} + 1 \right) \varphi + \beta_L \left(1 + \frac{\kappa}{\beta_L \omega_c} \frac{d}{dt} \right) \sin \varphi = \varphi_e \quad (11)$$

where $\varphi_e = 2\pi M I_T / \Phi_0 + \varphi_a$ and $\omega_s = (LC)^{-1/2}$; $\omega_c = R_q / L$ is the cutoff frequency of the loop. C is the junction capacitance, L is the inductance of the SQUID loop, and M is its mutual inductance with the tank circuit. R_q is the quasiparticle resistance of the junction, and κ is defined by Eqs. (1) and (3). I_T is the current oscillating in the tank circuit, and φ_a is the normalized applied flux; φ_e is the normalized total external flux. Equation (11) is derived for point-contact junctions, but it is applicable to tunnel junctions if the κ term is omitted and R_q is replaced by the shunt resistance.

The dynamics of the single-junction SQUID depends fundamentally on whether $\beta_L < 1$ (nonhysteretic SQUID) or $\beta_L > 1$ (hysteretic SQUID); see Fig. 2. In the following, both cases are examined separately.

3.2. rf SQUID in the Nonhysteretic Mode: The Inductive SQUID

3.2.1. Introduction

When $\beta_L < 1$, the dynamics of the rf-biased SQUID can be studied analytically. The SQUID operated in this regime, where $\varphi(\varphi_a)$ is a single-valued function, is also called an inductive SQUID or an L-SQUID. This emphasizes the fact that the nonhysteretic SQUID acts as a parametric inductance, whereas the hysteretic SQUID dissipates energy, acting as a flux-dependent resistor. Since the L-SQUID is a flux-dependent reactance, it can be used as a parametric amplifier. In magnetometer applications, the frequency of the signal ω_{sig} is much lower than the pump frequency ω_p and thus both sidebands, $\omega_p + \omega_{\text{sig}}$ and $\omega_p - \omega_{\text{sig}}$, are detected with a single tuned circuit. Such an amplifier is a double-sideband up-converter and its characteristics, such as the gain, stability, input impedance, etc., can be understood with the theory of parametric amplifiers.⁶⁶⁻⁶⁸

3.2.2. Operation of the Inductive SQUID

The characteristics of the L-SQUID follow from Eq. (11) when the tank circuit is taken into account. If the Q-value of this circuit, depicted in Fig. 3, is sufficiently high, the current I_T through the inductor L_T is given by (see Refs. 35 and 69)

$$\left[(1 - k^2) \frac{d^2}{dt^2} + \frac{1}{\tau_T} \frac{d}{dt} + \omega_T^2 \right] I_T \approx \omega_T^2 I_{\text{rf}} - \frac{\Phi_0}{2\pi} \frac{M}{LL_T} \frac{d^2\varphi}{dt^2} \quad (12)$$

where I_{rf} is the rf bias current, $\omega_T = (L_T C_T)^{-1/2}$ is the resonance angular frequency, and $\tau_T = R_T C_T$ is the time constant of the unloaded tank circuit; $k = M/(LL_T)^{1/2}$ is the coupling constant between the SQUID and the tank circuit. Equations (11) and (12) can be readily solved when $k \ll 1$ or $\beta_L \ll 1$. However, neither of these special cases applies to practical devices; therefore, a more general calculation is needed. Our analysis is based on the

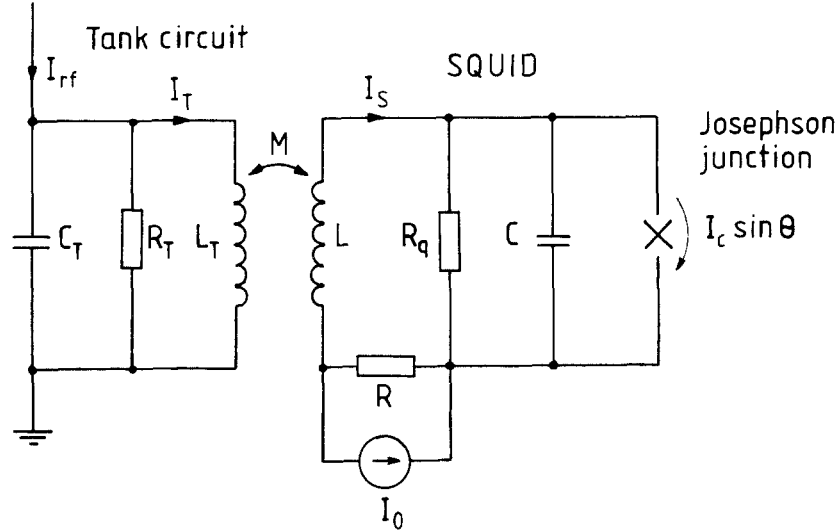


Fig. 3. Schematic diagram of the rf-biased single-junction SQUID. If $R = 0$ and $\beta_L = 2\pi L I_c / \phi_0 > 1$, the SQUID is hysteretic; if $\beta_L < 1$, it is called inductive. If $R \neq 0$, the so-called R-SQUID is obtained.

results reported by Erné *et al.*⁶⁹ Originally, the L-SQUID was studied by Hansma³¹; an interesting possibility to increase the flux-to-voltage transfer efficacy was discussed in Ref. 70 and verified experimentally by Dmitrenko *et al.*⁷¹ The L-SQUID has been investigated by several other groups as well.^{33,72-77}

To develop an analytic expression for the SQUID dynamics, we assume that $\omega_p \ll \omega_c = R_q/L$ and that the junction capacitance is negligible. Since the SQUID is matched to the preamplifier via a high- Q resonant circuit, only SQUID currents close to ω_p have a significant effect on the tank circuit.

Two basic methods have been applied to estimate the internal flux under sinusoidal excitation. The first method³¹ replaces the $\sin \varphi$ term in Eq. (11) by $\sin \varphi_e$. This approach is appropriate only for SQUIDs with a very low normalized inductance. The other approach⁶⁹ is based on a series expansion and applies to high- β_L devices as well; we shall follow this latter method. Under adiabatic conditions, i.e., at low frequencies, $\varphi(\varphi_e)$ is monotonic and periodic; the inversion of Eq. (11) leads to

$$\sin \varphi = -2 \sum_{n=1}^{\infty} (-1)^n \frac{J_n(n\beta_L)}{n\beta_L} \sin n\varphi_e \quad (13)$$

where J_n is the Bessel function of order n . The SQUID is usually sinusoidally excited by a high- Q tank circuit; thus the tank circuit current I_T is assumed

to be sinusoidal as well, and the normalized external flux is

$$\varphi_e = \hat{\varphi}_e \sin(\omega_p t + \vartheta) + \varphi_a \quad (14)$$

where $\varphi_a = 2\pi\Phi_a/\Phi_0$ is the external signal flux. Since the rf drive is coupled via a high- Q resonant circuit, $\hat{\varphi}_e$ is a slowly varying function* of time, related to \hat{I}_T as $\hat{\varphi}_e = 2\pi M\hat{I}_T/\Phi_0$. In practice, high-frequency excitations can also enter via the signal input; in the following, however, most signal power is assumed to be at low frequencies.

The flux in the SQUID ring can be calculated by putting the nonlinear $\sin \varphi$ term, given in Eq. (13), to Eq.(11) and by using Eq. (14). Inserting the result in Eq. (12), we find^{34,44,69}

$$Q_L \hat{I}_{\text{rf}} \sin \vartheta \approx \hat{I}_T [1 + \gamma g_L F(\hat{\varphi}_e, \varphi_a)/\hat{\varphi}_e] \quad (15)$$

$$Q_L \hat{I}_{\text{rf}} \cos \vartheta \approx -\hat{I}_T [\delta_L - g_L F(\hat{\varphi}_e, \varphi_a)/\hat{\varphi}_e] \quad (16)$$

Here $g_L = \beta_L k_L^2 Q_L$, which describes the coupling efficiency between the SQUID and the tank circuit, $\gamma = \omega_T(1 - \kappa/\beta_L)/\omega_c$, and

$$F(\hat{\varphi}_e, \varphi_a) = -4 \sum_{n=1}^{\infty} (-1)^n \frac{J_n(n\beta_L)}{n\beta_L} J_1(n\hat{\varphi}_e) \cos n\varphi_a \quad (17)$$

Here $\delta_L = 2Q_L(\omega_p - \omega_L)/\omega_L$ is the detuning parameter; ω_L and Q_L are the angular resonance frequency and the Q -value of the tank circuit, loaded by the extra damping due to R_q . If $\omega_p/\omega_c \ll 1$,

$$Q_L \approx \left[\frac{1}{Q_T} + k^2 \frac{\omega_p}{\omega_c} \right]^{-1} \quad (18)$$

$$k^2 Q_L \approx \left[\frac{1}{k^2 Q_T} + \frac{\omega_p}{\omega_c} \right]^{-1} \quad (19)$$

$$\omega_L \approx \omega_T \left[1 + \frac{1}{2} k^2 \frac{\omega_p^2}{\omega_c^2} \right] \quad (20)$$

where $Q_T = L_T \omega_T / R_T$ is the Q -value of the unloaded tank circuit.⁴⁴ These parameters reduce to those of the unloaded tank circuit in the limit of high ω_c or low k .

Solving \hat{I}_T and ϑ from Eqs. (15) and (16),

$$\hat{\varphi}_e = 2\pi M\hat{I}_T/\Phi_0 \approx \hat{\varphi}_{\text{rf}} + g_L \frac{\delta_L + \gamma}{1 + \delta_L^2} F(\hat{\varphi}_e, \varphi_a) \quad (21)$$

where

$$\hat{\varphi}_{\text{rf}} = \frac{2\pi M Q_L \hat{I}_{\text{rf}}}{\Phi_0 (1 + \delta_L^2)^{1/2}} \quad (22)$$

*The hat over a symbol denotes the amplitude of the sinusoidal signal.

If $g_L \ll 1$, the flux-to-voltage response can be obtained by replacing $\hat{\phi}_e$ on the right side of Eq. (21) by $\hat{\phi}_{rf}$. The signal can also be monitored with a balanced mixer that is made sensitive to amplitude or phase.

The flux-to-voltage characteristics are very strongly dependent on the design parameters of the L-SQUID, which is a disadvantage in magnetometer applications but an advantage in SQUID studies.^{35,45,78} Restrictions in the application of the RSJ model, as well as the exact form of the current-phase relationship of weak links and the value of the κ -term have been the main concerns in these investigations.

Differentiating both sides of Eq. (21) with respect to φ_a and using the relation $\hat{V}_T \approx \omega_p L_T \hat{I}_T = \omega_p L_T \hat{\phi}_e \Phi_0 / (2\pi M)$, we find

$$\frac{\partial \hat{V}_T}{\partial \Phi_a} \approx \frac{\omega_p}{k} \sqrt{\frac{L_T}{L}} \frac{(\delta_L + \gamma)}{(1 + \delta_L^2)} \frac{g_L g}{D} \quad (23)$$

where

$$D = 1 - g_L \frac{\delta_L + \gamma}{1 + \delta_L^2} \left[\frac{\partial F(\hat{\phi}_e, \varphi_a)}{\partial \hat{\phi}_e} \right] \quad (24)$$

and

$$g = \frac{\partial F(\hat{\phi}_e, \varphi_a)}{\partial \varphi_a} = 4 \sum_{n=1}^{\infty} (-1)^n \frac{J_n(n\beta_L)}{\beta_L} J_1(n\hat{\phi}_e) \sin n\varphi_a \quad (25)$$

If $\beta_L \ll 1$ and $\delta_L \approx 1$, $D \approx 1 - g_L [J_0(\hat{\phi}_{rf}) - J_2(\hat{\phi}_{rf})] \cos \varphi_a$, implying that the behavior of the L-SQUID depends fundamentally on whether $g_L < 1$ or $g_L > 1$. If $g_L > 1$, the parameter D can be tuned close to zero and, according to Eq. (23), an arbitrarily high flux-to-voltage conversion efficacy can be obtained, but at the cost of a decreased signal bandwidth and a strong dependence on SQUID parameters. If $g_L \ll 1$, the maximum flux-to-voltage conversion efficacy is approximately $(g_L/2)(\omega_p/k)(L_T/L)^{1/2}$, which is $g_L/2$ times that of the hysteretic SQUID (see Eq. (34)), favoring a high ω_p . In the opposite limit, however, g_L is restricted by $\beta_L(\omega_c/\omega_p)$ if $k^2 Q_T$ is very high. It should be emphasized here that the input characteristics of the amplifier are also strongly affected by interactions between the tank circuit and the SQUID.^{70,79} Consequently, in the complete analysis the input coupling circuits and the source impedance must be taken into account as well; our analysis applies only to SQUIDs with purely inductive sources, e.g., to a SQUID coupled to a flux transformer.

In Fig. 4a we have plotted the peak voltage \hat{V}_T across the tank circuit for different rf bias levels $\hat{\phi}_{rf}$, as a function of applied flux; Fig. 4b presents \hat{V}_T as a function of $\hat{\phi}_{rf}$. The curves are obtained through iterative use of

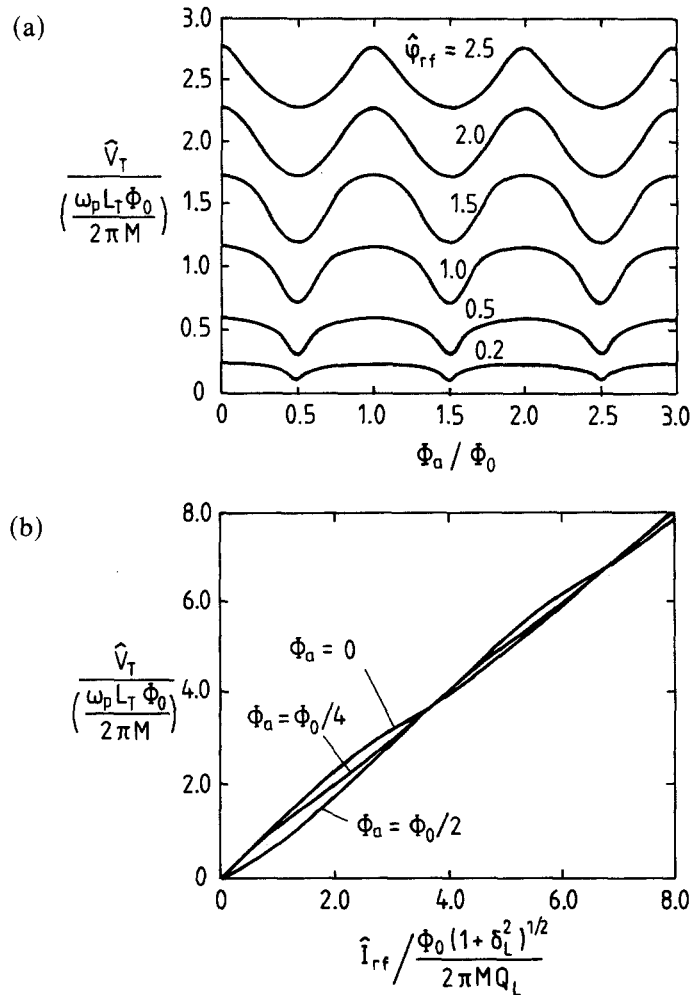


Fig. 4. Characteristics of the inductive rf SQUID calculated from Eq. (21). (a) Tank circuit circuit voltage \hat{V}_T as a function of applied flux Φ_a for different rf excitations $\hat{\varphi}_{rf} = 2\pi M Q_L \hat{I}_{rf} / (\Phi_0(1 + \delta_L^2)^{1/2})$. (b) $\hat{V}_T(\hat{I}_{rf})$ for three different values of Φ_a . For both figures $g_L(\delta_L + \gamma)/(1 + \delta_L^2) = 1$ and $\beta_L = 0.7$.

Eq. (21). When operating near the resonance, $\omega_p \approx \omega_L$, the amplitude modulation is small and the system is stable against parameter variations; the sidebands must, of course, be monitored by a mixer tuned sensitive to phase modulation. At high g_L , the $\Phi_a \hat{V}_T$ characteristics become hysteretic as predicted by Eq. (23).

3.2.3. Noise in the Inductive SQUID

Noise properties of the inductive rf SQUID are discussed in Refs. 70, 80, 81; here we present a slightly more general analysis. The noise sources can be represented in the equivalent tank circuit (see Fig. 5) by two resistors R_S and R_T in parallel with the inductor and the capacitor. $R_S = R_q L_T / (k^2 L)$ represents the resistance in the tank circuit due to the quasiparticle conductance or it can be replaced by the shunt resistance of the Josephson junction; R_T describes tank circuit and preamplifier losses. The values for the resistances are obtained from Eqs. (15) and (16). The noise temperatures of the tank circuit and the preamplifier are denoted by T_T and T_A . The noise voltage over the tank circuit is determined by the noise current sources and the dynamic tank-circuit resistance $R_{\text{dyn},T}$. In addition, the preamplifier noise voltage and the flux noise caused by the shunt resistor increase the detected amplitude fluctuation. Half of the total energy of the additive voltage noise appears as fluctuations in the phase of the signal voltage; the spectral density of amplitude fluctuation can thus be written as

$$S_{\hat{V}_T} = 2k_B R_{\text{dyn},T}^2 \left(\frac{T}{R_S} + \frac{T_T}{R_T} + \frac{T_A}{2R_{\text{opt}}} \right) + k_B T_A R_{\text{opt}} \quad (26)$$

where

$$R_{\text{dyn},T} = \frac{\partial \hat{V}_T}{\partial \hat{I}_{\text{rf}}} = \frac{\omega_p L_T Q_L}{(1 + \delta_L^2)^{1/2}} D^{-1} \quad (27)$$

Here R_{opt} is the optimal source resistance of the preamplifier; because it is

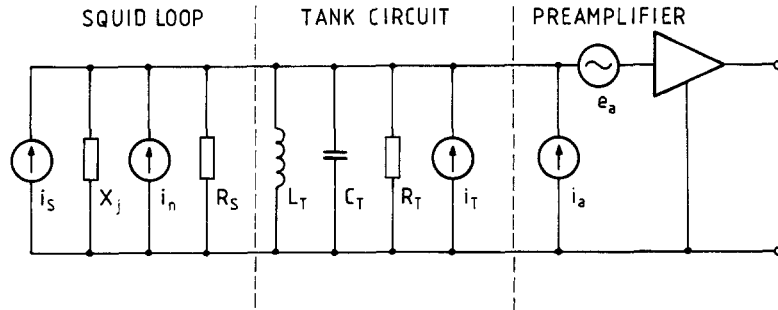


Fig. 5. Equivalent circuit for the L-SQUID, coupled to a preamplifier through a tank circuit. The dissipative elements R_S and R_T , with noise sources, are introduced by the quasiparticle resistance of the Josephson junction, dissipations in the tank circuit, and by the input impedance of the preamplifier; $i_n = (4k_B T / R_S)^{1/2}$, $i_T = (4k_B T_T / R_T)^{1/2}$, $i_a = (2k_B T_A / R_{\text{opt}})^{1/2}$, and $e_a = (2k_B T_A R_{\text{opt}})^{1/2}$. R_{opt} is the optimal input impedance of the preamplifier.

assumed to be real, the voltage noise and the current noise of the amplifier are considered uncorrelated. Including the intrinsic flux noise $S_{\Phi_i} = 4k_B TL^2/R$, the energy sensitivity is

$$\begin{aligned}\varepsilon &= \frac{(\partial \hat{V}_T / \partial \Phi_a)^2 S_{\Phi_i} + S_{\hat{V}_T}}{2L(\partial \hat{V}_T / \partial \Phi_a)^2} \\ &= \frac{2k_B T}{\omega_c} + \frac{k_B T}{\beta_L \omega_c g^2} \frac{1 + \delta_L^2}{(\gamma + \delta_L)^2} \left[1 + \frac{1}{k^2 Q_T} \frac{\omega_c}{\omega_p} \frac{T_{eq}}{T} \right] + \frac{k_B T_A}{\mathcal{F}} \quad (28)\end{aligned}$$

where $T_{eq} = T_T + T_A R_T / 2R_{opt}$ is the equivalent noise temperature of the unloaded tank circuit. The forward transfer frequency \mathcal{F} is defined here as (see also Ref. 82)

$$\mathcal{F} = \frac{2L}{R_{opt}} \left(\frac{\partial \hat{V}_T}{\partial \Phi_a} \right)^2 \quad (29)$$

\mathcal{F} is the ratio of the output power to the energy fed into the SQUID ring, and it is regarded as one of the most important figures-of-merit for SQUIDs. A high- \mathcal{F} SQUID is convenient since it is not very demanding on amplifier design. Equation (28) is accurate as long as the coupling between the SQUID and the tank circuit is not too strong in converting tank circuit noise into flux noise in the SQUID loop.⁷⁰ In the case of strong interaction, this correlation between the “input” and “output” noise influences the design of the flux transforming circuits.

If $k^2 Q_T$ is maximized with a superconducting tank circuit coil, if a cooled preamplifier is used to minimize tank circuit and amplifier noise, and if the frequency is tuned for high \mathcal{F} ($\delta_L \approx 1$), the intrinsic energy sensitivity of the low- β_L device can be estimated from Eq. (28) (see also Ref. 4):

$$\varepsilon_{min} \approx \frac{3k_B T}{\beta_L \omega_c} \quad (30)$$

In this regime the L-SQUID behaves as a negative-resistance parametric amplifier; its ultimate sensitivity depends on the device temperature and the quality factor of the parameter-dependent Josephson junction reactance. In the opposite regime, $k^2 Q_T \ll 1$, \mathcal{F} has a much more moderate value $(1/2)\omega_p \beta_L g_L$, and the two last terms in Eq. (28), which depend on the amplifier noise, become dominant. In this mode ε is determined by T_A and ω_p . It is not difficult to recognize the outstanding improvement obtained by increasing $k^2 Q_T$, until the transfer efficacy starts to increase. The L-SQUID can, of course, be operated at resonance where the amplitude

modulation disappears; then the flux must be detected by a phase-sensitive method. Since the power at the sidebands is not increased by the mutual interaction between the tank circuit and the SQUID loop, this mode of operation is stable but does not necessarily lead to a low-noise device. Nevertheless, a predictable and real output impedance essentially facilitates the design of the preamplifier.

3.2.4. Discussion

As mentioned, the condition $g_L > 1$ makes it possible to obtain a very high flux-to-voltage transfer efficacy; the point of operation, however, is highly sensitive to changes in the amplitude and frequency of the rf bias; increased low-frequency noise can result. In addition, the signal bandwidth is reduced, and the dynamic output impedance is modified, making it difficult to match the inductive SQUID into the optimal input impedance of the preamplifier. In contrast, the low-gain mode offers more stable operation but higher intrinsic noise; if $\omega_p = 2\pi \times 20$ MHz, $\beta_L = 0.5$, $k = 0.2$, and $T_A = 100$ K, we obtain $\mathcal{F} \approx 2\pi \times 100$ kHz and $\epsilon \approx 10^{-27}$ J/Hz, corresponding to the flux noise $\langle \Phi_n^2 \rangle^{1/2} \approx 7 \cdot 10^{-4} \Phi_0 / \text{Hz}^{1/2}$ for an L-SQUID with $L = 1.0$ nH. These drawbacks explain why inductive SQUIDs are rarely used. We may, however, conclude that the L-SQUID has some importance in investigating SQUID parameters and junction models and in experiments where the quantum noise limit is the goal. The L-SQUID is potentially suitable for rf power and attenuation measurements; however, its narrow signal bandwidth and strong interaction with the tank circuit make it less desirable for such applications (see Sec. 3.4).

3.3. rf SQUID in the Hysteretic Mode

3.3.1. Operation of the rf SQUID in the Dissipative Regime

If $\beta_L > 1$, the total flux through the SQUID loop is no longer a single-valued function of the applied flux; the resulting energy dissipation during the flux jumps (arrows in Fig. 2) dominates the dynamics. Hysteretic rf SQUIDs have been discussed extensively in the literature^{32,82–88}; we review them only briefly.

Just like the L-SQUID, the hysteretic SQUID is coupled to a resonant tank circuit for impedance matching with an rf preamplifier. In principle, the rf voltage could be sensed directly across the junction terminals, but the impedance there is very low.

The maximum voltage across the tank circuit depends on the amount of flux required for flux jumps. The points of flux transitions (see Fig. 2) can be found from Eq. (9): $\varphi_c = 2\pi\Phi_c/\Phi_0 = \pi/2 + (\beta_L^2 - 1)^{1/2} + \arcsin(1/\beta_L)$. Since $V_T = \omega_p L_T I_T$, the amplitude of the tank circuit voltage \hat{V}_T approaches

before transitions either

$$\hat{V}_{c1} = \frac{\omega_p L_T}{M} (\Phi_c - \Phi_a) \quad (31)$$

or

$$\hat{V}_{c2} = \frac{\omega_p L_T}{M} (\Phi_c - \Phi_0 + \Phi_a) \quad (32)$$

depending on the branch the system occupies. Because of energy absorption from the tank circuit by the SQUID, the voltage collapses, rising up again until the next transition. \hat{V}_T resembles a sawtooth pattern, and for a fixed rf excitation, $\hat{V}_T(\Phi_a)$ is a triangular function of flux with period Φ_0 (Fig. 6). The energy ΔE absorbed in one complete cycle is roughly equal to the area of the hysteresis loop in the $\Phi - \Phi_a$ plane, divided by the SQUID

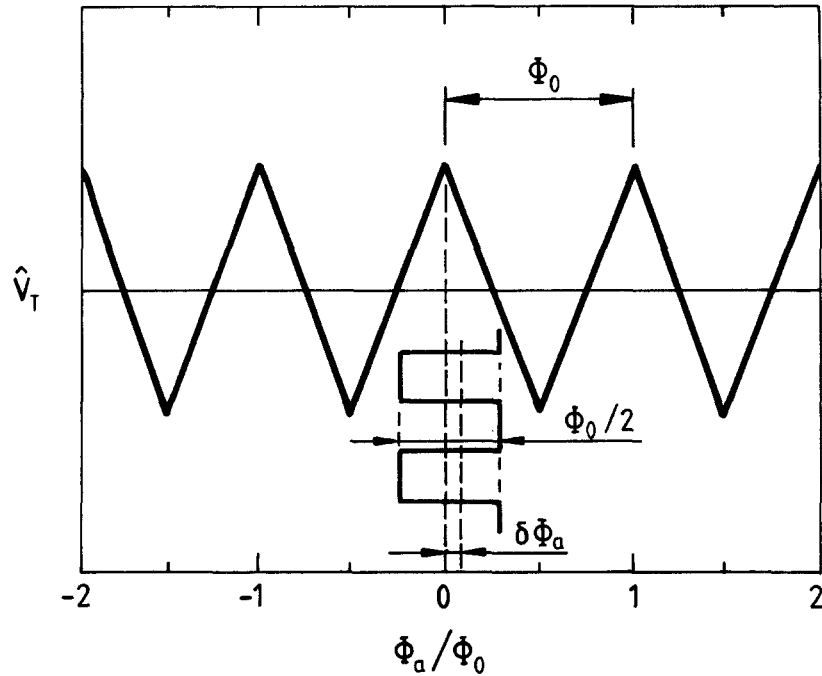


Fig. 6. Peak value of the tank circuit voltage \hat{V}_T as a function of Φ_a for the hysteretic rf SQUID. The period of the triangle pattern is the flux quantum Φ_0 . The square-wave modulation pattern of amplitude $\Phi_0/2$, to be discussed in detail in Sec. 7, is shown for a typical point of operation.

inductance (see Fig. 2):

$$\Delta E \approx \frac{\Phi_0^2}{\pi L} (\varphi_{c1} - \pi) \approx \frac{\Phi_0^2}{\pi L} \left(\beta_L + \frac{1}{2\beta_L} - \frac{\pi}{2} \right) \quad (33)$$

According to this estimate, the energy absorption is insensitive to the point of operation. In contrast, the peak value of the tank circuit voltage is strongly affected by the external flux and, thus, the rf SQUID acts as a flux-dependent resistor. Suppose next that $\Phi_a \neq n\Phi_0$, and that the rf current \hat{I}_{rf} is swept up: \hat{V}_T climbs up until the transitions start to dissipate energy from the tank circuit, after which \hat{V}_T remains unchanged, creating a horizontal plateau in the $\hat{V}_T \hat{I}_{rf}$ characteristics. When the energy fed into the circuit during every rf cycle exceeds ΔE , the voltage can rise again. The dissipated power increases as $(1/2)\hat{V}_{step}\Delta\hat{I}_{rf}$ when moving along the plateau \hat{V}_{step} , increasing the rate of flux transitions. Since the peak voltage cannot rise before the power $\Delta E \omega_p / 2\pi$ is exceeded, the length of the first step $\Delta\hat{I}_{rf}$ varies from $2\Phi_0 k^2 (1 - \pi/\varphi_{c1}) / M\pi$ to $2\Phi_0 k^2 / M\pi$, where $k = M/(LL_T)^{1/2}$. If $\Phi_a = n\Phi_0$, the first two steps will degenerate to a single plateau, which does not end until $2\Delta E$ is dissipated during every rf cycle. Further increase of rf power creates new plateaus and ramps; the so-called staircase pattern is formed as shown for three values of the applied flux in Fig. 7. When $k^2 Q_T > \pi/4$, the plateaus overlap and proper adjustment of the rf power yields the triangular pattern.

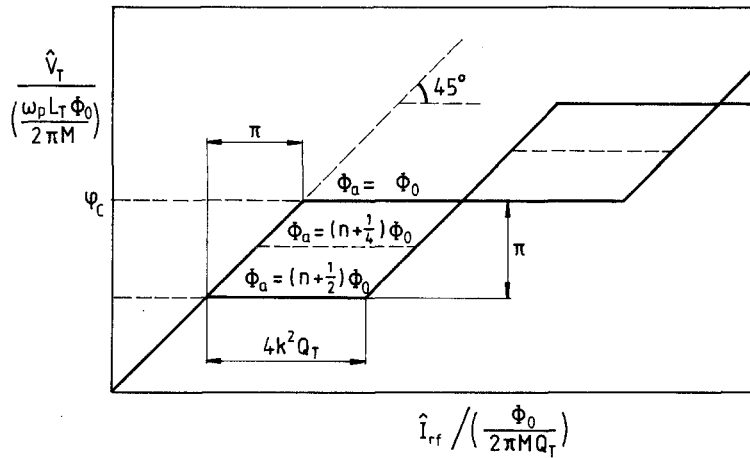


Fig. 7. \hat{V}_T as a function of the rf excitation \hat{I}_{rf} ; staircase patterns for three values of applied flux Φ_a , $4k^2 Q_T = 2\pi$.

According to Eqs. (31) and (32), the maximum modulation in \hat{V}_T , as a function of flux, is $\Delta \hat{V}_{T,\text{peak}} = \omega_p L_T \Phi_0 / 2M$; thus

$$\frac{\partial \hat{V}_T}{\partial \Phi_a} = \frac{\omega_p}{k} \sqrt{\frac{L_T}{L}} \quad (34)$$

It turns out that thermal noise tilts the plateaus of the $\hat{I}_{\text{rf}} \hat{V}_T$ characteristics; thus the dynamic impedance $R_{\text{dyn}} = \partial \hat{V}_T / \partial \hat{I}_{\text{rf}}$ differs from zero. If the normalized slope of the plateau is $\alpha = (\omega_p L_T Q_T)^{-1} \Delta \hat{V}_T / \Delta \hat{I}_{\text{rf}}$, $R_{\text{dyn}} = \alpha R_T$, implying that $\mathcal{F} = 2L(\partial \hat{V}_T / \partial \Phi_a)^2 / R_{\text{dyn}} = 2\omega_p / (\alpha k^2 Q_T)$ (see Eq. (29)) when the SQUID is operated at resonance. Since a device with high \mathcal{F} is insensitive to the noise temperature of the preamplifier, a high pump frequency and low $k^2 Q_T$ seem attractive. However, $k^2 Q_T$ cannot be much smaller than $\pi/4$; therefore $k^2 Q_T \approx 1$ optimizes the overall performance of the rf SQUID.

The optimal choice of the mutual inductance and, particularly, of the product $k^2 Q_T$ is discussed in detail by Jackel and Buhrman.⁸⁸ They argue that the best performance is obtained when $k^2 Q_T > 1$. The same conclusion was drawn by Simmonds and Parker⁸⁹ as early as in 1971 on the basis of computer simulations. Moreover, Ehnholm⁸² derived a small-signal model for an rf SQUID with complete input and output circuits and was able to show that the choice $k^2 Q_T \approx 1$ maximizes \mathcal{F} ($\mathcal{F}_{\text{max}} \approx 2\omega_p(1 - \alpha_{\text{exp}})$), where α_{exp} is the experimentally determined value of α , and minimizes the intrinsic energy sensitivity. The optimization of the rf SQUID is also discussed by Pascal and Sauzade⁷³ and Vasilev *et al.*⁸⁰

3.3.2. Noise in the Hysteretic rf SQUID

Thermal noise has a drastic influence on the operation of the rf SQUID. Figure 8 shows paths of the internal flux under sinusoidal excitation, both without and with thermal noise. In Fig. 8b the junction capacitance is not properly damped ($\beta_c = 3$), which leads to strong plasma oscillations after each transition. In the presence of noise when $\omega_p \ll \omega_c$ (Fig. 8c), thermally activated escape of flux, through the potential barrier, is likely to occur before the critical point for the flux jump, resulting in high uncertainty of the transition point and, consequently, in large excess noise. Figure 8d visualizes the improvement in sensitivity obtained through an increased pump frequency; transitions now occur very close to the critical points. Figure 9 illustrates the effect of thermal noise on the staircase pattern.

Because of the uncertainty in the flux transition, the equivalent flux noise is no longer dominated by thermal fluctuations in the quasiparticle conductance. By applying Kurkijärvi's calculations⁹⁰ for the uncertainty, Kurkijärvi and Webb⁹¹ derived the equivalent flux noise. They also pointed out that the plateau slope α and the intrinsic flux noise are interrelated; it

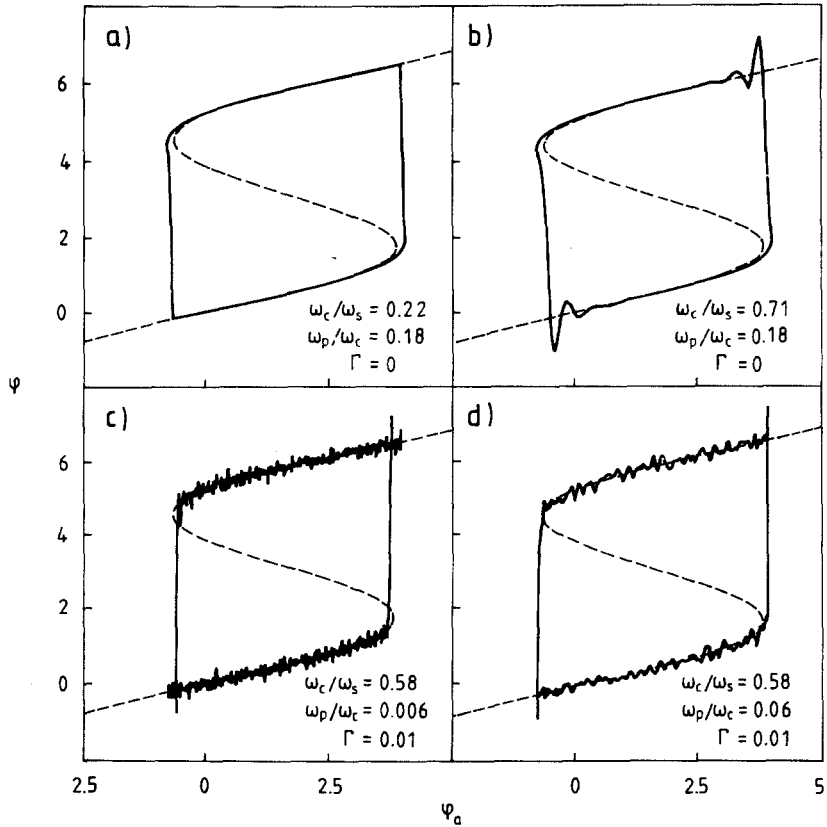


Fig. 8. Trajectories of flux, enclosed by the SQUID ring, when the hysteretic loop ($\beta_L = 6$) is sinusoidally excited. The noiseless motion of (a) a well-damped and (b) an inadequately damped SQUID are shown. Figure (c) and (d) illustrate the influence of the pump frequency on the point of flux transitions evoked by thermal noise. The dotted line is obtained from Eq. (9).

is thus convenient to express the intrinsic energy sensitivity⁸⁸ in terms of α

$$\varepsilon \approx \frac{1.5\Phi_0^2}{L\omega_p} \alpha^2, \quad \alpha^2 \approx 1.5\beta_L^{2/3} \left[\frac{k_B T L}{\Phi_0^2} \right]^{4/3} \quad (35)$$

The intrinsic flux noise increases the effective noise temperature of the tank circuit. The nonsinusoidal current-phase relation of the Josephson junction causes the fractional step rise to differ from the theory. If noise from the tank circuit and from the preamplifier is included as well, the experimentally defined value of α , α_{exp} , can be used to estimate the equivalent input energy

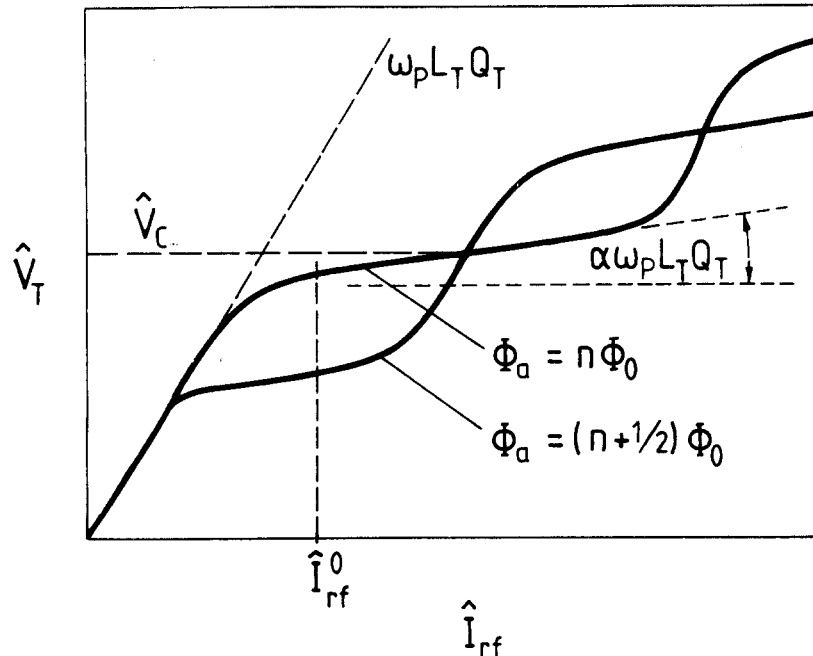


Fig. 9. The current-voltage characteristics of a hysteretic rf SQUID in the presence of thermal noise, corresponding to even and odd multiples of $\Phi_0/2$ in the externally applied flux.

sensitivity^{82,88,92}

$$\varepsilon = \frac{\pi k_B}{\omega_p (1 - \alpha_{\text{exp}})^2} \left\{ k_{\text{eff}} \frac{R_{\text{opt}}}{R_T} T_A + \frac{\alpha_{\text{exp}}^2}{2} k_{\text{eff}}^{-1} \left(T_T + T_i + \frac{1}{2} \frac{R_T}{R_{\text{opt}}} T_A \right) \right\} \quad (36)$$

where $k_{\text{eff}} = k^2 Q_T / \pi$ and $T_i \approx k^2 Q_T \Phi_0^2 / (\pi k_B L)$ is called the intrinsic tank-circuit temperature; T_T is the noise temperature of the tank circuit. $R_T = \omega_p L_T Q_T$ denotes dissipation in the tank circuit including the preamplifier. The equivalent noise temperature and the optimum source resistance of the preamplifier, T_A and R_{opt} , respectively, are used to describe the voltage noise source and the current noise source, assumed here to be uncorrelated (see Fig. 5). Usually $T_T < T_A$, in which case the energy sensitivity approaches its minimum when $k_{\text{eff}} \approx \alpha_{\text{exp}} R_T / (2 R_{\text{opt}})$. Since the maximum amplitude of the rf signal is obtained with $k^2 Q_T > \pi/4$, the tank circuit and the amplifier must be designed so that $r = R_{\text{opt}} / R_{\text{dyn}} = R_{\text{opt}} / (\alpha_{\text{exp}} R_T) \leq 1$. With $k^2 Q_T = \pi/4$ and $r = 1$,

$$\varepsilon \approx \frac{\pi k_B \alpha_{\text{exp}}}{\omega_p (1 - \alpha_{\text{exp}})^2} [T_A + \alpha_{\text{exp}} (T_i + T_T)] \quad (37)$$

The intrinsic tank-circuit temperature is related to the energy dissipation caused by the hysteresis loop. Apparently, the size of the hysteresis loop should be as small as possible but sufficient for proper operation. The excess noise from the uncertainty in flux transitions was also discussed by Danilov *et al.*,⁷⁰ who showed that the output noise of the SQUID depends on the bias point. The influence of the input circuit via current fluctuations in the SQUID ring has been investigated by many authors.^{82,93-96}

3.3.3. Discussion

The operation of the rf SQUID is based on rf-driven traversal around the hysteresis loop. The transfer parameters are predictable; energy dissipation reduces the dynamic Q -value, broadening the signal bandwidth. The main drawback of the hysteretic rf SQUID is its high intrinsic noise due to fluctuations in flux jumps. In a typical SQUID, with a loop inductance of 1 nH, the effective temperature of the tank circuit $T_i + T_T$ is of the order of 150 K. However, a careful design of the preamplifier is still the key to a low-noise rf SQUID, since $\alpha_{\text{exp}}(T_i + T_T) \approx 30$ K. If the noise temperature is $T_A = 200$ K and $\omega_p = 2\pi \times 20$ MHz, then $\varepsilon \approx 2.4 \cdot 10^{-29}$ J/Hz, corresponding to $\langle \Phi_n^2 \rangle^{1/2} \approx 10^{-4} \Phi_0 / \text{Hz}^{1/2}$ for $L = 1$ nH. The intrinsic energy sensitivity can be reached by cooling the preamplifier;^{45,97-101} increased helium boil-off, however, limits its applicability.

An improvement in sensitivity can be obtained by increasing the pump frequency, but the benefit is partly cancelled by the increasing preamplifier noise. At very high frequencies ($\omega_p \approx \omega_c$), the absorption loop begins to deform, manifesting itself as a reduced output conductance. The flux sensitivity diminishes and the rf SQUID begins to resemble an L-SQUID. On the basis of computer simulations, Keränen and Kurkijärvi¹⁰² concluded that the intrinsic energy sensitivity of an ideal rf SQUID at high frequencies ($\omega_p \approx \omega_c$) is limited by

$$\varepsilon \geq 1.5 k_B T \beta_L^{1/2} / \omega_c \quad (38)$$

which shows that this quantity can be as small as $\varepsilon \approx 6 k_B T (LC)^{1/2}$ for $\beta_L = 3$ at the hysteresis limit of the junction, $\beta_c = \beta_L (\omega_c / \omega_s)^2 = 0.7$. Buhrman and Jackel⁷⁴ showed that proper adjustment of SQUID parameters provides a low-noise rf SQUID even when $\omega_p > \omega_c$. Anyway, it is evident that a SQUID cannot reach the classical noise limit of the resistive loop, i.e., the thermal noise energy ($k_B T/2$) divided by the noise bandwidth ($\omega_c/4$).

It is essential to keep in mind that a well-behaving rf SQUID can be constructed only by proper damping of the junction. Incomplete attenuation may lead to multiple transitions and thus to excess noise. The condition $\beta_c \approx 1$ should ensure stable operation. Unfortunately, owing to parasitic resonances or capacitances introduced by the signal coil, strong coupling

to the signal coil may substantially decrease the effective damping (see Sec. 4.2.3).

Recently, dc SQUIDs have replaced rf SQUIDs, at least in applications involving the simultaneous use of several magnetometers. It seems, however, that the discovery of high- T_c materials makes the rf SQUID interesting again (Sec. 6).

3.4. rf SQUID in the High-Frequency Regime

3.4.1. Introduction

High pump frequencies are tempting because of reduced flux noise and increased signal bandwidth. SQUIDs operated at very high frequencies have been studied both experimentally and theoretically.^{4,74,103-114} The dynamics of the system is fundamentally dependent on whether the cutoff frequency ω_c of the SQUID loop is exceeded or not. In addition, if the wavelength of the pump signal is shorter than the distance between the first amplifier and the SQUID, a simple tank circuit cannot be realized; in this case the output impedance of the SQUID and the amplifier should be matched to the impedance of the transmission line in order to prevent reflections.

Buhrman and Jackel⁷⁴ concluded, on the basis of their computer simulations, that the characteristics of the hysteretic SQUID remain unchanged when the pump frequency approaches ω_c . The dynamics in this intermediate frequency range is very complex and it is not well-analyzed in the literature. On the contrary, when the frequency is further increased, the SQUID enters the quasi-nonhysteretic mode and can be studied analytically.

3.4.2. Operation of the Microwave SQUID

The microwave SQUID (M-SQUID) is usually formed from a point-contact Josephson junction in a waveguide or from a tunnel junction terminating a $\lambda/4$ section of an integrated transmission line. It can also be a tiny loop in a cavity resonator, which acts as an impedance-matching circuit.¹¹¹

If $\omega_p \gg \omega_c$ or the SQUID loop transmission line forms a $\lambda/4$ resonator, the dynamics of the SQUID can be studied by separating the quantum phase difference into its low- and high-frequency components, θ_{lf} and $\hat{\theta}_e \sin(\omega_p t + \gamma)$, respectively. Inserting both components into the RSJ-model (see Eqs. (3) and (4)), one finds the junction impedance

$$\begin{aligned} \{\bar{Z}_J\}_{\omega_p} \approx R_q & \{[1 + \kappa J_0(\hat{\theta}_e) \cos \varphi_{lf}] \\ & + j[\kappa J_2(\hat{\theta}_e) - 2(\beta_L \omega_c / \omega_p) J_1(\hat{\theta}_e) / \hat{\theta}_e] \cos \varphi_{lf}\}^{-1} \end{aligned} \quad (39)$$

where $\varphi_{lf} = 2\pi\Phi_{lf}/\Phi_0 = -\theta_{lf} + 2n\pi$ is the normalized low-frequency flux entering the SQUID loop. The amplitude of the high-frequency component is given by $\hat{\theta}_e = 2\pi\hat{V}_j/(\omega_p\Phi_0)$, where \hat{V}_j is the amplitude of the microwave voltage over the junction. J_n denotes the n th order Bessel function and j is the imaginary unit. In addition, both the effective low-frequency critical current and the κ -term are reduced by the factor $J_0(\hat{\theta}_e)$; thus $\varphi_{lf} = \varphi_a - \beta_L J_0(\hat{\theta}_e) \sin \varphi_{lf}$. Because of impedance mismatch, part of the incident wave is reflected from the junction. The reflection coefficient is determined by the contact impedance and, therefore, the detected signal is proportional to $\cos \varphi_{lf}$, which in turn depends on φ_a . It can be shown that the observed voltage V_D is related to φ_a by¹⁰⁹

$$V_D \propto \beta_R \frac{J_1(\hat{\theta}_e)}{\hat{\theta}_e} \left[1 + 4 \sum_{n=1}^{\infty} (-1)^n \frac{J'_n(n\beta_R)}{n\beta_R} \cos n\varphi_a \right] \quad (40)$$

where $\beta_R = J_0(\hat{\theta}_e)\beta_L$. $\hat{\theta}_e$ is proportional to the square root of the power transmitted to the junction. J'_n denotes the derivative of the n th order Bessel function. Equation (40) is derived by assuming that the flux-dependent components of the junction impedance are large compared to R_q ; thus $\beta_L < \omega_p/2\omega_c$. In Fig. 10a the absolute value of the reflection coefficient $\bar{\Gamma} = (\{\bar{Z}_j\}_{\omega_p} - \bar{Z}_0)/(\{\bar{Z}_j\}_{\omega_p} + \bar{Z}_0)$, where \bar{Z}_0 is the source impedance, is plotted as a function of the incident voltage at different values of Φ_a . If $\beta_L > 1$, the SQUID response is multivalued but at high microwave levels the response is very close to sinusoidal as predicted by Eq. (40). Figure 10b presents Γ^2 for different incident voltage levels as a function of Φ_a ; for low levels, hysteresis is found. If the quasiparticle conductance of the junction is matched to the line admittance, the forward transfer frequency $\mathcal{F} \approx \beta_L^2\omega_c/4$.¹¹³ In this case, \mathcal{F} denotes the power change in both sidebands when the input flux energy is changed. The maximum possible β_L depends on ω_p and on the applications the SQUID is intended for; for example, in rf attenuation measurements the SQUID response must be sinusoidal and $\beta_L < 1$.

The energy sensitivity of the microwave SQUID is usually determined by the noise temperature T_A of the preamplifier, since $T_A \gg T$ at microwave frequencies. The above approximation for \mathcal{F} leads to $\varepsilon \approx k_B T_A / \mathcal{F} \approx 4k_B T_A / (\beta_L^2 \omega_c)$, when the preamplifier is prevented from transmitting noise to the SQUID, e.g., by a circulator. The improvement in energy sensitivity is thus limited by the characteristic frequency of the SQUID ring. In Ref. 106 the reflected power in the device is optimized with $\beta_L \approx 1$ by omitting the quasiparticle resistance; the result is $\varepsilon \approx k_B T_A / 2\omega_p$. Both approximations show that the microwave SQUID exhibits properties of a very low noise device: for an X-band* microwave SQUID with $\beta_L = 1$, $\omega_c = 2\pi \times 10$ GHz,

*The frequency range from 8 GHz to 13 GHz.

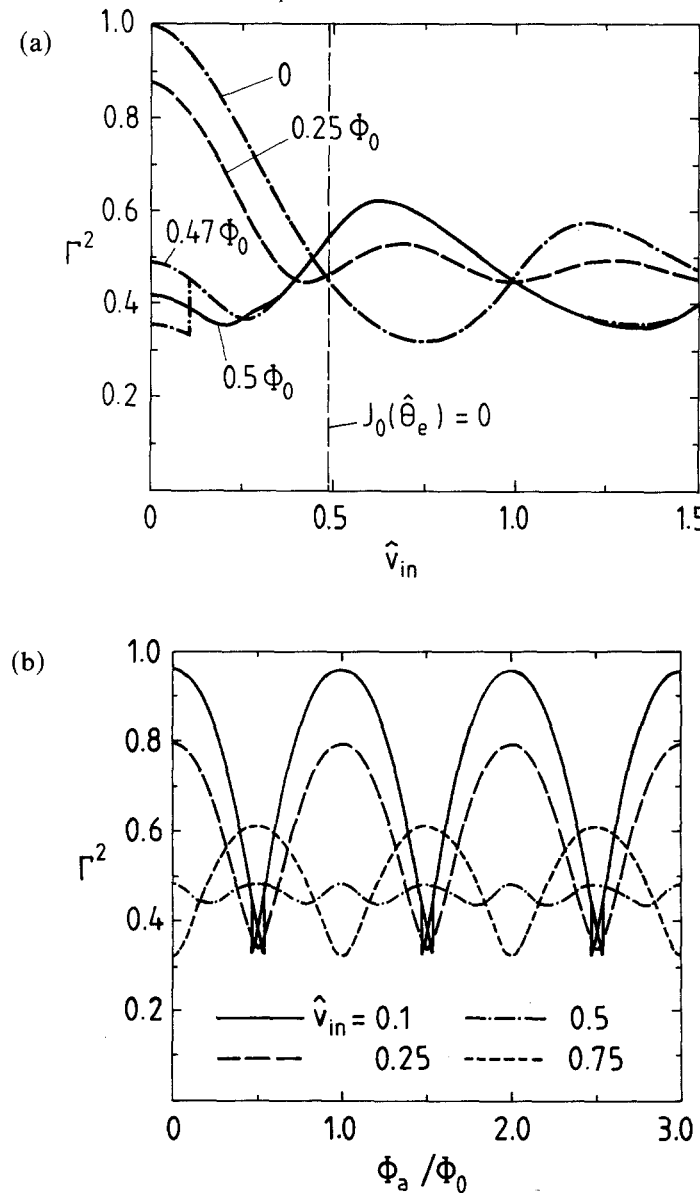


Fig. 10. (a) Absolute value of the reflection coefficient Γ^2 as a function of the normalized incident voltage $\hat{v}_{\text{in}} = \hat{V}_{\text{in}}/R_q I_c$, for four different values of applied flux; $\beta_L = 1.5$, $|\bar{Z}_0|/R_q = 0.2$, $\omega_p/\omega_c = 0.5$, and $\kappa = -1.0$. A hysteresis loop is seen for $\Phi_a = 0.47\Phi_0$; for $\Phi_a = 0.5\Phi_0$ the two branches coincide. The vertical dashed line indicates the value of \hat{v}_{in} where $J_0(\hat{\theta}_e) = 0$, i.e., $\beta_R = 0$, at $\Phi_a = \Phi_0/4$. (b) The corresponding Γ^2 - Φ_a characteristics.

and $T_A = 300$ K, one obtains $\varepsilon \approx 10^{-31}$ J/Hz, which is two orders of magnitude lower than for a typical hysteretic rf SQUID. It should be noted that, like the L-SQUID, the M-SQUID can be tuned to produce an infinite value of the transfer function; near this point of operation the energy sensitivity is limited by the intrinsic noise of the SQUID, not by the preamplifier.

3.4.3. Discussion

If the parameter $\beta_R = J_0(\hat{\theta}_c)\beta_L$ is reduced by proper adjustment of the microwave power, the time average of the detected amplitude turns out to be the zeroth-order Bessel function of the applied flux. Since the zeros of the Bessel function can be determined with high precision, a scale of current ratios and, hence, attenuation can be constructed.^{103,109,115-117} In practice, however, this ideal picture is partly destroyed by the nonlinear quasiparticle conductance and screening currents in the SQUID loop. Fortunately, by using tantalum or vanadium as the junction material instead of the more common niobium, a practical attenuation calibrator can be constructed;¹⁰⁹ YBaCuO junctions have recently been shown to be suitable for this application.¹¹³ Evidently, thin-film SQUIDs and high- T_c materials in rf metrological applications will be objects of intensive studies in the future.

The microwave SQUID is very seldom used in practical applications, although it can be made to a high-gain ($\mathcal{F} \approx 2\pi \times 2.5$ GHz), low-noise ($\varepsilon \approx 10^{-31}$ J/Hz) magnetometer with a large signal bandwidth ($B \approx 1$ GHz). The lack of reliable thin-film devices, the cost of the electronics, and the existence of dc SQUIDs perhaps explain this situation.

3.5. Resistive rf SQUID

3.5.1. Introduction

An rf-biased resistive SQUID, often called the R-SQUID, is obtained by adding a resistive portion to a single-junction SQUID ring (see Fig. 3). If a dc current I_0 is injected through the shunt resistor R , the Josephson junction oscillates at a frequency proportional to the voltage drop across the junction. The R-SQUID with a resonant circuit is an up-converter, transforming the audio-frequency signal to rf sidebands of the tank circuit voltage.

The R-SQUID can be used as an ordinary voltmeter, but thermal noise from the small shunt resistor limits its sensitivity. However, the high thermal noise can be used to establish an accurate temperature scale as proposed by Kamper and Zimmerman¹¹⁸ and as further developed by Soulen *et al.*^{45,119,120} and by Hoffmann and Buchholz.⁹⁸ The R-SQUID can also monitor heat flow through a metallic section by converting the temperature

difference into a voltage via the thermopower effect,¹²¹ or it can act as a voltage-controlled oscillator at microwave frequencies.¹²²

3.5.2. Theory of Operation

It can be shown^{44,123} that the dynamics of the SQUID interrupted by a resistor (see Fig. 3) can be analyzed by solving the high-frequency part from Eq. (11) and the low-frequency part from

$$\dot{\phi}_a = \omega_0 - \omega_R \sum_{n=1}^{\infty} g_n \sin n\varphi_a \quad (41)$$

where

$$g_n \approx 2(-1)^n \frac{J_n(n\beta_L)}{n\beta_L} J_0(n\hat{\varphi}_{rf}) \quad (42)$$

$\omega_0 = 2\pi RI_0/\Phi_0$, and $\omega_R = 2\pi RI_c/\Phi_0$. The parameter dependence of the low-frequency Josephson frequency $\langle \dot{\phi}_a \rangle$, which is proportional to the dynamic resistance $\rho = \Phi_0 \langle \dot{\phi}_a \rangle / (2\pi I_c)$,¹¹⁸ and the available signal power are the most important characteristics from the practical point of view. The audio frequency is used to determine the value of the shunt resistor; the low signal power increases the frequency variance, disturbing the temperature determination. The high-frequency dynamics in the resistive ring can be solved with the methods used for the L-SQUID. It turns out, however, that the interaction between the tank circuit and the SQUID ring affects the dynamic resistance of the junction.

Using Eqs. (11) and (41), and thus including the mutual interaction between the SQUID and the tank circuit, the normalized peak voltage across the tank circuit can be put into the form¹²³

$$\hat{\varphi}_e \approx \hat{\varphi}_{rf} + g_L \left[\frac{(\delta_L + \gamma)}{1 + \delta_L^2} F(\hat{\varphi}_e, \varphi_a) - \frac{2(\delta_L + \beta_a)}{\omega_B(1 + \delta_L^2)^2} \frac{\partial F(\hat{\varphi}_e, \varphi_a)}{\partial \varphi_a} \right] \quad (43)$$

where the substitution $\beta_a = \gamma(1 - \delta_L^2)/2$ is used; ω_B is half of the bandwidth of the loaded tank circuit: $\omega_B = \omega_L/2Q_L$. $F(\hat{\varphi}_e, \varphi_a)$, g_L , $\hat{\varphi}_{rf}$, and γ are defined in Sec. 3.2.2. The peak voltage \hat{V}_T can be estimated from Eq. (43) since $\hat{V}_T = \omega_p L_T \Phi_0 \hat{\varphi}_e / (2\pi M)$. The value of g_L separates the problem into two parts: in the weak-coupling limit, $g_L < 1$, $\hat{\varphi}_e$ and thus \hat{V}_T can directly be estimated by substituting $\hat{\varphi}_{rf}$ for $\hat{\varphi}_e$ in the right-hand side of Eq. (43), with $\hat{\varphi}_{rf}$ representing the rf excitation not disturbed by the nonlinear response of the SQUID; in the strong-coupling regime, $g_L > 1$, this method is applicable only at very high values of \hat{I}_{rf} . The R-SQUID dynamics in the weak-coupling limit has been analytically examined by Seppä.⁴⁴ The computer simulations by Erné and Luther¹²⁴ and by Van Veldhuizen and Fowler¹²⁵ cover both regions as well as the special case $\beta_L > 1$. The suitability

of the different models for the noise thermometer is discussed by Soulen and Van Vechten.⁴⁵

If the R-SQUID is applied to accurate voltage, current, or temperature measurements, the dynamic impedance must be determined. Adequate precision is obtained by inserting $\hat{\phi}_e$, found from Eq. (43), into Eqs. (41) and (42), which leads to a differential equation similar to Eq. (41), but with much more complicated Fourier coefficients. Peterson¹²⁶ derived the dynamic impedance without and Seppä¹²³ with the influence of the tank circuit. If $\beta_L \ll 1$, $\hat{\phi}_e \approx \hat{\phi}_{rf}$ and only the first component of the Fourier series, $g_0 = J_0(\hat{\phi}_e)$, remains. In that case it is found from Eq. (41) that $\rho^2/R^2 = \langle \hat{\phi}_a \rangle^2 / \omega_R^2 \approx 1 - (I_c/I_0)^2 J_0^2(\hat{\phi}_{rf})$. The dynamic impedance ρ is equal to R if either I_0 or $\hat{\phi}_{rf}$ are high. Both bias currents heat up the shunt resistor and the Josephson junction, which makes it difficult to determine the value of the shunt resistor R without a model of the dc impedance.

3.5.3. Noise Properties of the R-SQUID

As a first approximation, the R-SQUID can be considered to be a Josephson junction with the critical current reduced by the rf excitation. Consequently, following the noise calculations by Likharev and Semenov¹²⁷ for the heavily damped Josephson junction, an estimate for the frequency fluctuation was found by Giffard *et al.*¹²⁸

Frequency fluctuations in the R-SQUID were examined more accurately in Ref. 44, where Eq. (41) was analyzed with noise sources introduced by the shunt resistor and by dissipations in the tank circuit. If the influence of SQUID parameters on the frequency variance σ_f^2 is made negligibly small by proper adjustment of $I_c/I_0 \ll 1$ and $J_0(\hat{\phi}_{rf}) \approx 0$, the Allan variance can be given as

$$\sigma_f^2 = \frac{\sum_{n=1}^N (f_{i+1} - f_i)^2}{2N} = \sigma_T^2 \left[1 + \frac{1}{2} g_L \frac{\omega_R T_{eq}}{\omega_p T} \sum f_n^2 \right] \quad (44)$$

where

$$\sigma_T^2 = \frac{2k_B RT}{\Phi_0^2 \tau} \quad \text{and} \quad f_n^2 = \left(\frac{\partial g_n}{\partial \hat{\phi}_e} \right)^2 \approx 4 \frac{J_n^2(n\beta_L)}{n^2 \beta_L^2} J_1^2(\hat{\phi}_{rf}) \quad (45)$$

Here T_{eq} denotes the effective tank circuit temperature and τ is the gate time of frequency counting. Since the SQUID parameters and the tank circuit temperature are inaccurately known, T_{eq} gives rise to a systematic error in the temperature measurement. In addition, it turns out that the signal-to-noise ratio of the detected audio signal depends on SQUID parameters via g_L and $J_1(\hat{\phi}_{rf})$, just as the mixed-down noise does. On the other hand, a poor signal-to-noise ratio increases the frequency variance¹²⁹ and, therefore, a compromise is necessary. The noise can be reduced by feeding

the audio signal through a narrow bandpass filter; however, the filter affects the frequency variance. Including all sources of error discussed previously, Seppä¹³⁰ has shown that under optimum conditions the R-SQUID noise thermometer measures temperature with relative uncertainty $E_t = [N^{-1}(T_A/T)]^{2/7}$, where N is the number of periods in the pump signal

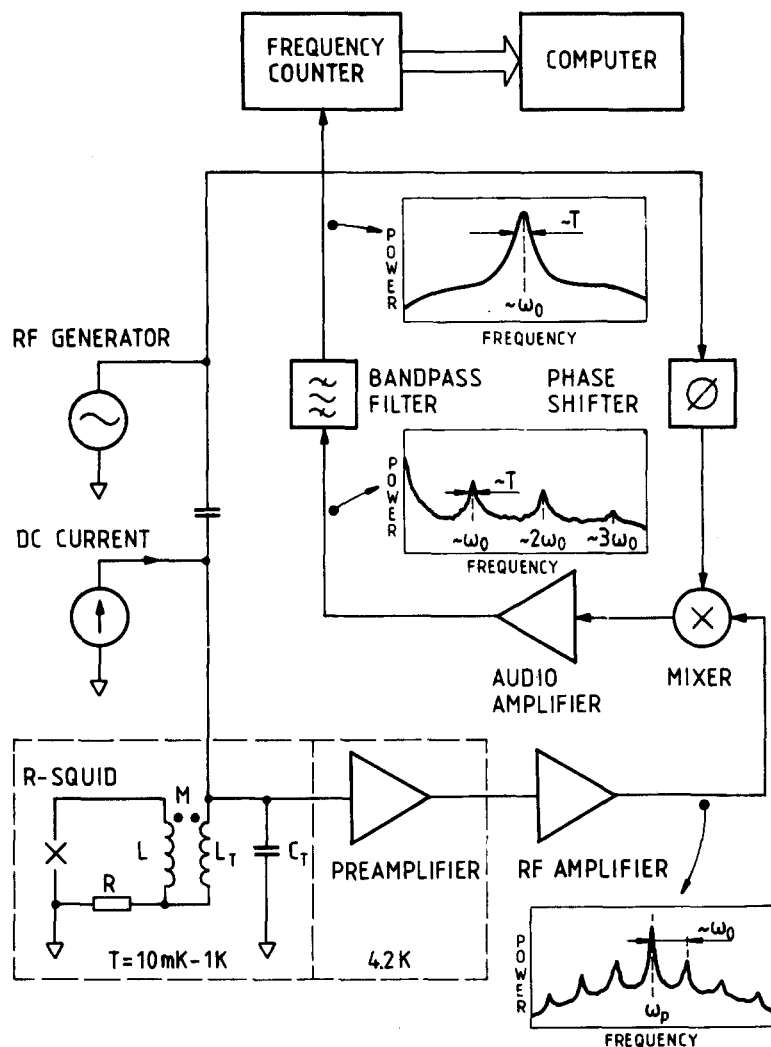


Fig. 11. Schematic diagram of a complete R-SQUID noise thermometer with a post-detection filter, counter, and a computer. The frequency spectrum of the signal is shown in the insets for different stages of the system.

during the measurement time Y , $N = Y\omega_p$. The optimized value is thus independent of SQUID parameters. The calculations predict that at sufficiently high temperatures ($T \geq 1\text{K}$), the R-SQUID, coupled to a low-noise preamplifier and operated at maximal pump frequency, can determine the temperature with an uncertainty of $E_i \approx (Y\omega_c)^{-2/7}$. In a typical point-contact SQUID, $\omega_c \approx 2\pi \times 1\text{ GHz}$ and thus a measurement time $Y = 1\text{ hr}$ leads to the relative uncertainty of $1.5 \cdot 10^{-4}$. A complete R-SQUID noise thermometer with a post-detection filter, a counter, and a computer is depicted in Fig. 11; the inset figures show the frequency spectra of the signal in different parts of the system.

3.5.4. Discussion

As a thermometer, the rf-biased R-SQUID will continue to have metrological interest for a long time. It should be emphasized here that the rf SQUID and the dc SQUID are also suitable for monitoring thermal noise from small resistors. Thus they can measure the absolute temperature^{86,131,132}; they can also be applied for the measurement of the temperature-dependent susceptibility of a dilute salt.¹³¹ Erné *et al.*¹³³ suggested that a resistive dc SQUID could be used to determine the temperature but noise of this system has not been analyzed. The discovery of high- T_c materials enables, in principle, an expansion of the temperature range up to 100 K, but possible extra sources of noise associated with the granular superconducting materials and flux creep may cause problems.

4. DOUBLE-JUNCTION (dc) SQUIDS

4.1. Operation

4.1.1. Model of an Autonomous dc SQUID

Particularly for applications involving the simultaneous use of multiple magnetometers, the dc SQUID^{10-12,134-138} seems to be the most suitable device. However, the design and fabrication of thin-film tunnel-junction dc SQUIDs have been more difficult than the basic idea of dc-SQUID dynamics suggests. Several studies^{137,139-146} indicate problems in coupling the dc SQUID to its input coil, emphasizing the importance of including the whole device in the analysis.^{147,148}

We start with a simple autonomous dc SQUID, i.e., a symmetrical superconducting loop with two identical Josephson junctions as shown in Fig. 12. In principle, the dc SQUID can be operated by measuring either the average voltage \bar{V} , as a function of the external magnetic flux Φ_a with constant bias current I , or the average current with constant bias voltage.

To develop differential equations describing the dynamics of the dc SQUID we note that^{12,149,150}:

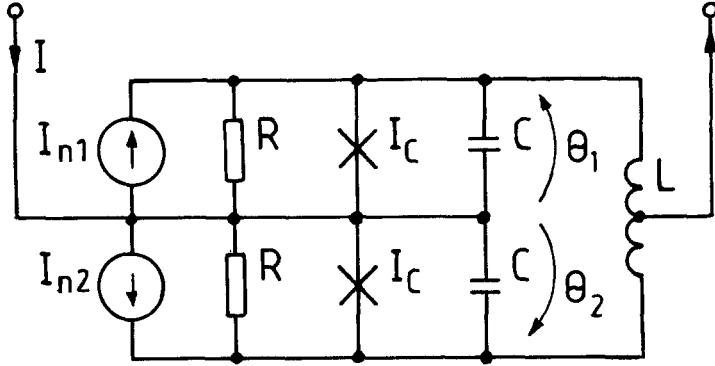


Fig. 12. Equivalent circuit of the dc SQUID. The ideal Josephson junctions are characterized by the critical current I_c ; both are shunted by capacitance C and resistance R that have thermal noise generators I_{n1} and I_{n2} . I is the bias current and L is the loop inductance of the SQUID.

- 1) the current I_i through junction i , $i = 1, 2$, is given by the RSJ model (see Eq. (4))

$$I_i = \frac{\hbar}{2e} C \frac{d^2\theta_i}{dt^2} + \frac{\hbar}{2eR} \frac{d\theta_i}{dt} + I_c \sin \theta_i + I_{ni} \quad (46)$$

- 2) the total current through the device is $I = I_1 + I_2$, and
- 3) the magnetic flux threading the ring (see Eq. (10)) is

$$\Phi = \frac{\Phi_0}{2\pi} (\theta_1 - \theta_2) = \Phi_a + L(I_1 - I_2)/2 \quad (47)$$

where C , R , and I_c denote the junction capacitance, resistance, and critical current, respectively. L is the inductance of the ring, and I_{ni} is the thermal noise current of shunt resistor R_i . The macroscopic superconducting state of the ring is characterized by the phase differences θ_i .

Let $\nu = (\theta_1 + \theta_2)/2$ and $\varphi = (\theta_1 - \theta_2)/2$. Then the instantaneous voltage over the two junctions is $V = RI_c d\nu/dt^*$ and the total flux is $\Phi = \Phi_0 \varphi / \pi$, where $t^* = 2\pi R I_c t / \Phi_0$ is the dimensionless time. (Note that the scaling is different from that of the rf-SQUID equations and that the change of variables does not conserve the length.) Using β_c and β_L defined in Sections 2.1 and 2.2, we can write the equations of motion for the dc SQUID as follows:

$$\beta_c \frac{d^2\nu}{dt^{*2}} + \frac{d\nu}{dt^*} + \sin \nu \cos \varphi = i + i_{n,\nu}(t^*) \quad (48)$$

$$\beta_c \frac{d^2\varphi}{dt^{*2}} + \frac{d\varphi}{dt^*} + \cos \nu \sin \varphi + \frac{2}{\beta_L} (\varphi - \varphi_a) = i_{n,\varphi}(t^*) \quad (49)$$

where $i = I/2I_c$ and $\varphi_a = \pi\Phi_a/\Phi_0$. The Langevin functions for ν and φ , $i_{n,\nu}$ and $i_{n,\varphi}$, represent thermal noise, characterized by $\langle i_{n,\nu}(t^*) \rangle = \langle i_{n,\varphi}(t^*) \rangle = 0$, $\langle i_{n,\nu}(t^* + \tau^*) i_{n,\nu}(t^*) \rangle = \langle i_{n,\varphi}(t^* + \tau^*) i_{n,\varphi}(t^*) \rangle = \Gamma \delta(\tau^*)$, and $\langle i_{n,\nu}(t^*) i_{n,\varphi}(t^*) \rangle = 0$.^{38,41} Γ is the noise-rounding parameter as defined in Sec. 2.1.

4.1.2. Simplified Model of the dc SQUID

The analysis of the nonlinear second-order differential equations (48) and (49) is very cumbersome and requires the use of computer simulations^{149–151} or approximations^{152,153} in the overdamped limit, $\beta_c \ll 1$, where the equations can be expanded as a series from which the voltage, the circulating current, and the transfer function $\partial \bar{V}/\partial \Phi_a$ can be estimated.

If the SQUID loop inductance is negligible, i.e., $\beta_L \ll 1$, and $\beta_c \approx 0$, the total flux of the ring $\Phi \approx \Phi_a$, and according to Eq. (48) the voltage $V \approx RI_c(i - \cos \varphi_a \sin \nu)$. Integrating V over the period τ of the Josephson oscillation, the average voltage over the current-biased SQUID is obtained⁷:

$$\bar{V} = \frac{1}{\tau} \int_0^\tau V dt \approx \frac{RI}{2} \left[1 - \left(\frac{2I_c}{I} \cos \frac{\pi \Phi_a}{\Phi_0} \right)^2 \right]^{1/2} \quad (50)$$

The dc SQUID thus behaves like a single Josephson junction with resistance $R/2$ and an effective flux-dependent critical current $I_{c,\text{eff}} = 2I_c \cos(\pi\Phi_a/\Phi_0)$. The modulation depth of the critical current is thus $\Delta I_{c,\text{eff}} = 2I_c$ for $\beta_L = 0$.

Because thermal noise rounding was neglected, the approximate characteristics do not yet indicate the actual transfer function. For an estimate, we differentiate Eq. (50) at $\Phi_a = \Phi_0/2$ and $I = 2I_c$, which approximates the practical point of operation in the flux-locked-loop mode.^{12,138} To relax the assumption $\beta_L = 0$ we note, on the basis of RSJ-model simulations¹² (see also Fig. 15), that $\Delta I_{c,\text{eff}}(\beta_L = \pi) \approx 0.5 \cdot \Delta I_{c,\text{eff}}(\beta_L = 0) \approx I_c$. Thus $\partial \bar{V}/\partial \Phi_a \propto \Delta I_{c,\text{eff}}$ is reduced approximately by a factor of 2 for $\beta_L = \pi$. We then obtain

$$\frac{\partial \bar{V}}{\partial \Phi_a} \approx \frac{R}{2L} \quad (51)$$

In a similar way, the dynamic resistance is found from Eq. (50);

$$R_{\text{dyn}} = \frac{\partial \bar{V}}{\partial I} \approx \frac{R}{\sqrt{2}} \quad (52)$$

These approximations for R_{dyn} and $\partial \bar{V}/\partial \Phi_a$ are useful in evaluating the energy resolution of the dc SQUID.

The dc SQUID can also be described by its dynamic input impedance. At low frequencies the device behaves almost like an ideal parametric amplifier with a flux-dependent input inductance; at higher frequencies resistive losses occur. No external pump signal is used: the dc SQUID is a self-pumped up-converter, where the signal power appears as sidebands

of the Josephson oscillation, and some of the properties resemble those of the L-SQUID. Measurements of the dynamic input impedance¹⁵⁴ have revealed a negative input resistance for some values of the applied flux, which cannot be explained on the basis of the RSJ model of the autonomous dc SQUID. A possible explanation is the influence of the signal-coil resonances (see Sec. 4.2).

4.1.3. Dynamics of the dc SQUID

Equations (48) and (49) that describe the dynamics of the dc SQUID are analogous to the equation of motion of a point mass in a force field with the potential energy^{149,150}

$$U(\nu, \varphi) = \frac{1}{\beta_L} (\varphi - \varphi_a)^2 - i\nu - \cos \nu \cos \varphi \quad (53)$$

$U(\nu, \varphi)$ describes a tilted parabolic trough with sinusoidal bumps. This analogy helps to understand the dynamics of the dc SQUID without solving Eqs. (48) and (49).

Figure 13a shows $U(\nu, \varphi)$ with $i=0$ and $\varphi_a=0$; on the bottom of the trough there is a periodic chain of minima and maxima. Figures 13b and 13c illustrate the effect of external flux φ_a . Changing φ_a from 0 to $\pi/2$ causes the bottom of the trough to shift from the line $\varphi=0$ in Fig. 13a to $\varphi=\pi/2$ in Fig. 13c, forming a serpentine path in connecting the minima along the trough. The movement of the particle in the ν direction implies oscillations in the φ direction, i.e., every voltage state with $\varphi_a=\pi/2$ is accompanied by oscillations of the total flux and hence of the current circulating in the ring. Figures 13b and 13c show that the oscillations are symmetric with respect to the line $\varphi=0$ when $\varphi_a=\pi/2$, and asymmetric when $\varphi_a=\pi/4$.

The effect of the bias current i is shown in Fig. 13d: the potential trough is tilted in the direction of increasing ν , and the saddle points between the minima are lowered. The critical value of the bias current, at which the motion of the particle starts, depends on β_L and φ_a .

Figure 14 shows the voltage v and the circulating current j in the SQUID ring, obtained from a numerical solution of Eqs. (48) and (49) at $i=1$. In the absence of an external field, v has peaks corresponding to jumps over the saddle points of the potential surface, and the circulating current is zero, i.e., the SQUID behaves like a single Josephson junction. When a small external flux threads the SQUID loop, the circulating current starts to oscillate as shown in Fig. 14a. At $\varphi_a=\pi/2$ the voltage and current are symmetric as in Fig. 14c; in Fig. 14b, where $\varphi_a=\pi/4$, the oscillations are asymmetric, in agreement with the qualitative picture discussed previously.

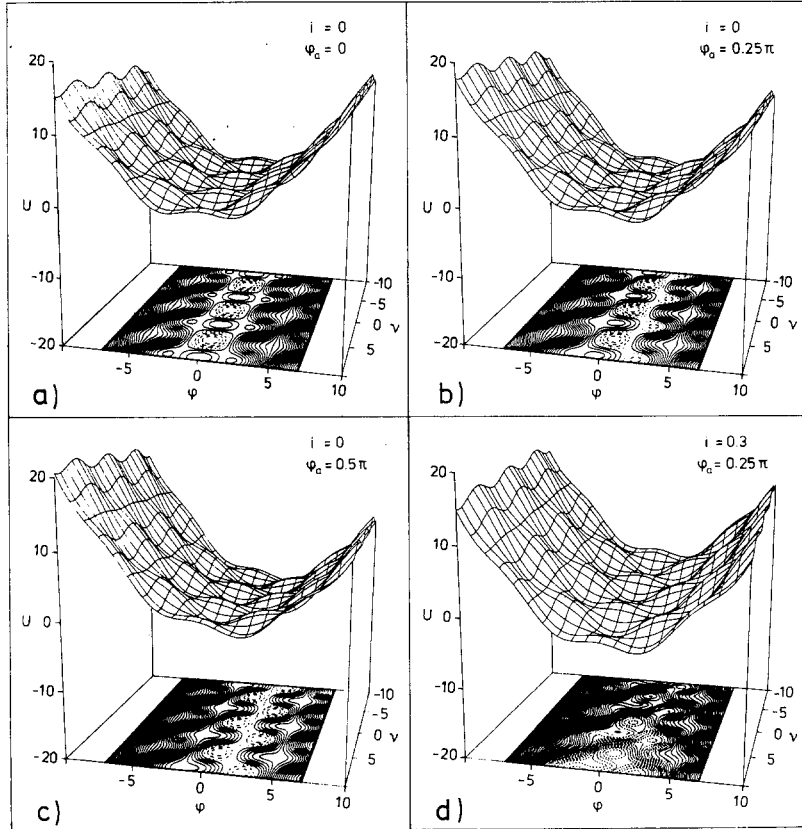


Fig. 13. Potential energy U of the dc SQUID for different values of the bias current i and the external flux φ_a . U is also displayed as an isocontour projection map.

The oscillation frequencies are typically of the order of 10 GHz; only the time average \bar{v} is observed. The $i\bar{v}$ and $\varphi_a\bar{v}$ characteristics are obtained by averaging the numerical solutions of the RSJ model over the period of oscillations. In Fig. 15 we show the $i\bar{v}$ characteristics for $\beta_L = \pi$ and $\beta_c = 0.3$. In comparison with the analytical approximation of Eq. (50), a realistic value of inductance reduces the modulation depth; for $\varphi_a = \pi/2$ a voltageless state of supercurrent exists. As $\beta_L \rightarrow \infty$, Eq. (49) becomes independent of external flux, i.e., increasing inductance diminishes the modulation depth. Figure 16 shows the periodic behavior of the dimensionless voltage \bar{v} as a function of φ_a ; the result is qualitatively similar to the analytical approximation.

The form of the potential energy function suggests that a higher value of β_L gives more freedom of motion in the φ direction. Increasing β_c , which

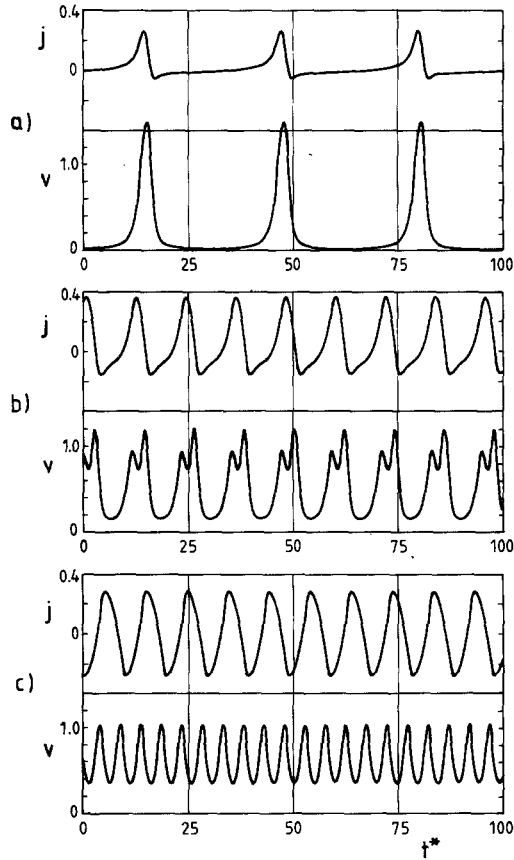


Fig. 14. Numerically calculated circulating current $j = (\varphi - \varphi_a)/\beta_L$ and voltage v across a dc SQUID for the bias current $i = 1.0$, as a function of time with different values of external flux. (a) $\varphi_a = 0$; (b) $\varphi_a = \pi/4$; (c) $\varphi_a = \pi/2$. The units of the circulating current and the voltage are $2I_c$ and RI_c , respectively.

is analogous to the mass of the particle, introduces more inertia into the dynamics; for small values of β_L and β_c , the particle follows the path of smallest dissipation^{155,156} between the minima, and the dynamics of the dc SQUID is straightforward. Higher values of β_L and β_c create much more complex behavior,^{149-151,157-159} leading to multiple voltage states and sometimes even to chaos.

Figure 17 shows the $i\bar{v}$ characteristics of the dc SQUID with increasing values of β_c and β_L . The increased inertia gives rise to a qualitatively new feature: the curves seem to form plateaus around the bias current level $i = 1$.

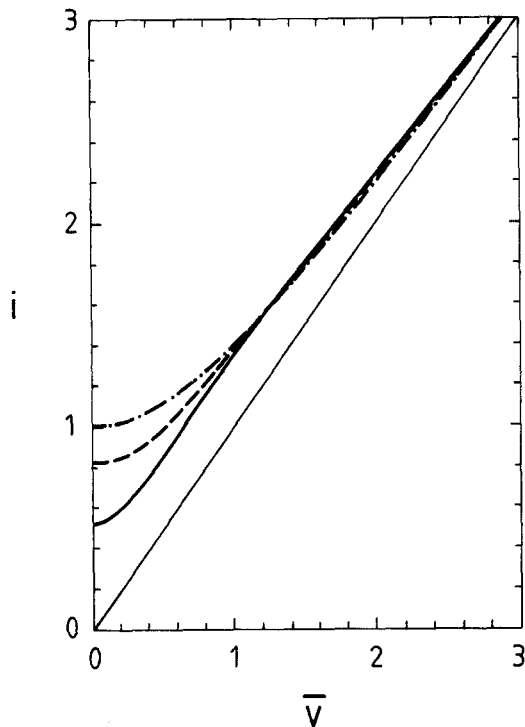


Fig. 15. Current-voltage characteristics of the dc SQUID with $\beta_L = \pi$ and $\beta_c = 0.3$. The thick solid line represents external flux value $\varphi_a = 0.5\pi$; the dashed line, $\varphi_a = 0.25\pi$; and the dash-dotted line, $\varphi_a = 0$. The diagonal line depicts the resistive curve of the dc-SQUID loop, $V = RI/2$.

This behavior can also be understood on the basis of LC resonances in the SQUID ring: a resonance at the frequency ω implies a tendency to lock onto the voltage level $\bar{V} = \omega\Phi_0/2\pi$. Figure 17b also illustrates the decrease of the modulation depth with increasing β_L .

The effect of relatively high values of β_c and β_L is shown in Fig. 17c. An interesting new feature emerges: the $i\bar{v}$ curves are divided into different branches connected by hysteresis loops, leading to multiple solutions with the same set of parameters.^{149,150,160,161} A division into three different types of solutions is found; in the case of zero external flux the classification of the solutions is straightforward:¹⁵⁰

- 1) Zero-voltage solution: $v = v_0 = \text{constant}$ and $\varphi = 0$. The particle is trapped into a minimum of the potential; for large values of β_L minima can exist also for $\varphi \neq 0$.

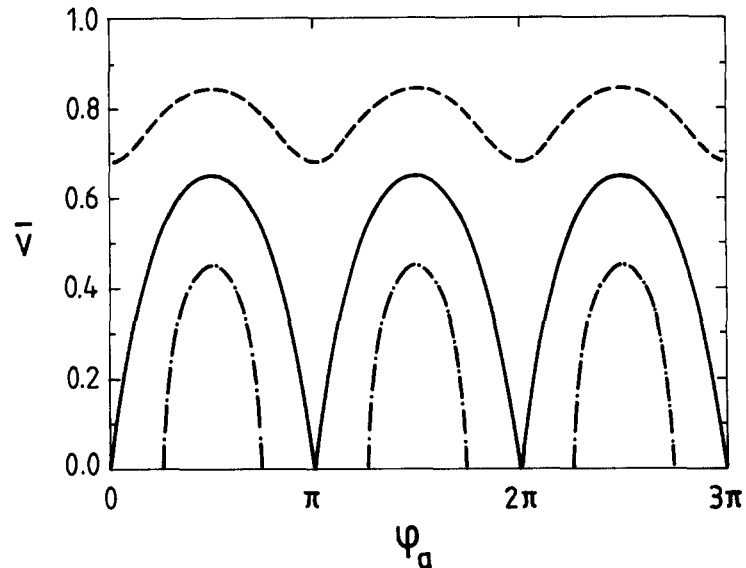


Fig. 16. Voltage vs. external flux characteristics of the dc SQUID with $\beta_L = \pi$ and $\beta_c = 0.3$. The dash-dotted line represents the bias current $i = 0.8$; the solid line, $i = 1.0$; and the dashed line, $i = 1.2$.

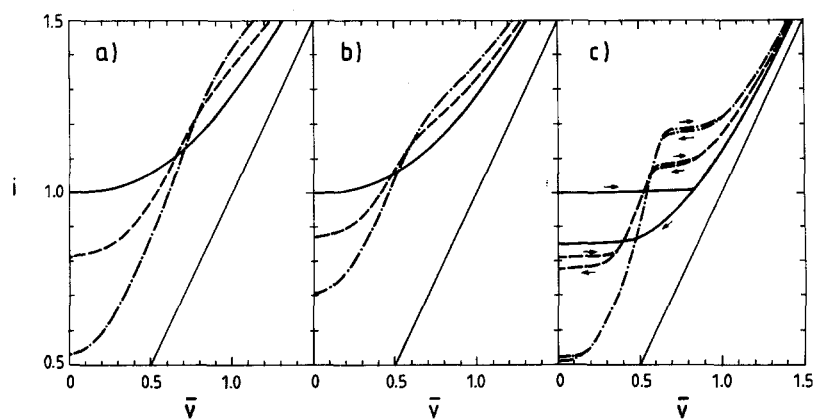


Fig. 17. Current-voltage characteristics for the dc SQUID. The solid lines represent the external flux $\varphi_a = 0$; the dashed lines, $\varphi_a = 0.25\pi$; the dash-dotted lines, $\varphi_a = 0.5\pi$. (a) The characteristics for $\beta_c = 0.7$ and $\beta_L = \pi$; (b) $\beta_c = 0.7$ and $\beta_L = 2\pi$; and (c) $\beta_c = 1.6$ and $\beta_L = \pi$. Hysteresis loops are indicated by arrows.

2) Running solution: $\nu = \omega_j^*(\beta_c, i)t^* + f(t^*)$, with $f(t^* + 2\pi/\omega_j^*) = f(t^*)$ and $\varphi = 0$, where ω_j^* is the dimensionless characteristic frequency of the oscillation. In the absence of external flux, the motion of the particle is along the bottom of the potential trough, and β_L does not influence the dynamics.

3) Beating solution: $\nu = \omega_j^*(\beta_L, \beta_c, i)t^* + f(t^*)$, with $f(t^* + 2\pi/\omega_j^*) = f(t^*)$ and $\varphi = g(t^*)$, with $g(t^* + 2\pi/\omega_j^*) = -g(t^*)$. The particle moves symmetrically in the φ direction as well; the dynamics thus depends on β_L , β_c , and i .

For $\varphi_a \neq 0$ a classification of the solutions is difficult, since motion in the φ direction exists in both beating and running cases. Figures 17a and 17b reveal the failure of the classification; two qualitatively different modes of operation obviously exist but with no clear separation. The beating solution is, however, characterized by current oscillations of larger amplitude and by lower average voltage. With hysteresis the problem of classification disappears.

4.1.4. Effect of Thermal Noise

In nonlinear devices, thermal noise has a drastic influence on the dynamics. With noise included, dc-SQUID behavior has been analyzed for $\beta_c \ll 1$ ^{12,162} or the optimization of β_c and β_L has been accomplished with a hybrid computer.¹⁶³ Digital simulations of complete dc-SQUID equations have concentrated on qualitative aspects.^{141,144,147,148,151,164}

The effect of noise on SQUID dynamics can be understood in terms of Brownian motion of a particle in a nonlinear force field.^{38,40,41,90,149,157,165-171} The classical problem⁴⁰ is to study the thermally activated motion of the particle over the potential barrier separating the minima, as shown in the inset of Fig. 18. The motion due to thermal noise can be simulated as random collisions with small particles in thermal equilibrium. Figure 18 illustrates the two-dimensional dc-SQUID potential energy with minima and saddle points.

For multidimensional systems, such as the dc SQUID, the activation time τ_e is defined to be the average time the particle needs to reach the borderline of the potential minimum: $\tau_e^{-1} \approx \omega_{\text{eff}}^{-1} e^{-\Delta U_{\text{eff}}/k_B T}$. Here, the effective attempt frequency ω_{eff} , which depends on the damping of the system and on the form of the potential energy, and the effective barrier height ΔU_{eff} differ from Kramers' one-dimensional approximations.^{40,157,172,173} In addition, some macroscopic quantum tunneling experiments with unshunted junctions in dc SQUIDs¹⁷⁴ indicate a significantly higher effective barrier for thermal activation. In principle, the model allows the calculation of the critical bias current.¹⁷⁰ Qualitatively, thermal noise affects the $\varphi_a \bar{v}$ and $i \bar{v}$ characteristics by rounding the point where the voltage

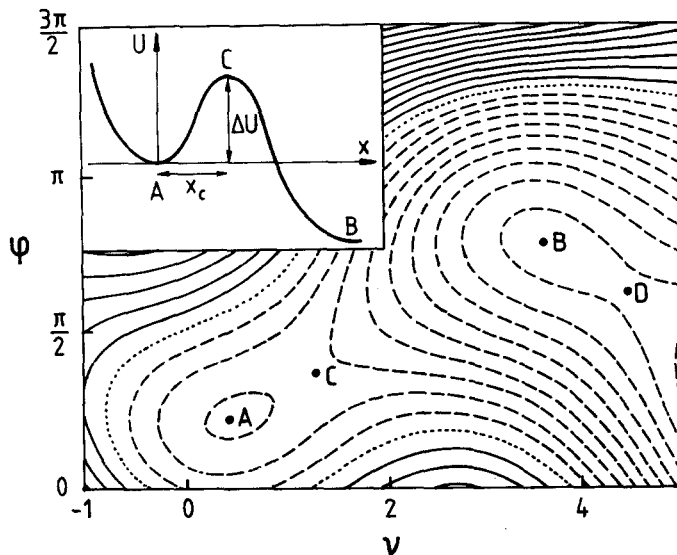


Fig. 18. Contour map representing the dc-SQUID potential energy surface. Points A and B are local minima; points C and D are saddle points. To move from A to B, the particle has to cross the barrier near the saddle point C. The two-dimensional thermal activation problem is similar to the classical activation problem of Kramers, which is shown in the inset.

state emerges. Figure 19 shows noisy $i\bar{v}$ curves for $\beta_L = 2\pi$, $\beta_c = 0.7$, and $\Gamma = 0.01$, together with the corresponding $i\bar{v}$ characteristics of a single Josephson junction. Although the noiseless characteristics of a single junction and those of a dc SQUID without external flux are similar in the units of Fig. 19, thermal noise causes the scaled voltage of the dc SQUID to be lower because of an extra degree of freedom.

The multiple solutions of the dc-SQUID equations indicate the existence of separate basins of attraction in the phase space.¹⁷⁵⁻¹⁷⁷ Every set of initial conditions leads the dissipative system to a particular running, zero-voltage, or beating solution. Thermal noise can be regarded as a random generator influencing the initial conditions for each time instant; depending on its thermal energy, the system has some probability for hopping between different voltage states.^{38,42,149,151,157,169,178-182} Because of thermal noise, hysteresis of the characteristics thus disappears or the hysteresis loops are rounded. On the other hand, the fluctuations between different states increase the noise of the system.

Figure 20a shows the $\varphi_a \bar{v}$ characteristics for a dc SQUID with $\beta_L = \pi$ and $\beta_c = 1.6$ (compare Fig. 17c), calculated for $i = 0.75, 0.9$, and 1.1 . When $i < 1$, the point where the voltage state emerges is hysteretic. The separation

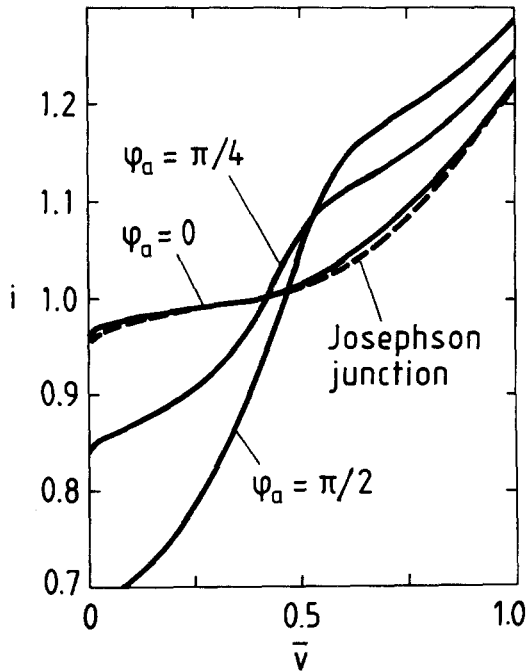


Fig. 19. Current-voltage characteristics of a dc SQUID, with $\beta_c = 0.7$ and $\beta_L = 2\pi$ (see Fig. 17b) with $\Gamma = 0.01$. The solid lines represent the dc-SQUID curves calculated for $\varphi_a = 0, \pi/4$, and $\pi/2$; the dashed line is the voltage-current characteristics of a single Josephson junction with $\beta_c = 0.7$. For the Josephson junction the bias current is scaled by I_c , while for dc-SQUID the scaling factor is $2I_c$.

between the beating and the running branches is also hysteretic. Figure 20b represents noisy characteristics for three different temperatures. In the case of hysteresis, the voltage value is an average of the different voltage states. This is shown in the inset of Fig. 21 for $i = 0.75$, $\varphi_a = 0.3\pi$, and $\Gamma = 0.05$. The voltage distribution has two peaks, corresponding to the zero-voltage state and the running state. The distribution is calculated after integration over an oscillation period of the system; the corresponding voltage power spectral density, $S_v(0) \approx 1.0$, is shown in Fig. 21. Similar results have been published in Refs. 151 and 163.

4.1.5. Energy Resolution of the Autonomous dc SQUID

The external flux is normally coupled to a dc SQUID via a flux transformer, which allows measurements from a bigger volume. The minimum field energy per unit bandwidth in the input coil ϵ , measurable

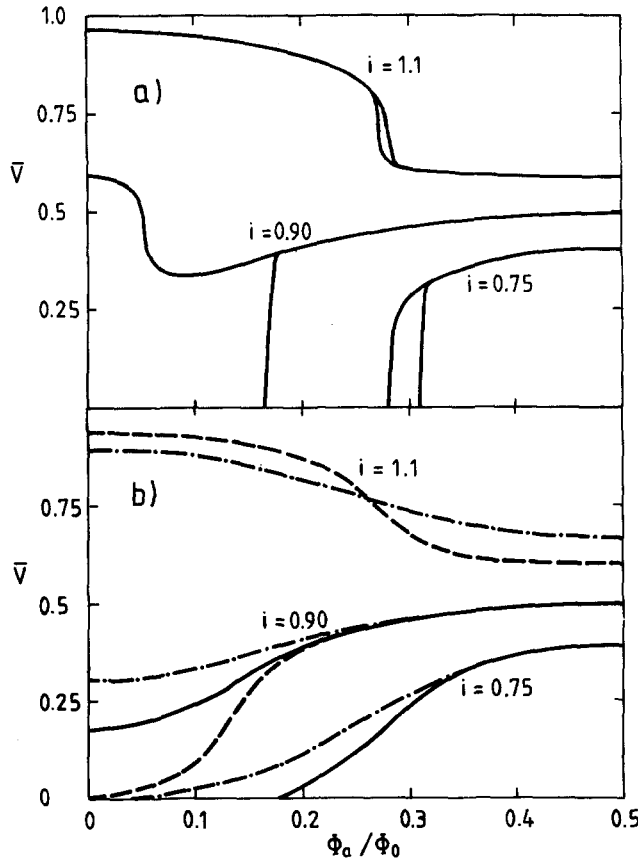


Fig. 20. Voltage vs. external flux characteristics of a dc SQUID with $\beta_c = 1.6$ and $\beta_L = \pi$ at three currents, $i = 0.75, 0.9$, and 1.1 . (a) Noiseless characteristics, where different branches of voltage exist. (b) The effect of thermal noise on characteristics at three different temperatures; the dashed lines correspond to $\Gamma = 0.02$, the solid lines to $\Gamma = 0.05$, and the dash-dotted lines to $\Gamma = 0.1$.

by the SQUID (see Eq. (28)), is thus an appropriate figure of merit.¹⁸³ Following the formalism of Sec. 3.2.3, the equivalent spectral density of the voltage noise power in the input of the preamplifier is

$$S_V \approx \left(\frac{\partial \bar{V}}{\partial \Phi_a} \right)^2 S_\Phi + 4k_B R_{\text{dyn}}^2 \left(\frac{T}{R_{\text{dyn}}} + \frac{1}{2} \frac{T_A}{R_{\text{opt}}} \right) + 2k_B T_A R_{\text{opt}} \quad (54)$$

where $S_\Phi = L^2 4k_B T / (2R)$ is the spectral density of the intrinsic flux noise

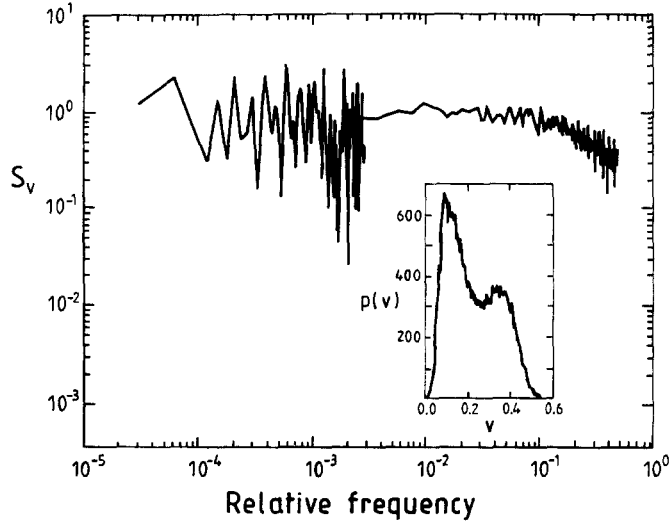


Fig. 21. Voltage noise power spectral density of the SQUID of Fig. 20 at $\varphi_a = 0.3\pi$, $i = 0.75$, and $\Gamma = 0.05$, as a function of frequency relative to the Josephson frequency. The apparent break in the curve around the relative frequency $2 \cdot 10^{-3}$ arises from a change in the treatment of the data. At high frequencies, 64 runs of $512 \times 2\pi$ were averaged as Fourier components. At low frequencies, the full length of $64 \times 512 \times 2\pi$ runs is Fourier transformed. Inset: Probability distribution of the voltage according to the data used for the above voltage noise spectrum (arbitrary units).

of the ring and the second term is the thermal noise voltage across the SQUID, including also the contribution of the preamplifier with a noise temperature T_A . The third term represents the equivalent voltage noise of the preamplifier, where R_{opt} is its optimal source impedance. In Eq. (54) a general theory for the noise in the nonlinear resistance^{184,185} is applied, using the first term of the Taylor expansion of the power dissipation, i.e., $R_{\text{dyn}} = \partial \bar{V} / \partial I$; the approximation can be further improved by including higher-order terms. The energy resolution of the dc SQUID can be written from Eq. (54) as

$$\varepsilon = \frac{S_V}{2L(\partial \bar{V} / \partial \Phi_a)^2} \approx \frac{k_B T}{L} \left\{ \frac{L^2}{R} + \frac{2R_{\text{dyn}}}{(\partial \bar{V} / \partial \Phi_a)^2} \left[1 + \frac{1}{2} \frac{T_A}{T} \left(\frac{R_{\text{dyn}}}{R_{\text{opt}}} + \frac{R_{\text{opt}}}{R_{\text{dyn}}} \right) \right] \right\} \quad (55)$$

Here, the contribution of the amplifier is reduced to the input coil. Equation (55) shows that the contribution of the preamplifier on ε is minimized when $R_{\text{opt}} = R_{\text{dyn}}$. In practice, noise matching^{186,187} is achieved with a cooled transformer (see Sec. 7.5). Applying approximations (51) and (52) for $\beta_L = \pi$ and neglecting amplifier noise, the energy resolution becomes $\varepsilon \approx$

$6.7k_B T(L/R)$. Furthermore, setting $\beta_c = \beta_L/\pi = 1$, we find $\varepsilon \approx 12k_B T(LC)^{1/2}$.

For the dc SQUID, the forward transfer frequency \mathcal{F} , defined by Eq. (29), is

$$\mathcal{F} = \frac{2L}{R_{\text{dyn}}} \left(\frac{\partial \bar{V}}{\partial \Phi_a} \right)^2 \approx \frac{R}{\sqrt{2}L} = \frac{\omega_c}{\sqrt{2}} \quad (56)$$

where $\omega_c = R/L$ is the characteristic frequency of the SQUID and the approximations (51) and (52) are used. For single-junction SQUIDs, both inductive and hysteretic, \mathcal{F} is proportional to the pump frequency ω_p , which is normally 2-3 orders of magnitude below ω_c . Thus \mathcal{F} is much higher for dc SQUIDs than for other types of sensors; the double-junction device appears superior. For $L = 80$ pH and $R = 5 \Omega$ we find $\mathcal{F} \approx 2\pi \times 7$ GHz. Only the microwave SQUID with $\omega_p \sim \omega_c$ or the L-SQUID, tuned to nearly infinite gain, can have similar values of \mathcal{F} .

The sensitivity of the dc SQUID has been studied numerically, either ignoring the junction capacitance C ^{12,162} or with nonzero β_c .¹⁶³ The optimized energy resolution was found to be quite insensitive to β_L and β_c for $\pi < \beta_L < 2\pi$ and $1 < \beta_c < 2$, respectively. The optimum is $\varepsilon \approx 12k_B T(LC)^{1/2}$ for $\beta_L \Gamma < 0.1\pi$, i.e., $L < 580$ pH at 4.2 K or $L < 32$ pH at 77 K. Optimally, ε is about 25% less than in the overdamped case $\beta_c = 0$, where the unlimited bandwidth increases the mixing-down effect of noise. For $\beta_L \Gamma > 0.1\pi$, the energy resolution deviates from the above formula; when $\beta_L \Gamma \approx 0.3\pi$, ε is already twice the optimal value. The behavior of $\langle \Phi_n^2 \rangle^{1/2}$, i.e., $(2L\varepsilon)^{1/2}$ as a function of T for fixed values of L is illustrated in Fig. 28.

Figure 22 compares the numerically calculated energy resolution with the approximation based on Eq. (55). The $\varphi_a \bar{v}$ characteristics and the noise spectrum for an optimal dc SQUID are shown in Figs. 20 and 21. The high transfer function is achieved on the basis of hopping between multiple voltage states; within a very large range of parameters the increased transfer function compensates for the excess noise created by hysteresis. However, for $\beta_c \geq 3.0$, noise energy is already increasing; the optimal range of β_c and β_L has a clear upper limit.^{147,151,164}

The data depicted in Fig. 22 can be explained by two different factors. For $\beta_c \approx 1$, the energy sensitivity corresponds to Eq. (55), i.e., it is proportional to R^{-1} or $\beta_c^{-1/2}$, if C and L are kept fixed. When R is the free parameter, the mixing-down effect of noise finds its minimum roughly when $\beta_c \approx 1$; thus an increase or a decrease of β_c increases the noise. In addition, the excess noise of the system begins to dominate when the hysteresis limit, $\beta_c \approx 0.7$, is exceeded. At very high values of β_c , the excess noise due to hopping between multiple solutions or the chaotic behavior of the dc SQUID solely determines the deteriorated energy resolution of the device.

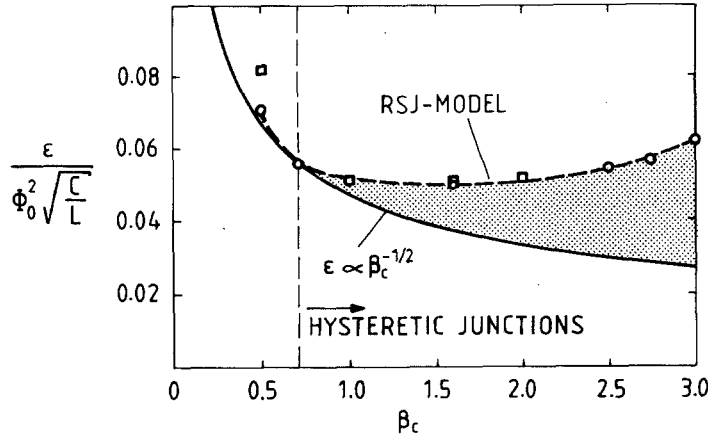


Fig. 22. Energy resolution ε as a function of β_c . The solid line represents the expected behavior of ε calculated from Eq. (55), where the junction capacitance C and the loop inductance L are fixed, $\beta_L = \pi$, and β_c is varied by altering R . The dashed vertical line refers to the critical value of β_c for hysteresis. The squares refer to the simulations of de Waal *et al.* with a hybrid computer,¹⁶³ and the circles to our simulations with a digital computer. The shading represents the noise rise, owing to hysteresis, mixing-down effect, and chaos at high β_c .

The optimal energy resolution $\varepsilon \approx 12k_B T(LC)^{1/2}$ at $\beta_c \approx 0.7$ can be roughly interpreted as the thermal energy ($k_B T/2$) divided by the effective noise bandwidth of the SQUID ($\omega_c/4$). We may thus conclude that a low-noise dc SQUID must have a small junction capacitance, a small loop inductance, and proper damping of the junctions.

4.1.6. Sensitivity of the dc-SQUID Magnetometer

So far, we have discussed only the intrinsic noise, although in practical applications the extrinsic noise, i.e., the equivalent noise in the input of the device, is more important. The SQUID is usually coupled to the external world via a flux transformer, characterized by three inductances: the detection coil L_d , the signal coil L_s , and the parasitic inductance of the connecting leads L_i . The integration of the input circuit and the dc SQUID on the same chip leads to precise control of these flux-transformer parameters and the coupling constant, enabling the optimization of the whole magnetometer configuration. The extrinsic energy sensitivity of the device can be written in the form^{183,188,189}

$$\varepsilon_{\text{ext}} = \frac{\langle \Phi_{n,\text{ext}}^2 \rangle}{2L_p} \approx \frac{1 - k_s^2 s_f}{k_s^2 s_f (1 - s_f)} \varepsilon_{\text{int}} \quad (57)$$

where k_s denotes the coupling constant between the signal coil and the SQUID loop and $s_f = L_s/(L_s + L_d + L_i)$ is the screening factor. Here $\varepsilon_{\text{int}} = \langle \Phi_{n,\text{eff}}^2 \rangle / 2L_{\text{eff}}$ is the intrinsic energy resolution of a coupled SQUID, calculated by replacing in Eq. (55) the geometric inductance L of the SQUID ring with the screened loop inductance $L_{\text{eff}} = (1 - k_s^2 s_f) L$.

As discussed in Sec. 4.1.5, the design of a low-noise dc SQUID tends to require very low loop inductances. In practice, the final limitation is the effective stray inductance L_{stray} of the SQUID loop, constrained by the fabrication technology. The geometric inductance L and the stray inductance L_{stray} are related by $L = L_{\text{stray}}/(1 - k_s^2)$. The optimization of the magnetometer can now be performed using Eqs. (55) and (57) with L_{eff} , by just fixing the fabrication parameters L_{stray} and C . The practical constrained optimization¹⁸⁹ also takes into account the minimum allowed linewidth, feasible film thicknesses, maximum resistivities of resistor foils, permittivities of the insulators, etc.

Instead of using approximations in Eq. (57), we can calculate R_{dyn} and $\partial \bar{V} / \partial \Phi_a$ from the simulated characteristics. On the basis of Figs. 1 and 17, R_{dyn} increases very rapidly as β_c grows and it thus compensates for the higher transfer function discussed in Sec. 4.1.5. R_{dyn} , possibly with higher-order terms, and $\partial \bar{V} / \partial \Phi_a$ are appropriate for optimization if their functional forms for a particular SQUID design are known; in practice, the calculation of R_{dyn} and $\partial \bar{V} / \partial \Phi_a$ can be as laborious as the direct optimization of ε_{int} .

Here we evaluate the sensitivity of the dc-SQUID magnetometer with approximations of Sec. 4.1.2 and with the dependence of the transfer function on β_L :^{12,189} $\partial \bar{V} / \partial \Phi_a \approx 7(RI_c/\Phi_0)(\pi + \beta_L)^{-1}$. According to Fig. 22, we set $\beta_c = 0.7$, which is below the hysteresis limit of junctions and gives low excess noise; for $\beta_c = 0.7$ the approximations also correspond well to the simulated energy resolution. If the dc SQUID is not intended for wideband use, the noise temperature of the preamplifier can be as low as 2 K (Sec. 7.5). Therefore, the contribution of the preamplifier to Eq. (55) is small when the noise-matching condition $R_{\text{opt}} = R_{\text{dyn}}$ is fulfilled. The numerical optimization of ε_{ext} thus leads to $\beta_L \approx 2.6\pi$, $k_s \approx 0.83$, and $s_f \approx 0.53$. Note that the coupling constant k_s is not a free parameter when the whole magnetometer is optimized. The screening factor s_f differs from the conventional optimization criterion¹⁸³ $L_s = L_d + L_i$ obtained for a tightly wound pickup coil. The optimal value of β_L is also higher than for the autonomous dc SQUID. If one is limited by technology to $C = 1 \text{ pF}$ and $L_{\text{stray}} = 20 \text{ pH}$, the optimal external and intrinsic energy resolutions at $T = 4.2 \text{ K}$ are $\varepsilon_{\text{ext}} \approx 4 \cdot 10^{-32} \text{ J/Hz}$ and $\varepsilon_{\text{int}} \approx 10^{-32} \text{ J/Hz}$, giving an intrinsic flux noise $\langle \Phi_{n,\text{eff}}^2 \rangle^{1/2} \approx 4.6 \cdot 10^{-7} \Phi_0/\text{Hz}^{1/2}$ for the effective SQUID inductance $L_{\text{eff}} \approx 40 \text{ pH}$. In practice, other noise sources deteriorate the performance (see Sec. 4.2 and 6.3).

4.2. Problems with Practical Devices

4.2.1. Origins of Parasitic Effects

The results of the simulations discussed above suggest that very-low-noise devices are possible; indeed, autonomous dc SQUIDs have been made that are within a factor of 2 of the quantum noise limit at 4.2 K.^{143,190-194} However, experimental results by several groups^{137,139,140,142,145,146,154,195} indicate difficulties with thin-film SQUIDs coupled to an input coil: new features in the dynamics are introduced. The optimization of the SQUID should thus include the input circuit.

Figure 23 illustrates a dc SQUID with an input coil. The SQUID loop is represented by a thin square washer (see Sec. 4.3.2), with the junctions shown as projecting edges of the plate; the signal coil is depicted as a two-turn microstrip line over the washer. The input coil introduces stray capacitance across the junctions, and its turns are capacitively connected mainly via the SQUID plate and at the crossings of the microstrip line. The capacitances are distributed over a large area; they appear, however, effectively in parallel with the SQUID and the input coil inductances, shunting the junctions. Resonators with high Q -values can be created.

The dc-SQUID loop itself forms a $\lambda/2$ resonating antenna, which has a quite low Q -value.^{196,197} However, the input coil and the SQUID form a microstrip-type resonator with much higher Q -values. If the loop size is increased, the resonances move closer to the Josephson frequencies. This is hazardous for proper operation of a dc SQUID, causing voltage plateaus in the IV characteristics.^{143,148,154,189} The problem becomes severe in multi-

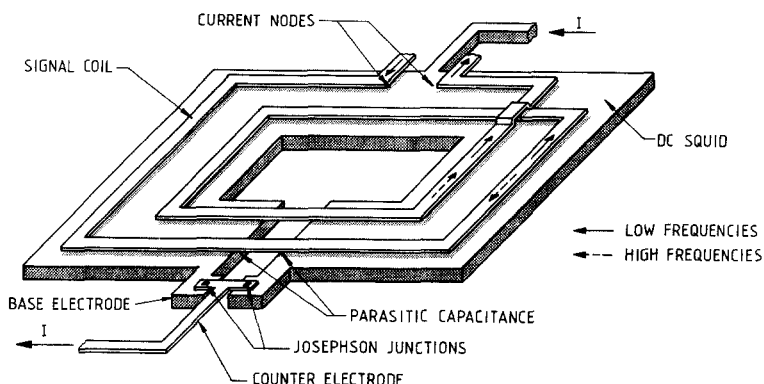


Fig. 23. Simplified structure of a planar dc SQUID together with a signal coil. The sites for the current nodes of the microstrip resonance and for the effective capacitive coupling are indicated. The directions of the current in the different signal-coil turns at frequencies lower and higher than the microstrip-line resonance frequency are shown.

loop structures,¹⁴² in which the transmission lines can be very long. In Ref. 154 the voltage plateaus are found to occur at approximately constant voltage intervals for three SQUIDs with different numbers of turns of the input coil. An increased number of turns sharpens the plateaus, indicating a higher Q -value as a result of the denser input coil. The sharpening of the voltage plateaus, as a function of the Q -value of the resonance, is very similar to the cavity-coupled Josephson devices.¹⁹⁸

Another resonance is created by the spiral transmission line, formed between the SQUID and the signal-coil microstrip line.^{148,189} The most probable standing wave has current nodes at the ends of the input coil, where the microstrip line leaves the SQUID ring and the wave impedance of the transmission line rises sharply (see Fig. 23). Figure 23 also illustrates the fact that, at low frequencies, the current in the input coil flows in the same direction, whereas at frequencies higher than the microstrip-line resonance a phase difference between turns is created because the wavelength of Josephson oscillations becomes smaller than the total length of the signal coil. The effective coupling between the input coil and the dc SQUID diminishes, being negligible at very high frequencies. Measurements of the dynamic input impedance reveal a reduction in the coupling at higher frequencies,¹⁹⁹ confirming the decoupling of the SQUID and the input coil. If the coil is long, i.e., there are many turns, the cutoff frequency is well below the Josephson frequency. The coupling at high frequencies becomes looser, which makes the SQUID more independent of its surroundings. On the other hand, the demand for lower parasitic capacitance favors a short signal coil, and thus the $\lambda/2$ resonance of the signal coil has a tendency to be near the operating frequency. A compromise is necessary.

The characteristics of the dc SQUID were found experimentally to depend markedly on the impedance connected across the input coil.^{146,200,201} The signal-coil circuit, including parasitic capacitances, determines the resonance frequency of the flux transformer oscillations. The Q -value is set by dissipations in the combined system of the SQUID and the signal coil. Low-frequency resonances in the signal coil do not manifest themselves in the dc SQUID characteristics as plateaus of voltage, because they are far below the operation frequency, and at high frequencies the coupling becomes smaller. Hence, their influence on the dc-SQUID dynamics has not always been realized. Thermal noise can undoubtedly activate the resonances in the signal coil as shown by computer simulations¹⁴⁸ and by experiments.¹⁴⁶ Especially in dc SQUIDs with high β_c , hysteresis creates a rich spectrum of frequencies, facilitating the activation of signal-coil oscillations. The interaction of the signal-coil resonances with the dc-SQUID dynamics is extremely difficult to study numerically, because the magnetic coupling varies with frequency as was discussed earlier.

In applications where the dc SQUID is used as an amplifier, an additional problem due to grounding may arise if the SQUID and the input circuit are in galvanic contact: the distributed capacitive coupling between the circuits may cause a capacitive feedback influence on the characteristics.¹⁵⁴ In most magnetometer applications the frequency is so low that this effect is not a severe problem, if the feedback is not sufficient to create parasitic oscillations.

4.2.2. Model for Practical dc SQUIDs

Reasonably realistic computer models have been constructed by several groups for studying the resonances caused by the parasitic capacitance over the junction area^{141,144,147} and by the input-coil resonances coupled to the dc SQUID.^{148,202}

Figure 24 shows the equivalent circuit of a dc SQUID coupled to an input coil. In the model the flux coupled to the SQUID is divided into the low-frequency signal φ_a , assumed to be constant in the simulations, and into the high-frequency part caused by oscillations in the signal coil. The input coil introduces a parasitic capacitance C_p in parallel with the SQUID inductance L ; the shunt resistor R_p is for damping the LC_p -resonances.¹⁴⁴ The input-coil inductance L_s is in parallel with a stray capacitance C_s . The L_sC_s resonance is damped by a resistor-capacitor shunt R_xC_x . The high-frequency current oscillations I_s in the input coil are coupled to the SQUID with a complex frequency-dependent mutual inductance $M(\omega) = \bar{k}(\omega)(L_s L)^{1/2}$, where $\bar{k}(\omega)$ is a complex frequency-dependent coupling constant. The signal-coil inductance L_{ext} can be incorporated into L_s .

When the above-mentioned effects are taken into account, Eq. (48) remains unchanged, while Eq. (49) becomes

$$\begin{aligned} \beta_{c,\text{eff}} \frac{d^2\varphi}{dt^{*2}} + (1+2\rho) \frac{d\varphi}{dt^*} + \cos \nu \sin \varphi + \frac{2}{\beta_L} (\varphi - \varphi_a) \\ = -2\zeta_L k(t^*) * i_s(t^*) + i_{n,\varphi}(t^*) \end{aligned} \quad (58)$$

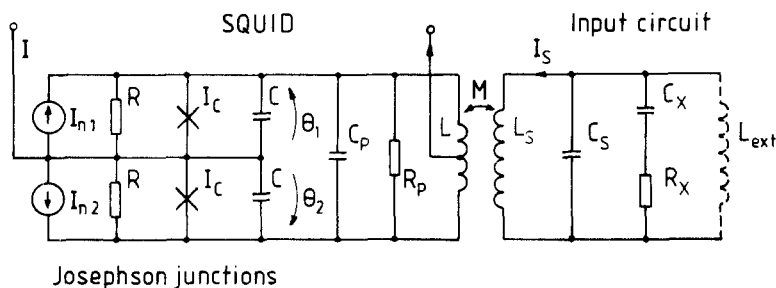


Fig. 24. Model of a dc SQUID with input coil.^{148,202} The parasitic capacitances C_p and C_s and the damping elements R_p , C_x , and R_x are included.

where $\beta_{c,\text{eff}} = (1 + 2C_p/C)\beta_c$ is the effective β_c arising from the extra capacitance, $\rho = R/R_p$ represents the increased damping in the system, $\langle i_{n,\phi}(t^*)i_{n,\phi}(t^* + \tau^*) \rangle = (1 + 2\rho)\Gamma\delta(\tau^*)$, $\zeta_L^2 = L_s/L$, and the oscillating current $i_s = I_s/2I_c$ in the input circuit is governed by a third-order differential equation.^{148,202} The frequency-dependent coupling in the differential equation (58) is given by the convolution integral $k(t^*) * i_s(t^*)$. In simulations a proper coupling can be achieved by an additional differential equation.²⁰²

A higher $\beta_{c,\text{eff}}$ increases the oscillations of the circulating current, while the influence of ρ is the opposite. The effect of the external current is to swing the potential trough of Fig. 13. When this swinging is in resonance with the motion of the mass point, the potential slope falls under the mass point, indicating high-amplitude oscillations in the circulating current.

4.2.3. Effect of Parasitic Capacitances

The most prominent new feature introduced by the signal coil is the increased parasitic capacitance C_p appearing across the junctions.^{141,144,202} Evidently, C_p is roughly proportional to the number of turns in the signal coil. The dynamics of the SQUID is affected if C_p becomes comparable to the junction capacitance C .^{148,202} When $C_p > C$, the dynamics is completely determined by the stray capacitance, because of noise.

As we discussed earlier, the resonances in the signal coil, although far below Josephson frequencies, are activated thermally. Figure 25 illustrates a simulation of a dc SQUID, coupled to a resonant circuit with different Q -values, using the model discussed previously. The $i\bar{v}$ characteristics are dramatically affected. The voltage distribution shows that, in addition to normal Josephson oscillations, low-frequency oscillations exist as well. Figure 26 presents the corresponding noise spectrum. The signal-coil resonance is about two orders of magnitude lower than the Josephson frequency; in addition, harmonics of the resonance frequency are seen in the spectrum. Damping of the signal coil enhances the performance of the dc SQUID significantly: the voltage distributions of Fig. 25 and the noise spectra of Fig. 26 indicate much smaller low-frequency interference for proper damping.

The lifetime of the resonant voltage state is assumed¹⁴⁸ to be proportional to the Q -value divided by the resonant frequency. If the lifetime of a resonant state is much shorter than that of a running state, $\tau_1 \ll \tau_0$, the low-frequency power spectral density $S_V(0)$ is directly proportional to the lifetime of the resonant state, i.e., $\tau_1 \propto Q/\omega_{\text{res}} \propto 1/R_x$.

A resistor-capacitor shunt in parallel with the input coil reduces the resonance noise without increasing thermal noise, as was proposed and verified with computer simulations in Ref. 148. Experiments¹⁴⁶ carried out with dc SQUIDs manufactured by IBM¹⁹⁵ agreed well with these predictions.

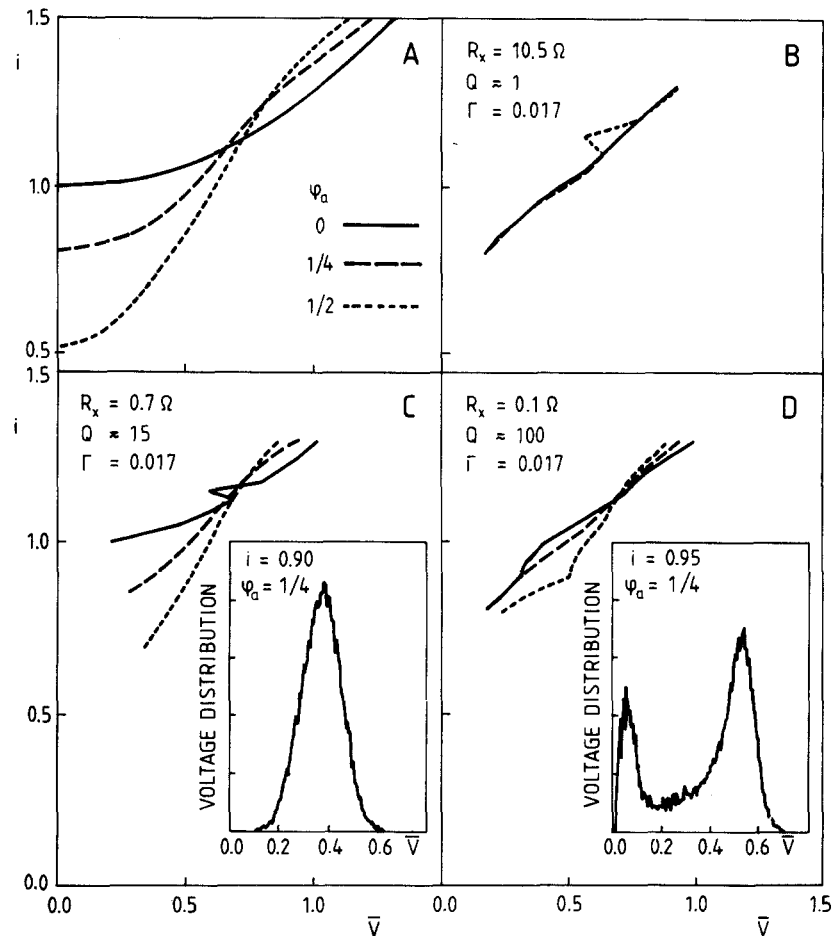


Fig. 25. Current-voltage characteristics of a SQUID with different values of the damping resistance R_x .¹⁴⁸ (a) Noiseless characteristics for a dc SQUID with $\beta = 1.0$, $\beta_c = 0.7$, and $\beta_{\text{eff}} = 0.91$. (b) Characteristics for $Q \approx 1$ at $\Gamma = 0.017$. (c) $Q \approx 15$; (d) $Q \approx 100$. The insets of (c) and (d) give the voltage distributions at the optimal points of operation ($\varphi_a = \pi/4$, $i = 0.9$, and $\varphi_a = \pi/4$, $i = 0.95$, respectively).

In Fig. 27, damping is seen to have a notable effect on the flux-to-voltage characteristics: without a shunt the best points of operation are at high bias currents with moderate flux-to-voltage transfer efficiency; proper damping of the signal-coil resonances enables the operation at low bias currents with improved gain. At fixed bias currents the flux noise is seen to scale roughly as $R_x^{-0.7}$. We can thus conclude that the shunt should be designed by minimizing the lifetime of the resonant oscillations. On the other hand,

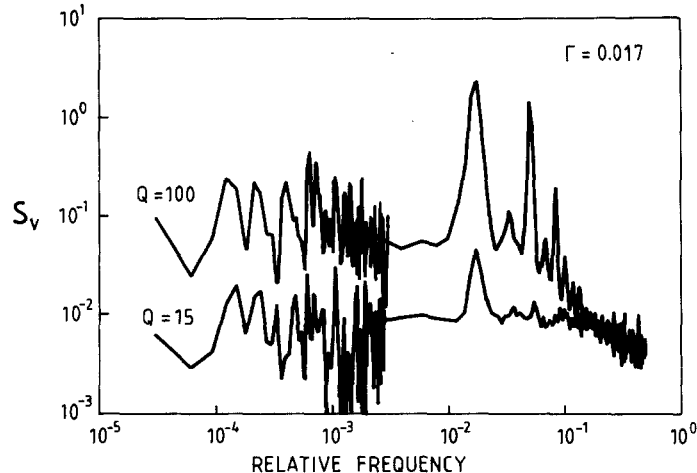


Fig. 26. Voltage noise power spectral density of the SQUIDs of Figs. 25c and 25d.¹⁴⁸ The Fourier transforms and the frequency scale are represented in the same way as in Fig. 21.

thermal noise caused by the damping resistor should extend neither to the signal nor to the Josephson frequencies. In addition, the shunt acts as an rf input filter.²⁰³

4.3. The State of the Art of dc SQUIDS

4.3.1. General

High coupling efficiency is best obtained with a large SQUID loop, whereas minimum energy sensitivity calls for a small device with a small junction capacitance. Studies of autonomous dc SQUIDS have shown that it is possible to increase the values of β_L and β_c without severe deterioration of performance. In practice, however, increasing the dimensions of the dc SQUID is not a fruitful approach. Best results have been obtained with low- β_c junctions and with damping of the signal-coil resonances, or by moderate values for all the SQUID dimensions that prevent the different resonances from affecting the dynamics. In this section, the most important dc-SQUID structures that include a flux-coupling circuit and that are used in low-frequency measurements are reviewed. Our aim is to point out how the different dc SQUIDS are affected by parasitic elements and how their performance can be improved. The analysis shows that the energy sensitivity obtained with all the different structures is proportional to $(LC)^{1/2}$.

4.3.2. Square-Washer dc SQUID

The most widely used thin-film dc SQUID design was suggested and fabricated by Jaycox and Ketchen;^{137,140} their SQUID loop is a square

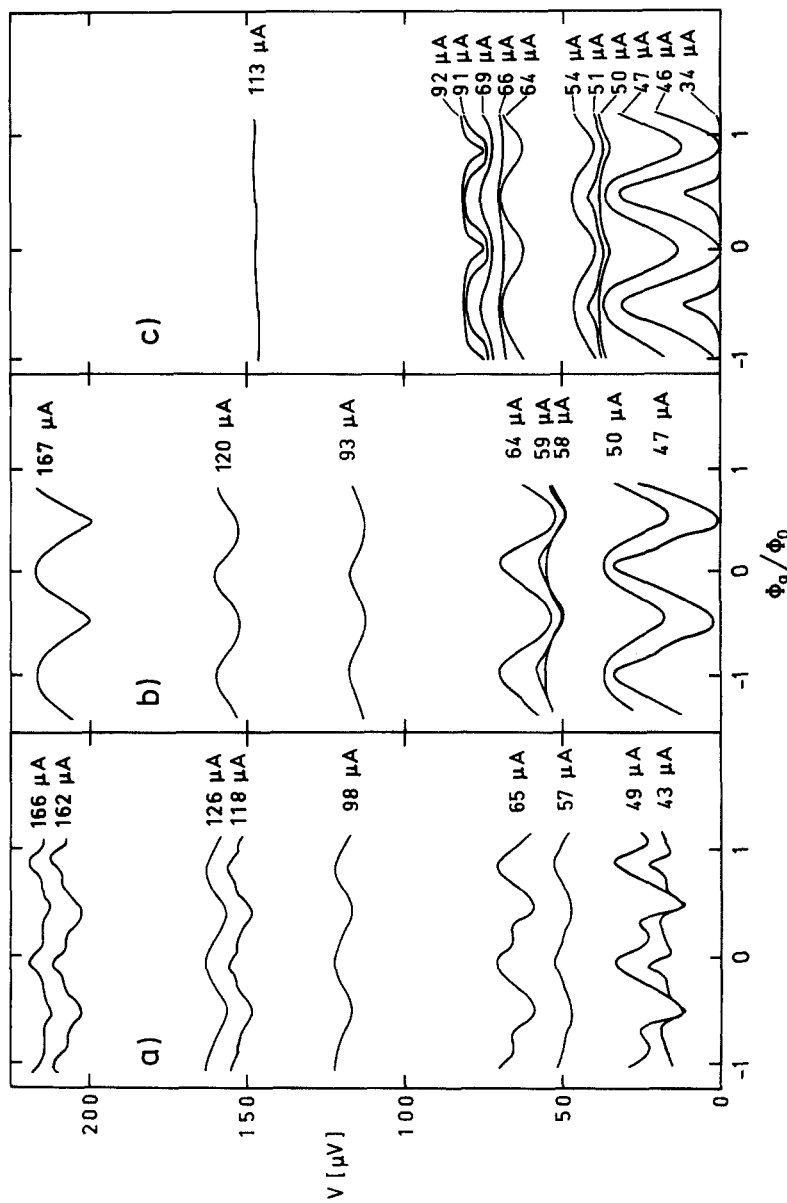


Fig. 27. Voltage-flux characteristics of an IBM dc SQUID connected to a pickup coil as a function of the bias current.¹⁴⁶ (a) no $R_x C_x$ shunt, (b) a shunt of $R_x = 3.3 \Omega$ and $C_x = 22 \text{ nF}$ and $C_x = 0.68 \text{ nF}$. (c) $R_x = 14.7 \Omega$ and $C_x = 0.68 \text{ nF}$.

washer of Nb containing a slit, as depicted in Fig. 23. Window-type Josephson junctions were used, and the input coil was deposited over the washer as a spiral Nb film. This structure provides a good coupling and a small SQUID inductance. However, the construction suffers from the parasitic resonances and interferences discussed previously. Plain square-washer SQUIDs have been used mostly in experimental work for studying the dynamics and the noise in SQUIDs and junctions, because of its simple structure. For magnetometer use, the energy resolution of the coupled dc SQUID has remained modest. This SQUID structure has been modified and developed by several groups in order to ensure better coupling or to get rid of the effects of parasitic elements: junctions have been shunted capacitively, resistively or inductively, a multiloop structure and matching transformers have been used, and SQUID parameters, including different parasitic elements, have been optimized.

4.3.3. Capacitively Shunted dc SQUID

Capacitive shunting of Josephson junctions has been suggested by Paik *et al.*²⁰⁴ In their scheme, the loop inductance is divided into two parts: a small loop of inductance L on the junction side and a large loop of inductance L_s on the signal-coil side. High-frequency Josephson oscillations see only the small loop, and the effective size of the SQUID loop is small. For low-frequency fields, in contrast, the effective inductance is $L_T = L + L_s$; the high inductance facilitates good coupling. In addition, the parameters can be controlled more accurately: The parasitic capacitance over the junctions is in parallel with a larger shunting capacitance and thus its effect is negligible. The double-loop dc SQUID allows reduction of β_L and β_c without sacrificing excellent coupling to the signal coil.

The behavior of the capacitively shunted dc SQUID has been analyzed in detail by Tesche.¹⁷⁰ Its characteristics are double-valued and hysteretic, owing to the frequency-dependent inductance of the dc-SQUID loop. Thermally activated switching between the multiple solutions creates a lot of excess noise especially at low values of bias current, where the flux-to-voltage transfer function is maximal. The characteristics are distorted by loop resonances, and the SQUID is noisy. At higher bias currents, where the characteristics are smoother, the noise is mainly thermal; the flux-to-voltage transfer function is, however, much smaller than at low bias currents.

Tesche¹⁷⁰ describes the dynamics of the capacitively shunted dc SQUID with a simple model. The critical current I_c is the same as for a conventional SQUID with a loop inductance $L_T = L_s + L$ and with the same applied flux Φ_a . The modulation depth $\Delta I_c \approx \Phi_0 / L_T$ is thus reduced far below that of a conventional dc SQUID with inductance L . Because of the double-loop structure, the average voltage across the SQUID is the same as for a

conventional dc SQUID. The effective flux Φ_e is determined by L_s . For $I \geq I_c$, $\Phi_e > \Phi_a$.

Because of hysteresis, the optimization of the double-loop SQUID must be carried out only for bias currents $I \geq I_c$. In this region, the noise rounding of the SQUID characteristics is negligible, and the forward transfer function can be approximated by the noise-free double-loop value $\partial \bar{V} / \partial \Phi_a = (\partial V / \partial I_c)(\partial I_c / \partial \Phi_a) \approx (R/2)(2\Delta I_c / \Phi_0) \approx R/L_T$. The transfer function is thus determined by the total loop inductance. For bias levels well above the critical current of the SQUID, $R_{dyn} \approx R/2$; we thus get from Eq. (55) a flux resolution $S_\Phi \approx 4k_B TL_T^2 / R$ and an energy resolution $\varepsilon \approx 2k_B TL_T / R$.

The capacitively shunted dc SQUID is operated in the bias current regime $I \gg I_c$ with relatively low values of transfer function but with very low excess noise. The energy resolution is found to be worse than for the autonomous dc SQUID at smaller bias currents, but much better than normally measured for coupled planar dc SQUIDs. Furthermore, the above analysis applies only to junctions with $\beta_c \ll 1$, and the influence of resonances in the flux-coupling circuit on the SQUID dynamics is neglected.

Double-loop dc SQUIDs have been produced at IBM.¹⁹⁵ The flux sensitivity in a practical magnetometer setup was $\leq 10^{-5} \Phi_0/\text{Hz}^{1/2}$, and the $1/f$ noise was very low. After the double-loop resonances were damped,¹⁴⁶ the flux sensitivity was improved to $\leq 4 \cdot 10^{-6} \Phi_0/\text{Hz}^{1/2}$. Characteristics of the IBM dc SQUID are shown in Fig. 27.

4.3.4. Resistively Shunted dc SQUID

Enpuku *et al.*^{144,205-207} have investigated thoroughly the effect of the damping resistance R_p , shown in Fig. 24. The main idea of their studies is to increase the SQUID loop inductance in order to achieve better coupling to the flux transformer. The increased inductance enhances the current oscillations, and the effect of the internal and external resonances becomes stronger. Equation (58) is the basis for studying the effect of R_p . The parasitic capacitance affects the parameter $\beta_{c,\text{eff}}$, and the damping resistor has its influence through the parameter ρ . The higher the value of $\rho = R/R_p$, the better is the damping; on the other hand, the parasitic capacitance C_p effectively reduces the damping.

Studies by Enpuku *et al.*¹⁴⁴ based on an analytical expression and on computer simulations, show that the flux-to-voltage characteristics of the dc SQUID become almost independent of β_L when $\rho > 1$; $\partial \bar{V} / \partial \Phi_a$ does not deteriorate as in a conventional dc SQUID. The effect of the junction capacitance is negligible when $\beta_c \leq 0.4$. In further numerical simulations,²⁰⁵ the energy resolution of the resistively damped dc SQUID was investigated, concentrating on the overdamped junction ($\beta_c \approx 0$). It was found that the damping significantly improves the energy resolution of the SQUID for

large β_L , although the best performance was still obtained for $\beta_L = \pi$. The energy resolution for $\beta_L = 4\pi$ was only two times and for $\beta_L = 10\pi$ four times as large as for $\beta_L = \pi$. Furthermore, in a large- β_L dc SQUID, a good energy resolution was found for a wide range of points of operation and for bias currents above the critical current.

If the resistive shunting is assumed to wipe out the excess noise generated by the LC_p resonance of the SQUID, the damping resistor must be set to $R_p \sim (L/C_p)^{1/2}$. If L is increased, R_p must also be increased. The damping resistor creates an extra flux noise $S_\Phi(0) \approx 4k_B TL^2/R_p$ in the SQUID loop, adding $\Delta\varepsilon \approx 2k_B TL/R_p \approx 2k_B T(LC_p)^{1/2}$ to ε . However, if optimization of the whole magnetometer configuration is performed, following the scheme discussed in Sec. 4.1.6 and including the effect of R_p on the flux noise and on $\partial\bar{V}/\partial\Phi_a$, the contribution $\Delta\varepsilon_{ext}$ of R_p is small.²⁰² If $C_p > C$, the use of R_p for damping the LC_p resonance is suitable and gives possibilities for coupling submicron-junction SQUIDs to the signal coil. The result that a ten times larger value of β_L gives only four times higher noise energy can be understood on the basis of the square-root law $\varepsilon \propto (LC)^{1/2}$.

4.3.5. Inductively Shunted dc SQUID

A structure in some ways similar to the capacitively shunted dc SQUID is obtained by dividing the SQUID loop inductively into two parts.^{139,145,208} The large loop couples the flux while the smaller loop forms the dc SQUID. This structure has not, however, been analyzed thoroughly in the literature, but it does not differ much from the former two cases.

Let $\Phi_s = L_s I_s$ be the flux coupled to the bigger loop of inductance L_s . The current circulating in the smaller loop is approximately I_s at low frequencies; thus the flux in the smaller loop is $\Phi_i \approx LI_s = (L/L_s)\Phi_s$. The flux noise of the smaller loop, from Eq. (55), is $\Phi_{i,n}^2 \approx 13.4k_B TL^2/R$. Consequently, the energy resolution of the SQUID is

$$\varepsilon = \frac{\Phi_{s,n}^2}{2L_s} \approx \frac{1}{2L_s} \left(\frac{L_s}{L} \right)^2 \Phi_{i,n}^2 \approx 6.7k_B TL_s / R \quad (59)$$

The advantage of this structure is that the parasitic capacitance across the junctions does not cause LC_p resonances at low frequencies. On the contrary, the large loop size brings the transmission-line resonances down to Josephson frequencies.

A comparison of the capacitively, resistively, and inductively shunted dc SQUIDs reveals that the devices are limited by the loop inductance. This is the cost for coupling the input coil to the dc SQUID. On the basis of these results we conclude that the basic features determining the sensitivity of dc SQUIDs are the effective inductance of the larger loop connected to the junctions and the effective capacitance due to the junctions and parasitic

elements. Whatever efforts are made to obtain better energy resolution, one is always ultimately limited by $(LC)^{1/2}$.

4.3.6. Multiloop dc SQUID

Carelli and Foglietti^{142,209,210} have constructed multiloop dc SQUIDs, which enable good coupling with a fairly low loop inductance. The idea is similar to that of the fractional-turn SQUID, originally reported by Zimmerman *et al.*¹⁸³ for rf SQUIDs. Because of its large size, the multiloop structure suffers from $\lambda/4$ transmission-line resonances that are seen as voltage plateaus in the $\bar{V}\Phi_a$ characteristics. The multiloop structure is suitable for rf SQUIDs because the pump frequency is far below the transmission-line resonances, whereas in dc SQUIDs the Josephson frequencies are near the $\lambda/4$ resonance of the SQUID loop. On the other hand, owing to the long signal coil, coupling of the SQUID and the signal coil is strongly reduced at high frequencies. Thus the SQUID is not disturbed by the signal coil resonances. The result is relatively good energy resolution with good coupling, but there are problems in obtaining smooth characteristics and thus trouble with excess noise due to hysteresis.

4.3.7. dc SQUID with a Matching Transformer

An efficient scheme to couple the low-inductance dc SQUID to a signal source was developed by Muyllefelder *et al.*^{143,211} They constructed a low-noise dc SQUID with 16-pH inductance, and coupled it to a 1- μ H signal coil with a matching transformer. The SQUID performed as expected at low frequencies. The characteristics were smooth enough for normal flux-modulated operation. However, the $\bar{V}\Phi_a$ characteristics were clearly affected by resonances which arose, according to the authors, from striplines.

The matching-transformer solution provides excellent possibilities for design:^{143,148,189} 1) The number of turns over the SQUID can be small; as a result, parasitic capacitances are small and transmission-line resonances are easier to control. 2) Good coupling between the high-impedance signal coil (1–2 μ H) and the low-impedance SQUID loop (10–100 pH) can be achieved. 3) The effect of parasitic resonances in the transformers may be controlled by the external circuit.

4.3.8. Optimized dc SQUID

Recently, the design and fabrication of a dc SQUID, with the previously discussed points (see also Ref. 148) taken into account, was published.¹⁸⁹ The starting point of the design was that the energy resolution is proportional to $(LC)^{1/2}$. The fabrication technology, however, dictated the lower bounds for stray inductances and junction stray capacitances; the lowest obtainable noise level was determined by these constraints. For an optimized SQUID, the loop inductance is of the same order of magnitude as the SQUID stray

inductance, and the parasitic capacitance appearing across the SQUID loop should be prevented from exceeding the junction capacitance.

To couple flux to the small-inductance SQUID, without introducing excessive parasitic capacitance via a large number of input-coil turns, an intermediate matching transformer was used in this design. The optimization of the geometrical dimensions was carried out with a model where the effects of the input circuits, including parasitic elements, were taken into account; fabrication technology limitations were used as boundary conditions. A second major point in the design was the control of resonances introduced by the signal coil: they should be properly damped and kept from interfering with the Josephson oscillations. Furthermore, the structure was designed to be used with planar gradiometers in multichannel applications, as discussed in our companion paper.¹⁵

In the resulting design, moderate values of $\beta_c = 0.3$ and $\beta_L = \pi$ were used to ensure stable dynamics. The $\lambda/2$ resonance of the SQUID loop was adjusted to be above the Josephson frequencies at the normal operating points, and the transmission-line resonances corresponding to the total length of the input coil were set below the Josephson frequency and damped by terminating the line with a resistor, matched to the microstrip-line impedance. The predicted energy resolution $\epsilon_{int} \approx 1.2 \times 10^{-31}$ J/Hz, with reliable and smooth operation and a low $1/f$ noise, was obtained within a factor of two, indicating the success of the design. The disadvantage of the structure is that its realization requires 11 mask layers, complicating the fabrication.

5. FABRICATION OF TUNNEL-JUNCTION SQUIDS: LIMITATIONS TO THE DESIGN

5.1. Materials

The majority of SQUIDs have been fabricated from pure Nb and from Pb alloys containing about 10% Au, In, or both; pure lead is not used because of its instability in thermal cycling. A conventional structure has both Nb and Pb layers. The base electrode is made from Nb, the tunnel barrier is oxidized on the Nb surface, and the top electrode is made of a Pb alloy. The electrodes are usually separated by a layer of silicon oxide except at a window that defines the junction area.

This two-metal structure has been popular because it has better properties than all-lead-alloy structures. The hardness and high tensile strength of niobium and the stability of the pentoxide Nb_2O_5 are the main advantages. On the other hand, all-niobium structures, with niobium oxide barriers, have posed difficulties in fabrication and in obtaining good tunneling characteristics; for low-leakage junctions a thin Cu or Au layer on the top of the oxide is necessary.²¹²⁻²¹⁶ The fabrication and properties of the Nb-Pb

alloy structures have been discussed extensively in the literature; see, for example, the review by Broom *et al.*²¹²

Recently, all-refractory-material junctions have been introduced, utilizing all-Nb or NbN electrodes separated by “artificial” tunnel barriers such as Al₂O₃, MgO, or amorphous Si. Especially, Al₂O₃ and MgO are superior to conventional materials; their stability is better, the critical current uniformity and reproducibility are good, and the subgap leakage current is very small. In addition, with NbN electrodes the maximum operating temperature is higher. For reviews, see, for example, the papers by Raider²¹³ and Braginski.²¹⁷

The recent discovery of superconducting ceramic compounds¹⁴ and their development, resulting in critical temperatures of over 90 K²¹⁸, over 110 K²¹⁹ and over 125 K,^{220,221} have raised hopes for high-temperature SQUIDs. Most studies have been performed with lanthanum-barium-copper-oxide, yttrium-barium-copper-oxide, bismuth-strontium-calcium-copper-oxide, and thallium-barium-calcium-copper-oxide compounds. The unfavorable mechanical, chemical, and crystalline properties of the ceramic superconductors complicate the development of high-quality films and wires, as will be discussed in the next section.

The Josephson effect has been observed in these high- T_c materials.²²²⁻²²⁶ In most of the studies, microbridges or crack junctions have been used. The microbridges, however, have been larger than the estimated coherence length, suggesting that the junctions form between grain boundaries.

In addition to superconducting films and insulators, resistive films are also needed in the SQUIDs. Since the required square resistance is often on the order of a few ohms, pure metals are not practical because of the required thinness of the film, unless the resistor can be the lowermost layer, whereby step coverage problems can be avoided. Gold, chromium, copper, tantalum, palladium, and molybdenum, for example, have been used as resistor materials; the films are only some tens of nanometers thick. For thicker films, various alloys with higher resistivity, such as AuTi^{227,228} and AuIn,²²⁹ have been used; often, the different elements are deposited alternately to form sandwich structures.

5.2. Film Deposition and Patterning

Sputtering and evaporation are the most common methods in depositing thin films. For example, in depositing Nb, the high melting temperature of this metal, the requirement of heating the substrate to avoid strains in the films, and the easy gettering of impurities make evaporation difficult, favoring sputtering. For low-defect-density dielectrics, chemical vapor deposition has also been used.²³⁰

The films are patterned by etching through lithographically defined resist masks. Chemical wet etching has largely been replaced by dry methods like plasma^{231,232} and ion-beam etching.²³³ Another possibility is to apply a lift-off technique, where a photoresist layer is first coated over the substrate and patterned. Following film deposition, the resist is removed with a solvent, thereby lifting off those parts of the film that were on top of the resist. Etching that might deteriorate the underlying structures is not needed but a good control over the resist profile is required.

The minimum linewidths with the above-mentioned methods, using optical photolithography, are typically a few micrometers. For submicron resolution, electron-beam lithography with direct writing on the substrate must be used.

The use of several photolithographic mask layers with fine details requires accurate alignment. Because of the overhead in the dimensions, necessary for alignment, very small window junctions are difficult to fabricate in a well-controlled manner. To avoid problems, self-alignment techniques for junction formation have been developed.^{230,234-240} In these "full-wafer sandwich" methods, the junction barrier is formed on the whole wafer, to be patterned afterwards. With this technique it is also possible to avoid the cleaning step before junction barrier formation and even to reduce the number of masks.

In window-type junctions capacitances are relatively large. For example, in Nb-Nb oxide-Pb rectangular tunnel junctions an experimentally determined relation is²⁴¹ $1/C_s = (8.4 \pm 1.7) - (0.45 \pm 0.15) \ln j_c$, where C_s is the specific capacitance in $\text{pF}/\mu\text{m}^2$, and j_c the critical current density in $\mu\text{A}/\mu\text{m}^2$. Thus, for $j_c = 10 \mu\text{A}/\mu\text{m}^2$, we obtain $C_s = 0.14 \text{ pF}/\mu\text{m}^2$. This is due to the high dielectric constant of Nb_2O_5 ($\epsilon_r = 30-100$)²⁴² and the thinness of the barrier. The specific capacitance of Al_2O_3 and MgO junctions is smaller because of the smaller ϵ_r ; for example, aluminium oxide junctions with $j_c \sim 10 \mu\text{A}/\mu\text{m}^2$ have $0.06 \text{ pF}/\mu\text{m}^2$.²³⁴ Edge junctions enable the reduction of the junction area to $1-2 \mu\text{m}^2$.²⁴³⁻²⁴⁵ In these structures, the edge of the film is etched to be oblique, the top of the film is insulated, and the actual junction is formed by oxidizing the edge. Another method is to form the junction between two vertical side-by-side edges of the film.²⁴⁶ The characteristics of junctions formed by the latter method resemble those of point-contact junctions, with an area as low as $0.2 \mu\text{m}^2$; no external shunting is necessary.

The lithographic processes require utmost care. For example, pinhole defects in the insulators, due to inadequate cleanliness, cause short circuits. Two insulator layers with different masks eliminate pinholes, but this costs an extra vacuum deposition and lithography step. Long and narrow conductors, which are necessary in signal-coupling coils, are difficult to fabricate; small dust particles or photoresist residuals can easily cause discontinuities

in the films. In multilayer structures, conductors must cross over film edges and steps; to ensure proper step coverage, each successively deposited layer must usually be thicker than the ones below. Furthermore, possible leftovers from patterning of previous films may also cause discontinuities. For example, during SiO film deposition, material is backscattered on the edges of the photoresist stencils used in lift-off; the resulting burr on the edge is partly attached to the substrate and thus it may not be completely removed with the resist. The material on the edges must be etched away before lift-off; however, at the same time the step coverage of cross-overs is weakened.

To avoid step-coverage problems in multilevel structures, which severely restrict the minimum feasible feature sizes, including the film thickness, special planarization techniques have been developed. A undercut lift-off planarization process²⁴⁷ utilizes a multilayer photoresist, both for etching and for lift-off, to obtain a groove-free planar structure with no residues on the edges. In a second method, a polystyrene layer is spun and baked planar on the structure to be flattened and then etched back.²⁴⁸ The etch rates of the polystyrene layer and of the topmost layer underneath it is then adjusted to be the same, resulting in excellent planarity of the final structure.

Fabrication of thin films of the new ceramic superconductor materials has introduced many new problems. For example, during the deposition the film reacts with many substrates; SrTiO₃ and yttria-stabilized ZrO₂ have proven to be among the best substrate materials. Thin films have been sputtered, co-sputtered, ion-beam sputtered, and electron-gun evaporated for layered structures, co-evaporated, laser-beam deposited, or grown by molecular beam epitaxy. The result is typically an amorphous film, which must be annealed in an oxygen atmosphere to form the superconducting crystalline structure; even then, the resulting film is usually polycrystalline. Grain boundaries, which can act as Josephson junctions, are easily formed; they may severely limit the critical current density, but they offer possibilities for producing Josephson devices in a natural way.²⁴⁹ Furthermore, the patterning of the film may substantially affect its properties and lower the critical temperature. So far, the most promising methods seem to be direct laser patterning and oxygen implantation, whereby the material outside desired conductor regions is made insulating. The high temperatures needed during film deposition or annealing, and the morphology and reactivity of the films even with water introduce severe problems in tunnel-junction fabrication from these materials.

5.3. Formation of the Junction Barrier

The conventional tunnel barrier is made by oxidizing the Nb base electrode with either rf²⁵⁰ or dc plasma.^{251,252} For better process control, a

mixture of 95% of Ar and 5% of O₂ is typically used as the working gas. The rf plasma method is preferred because of its better controllability.

Oxidation by an argon-oxygen ion beam is an interesting alternative in forming the oxide tunnel barrier.^{244,253-256} The advantage is that the energy of the ions and the ion flux and thus the resulting oxide thickness can be accurately controlled. As in the rf plasma process, a steady state between oxidation and sputtering by argon can be achieved. However, anisotropy and lack of uniformity of the ion beam can reduce the homogeneity of the junction.

The critical current in tunnel junctions depends exponentially on the barrier thickness. For Nb-Nb oxide-Pb junctions, experimental dependences $e^{-3.1d}$ for thermally oxidized barriers²⁵⁷ and $e^{-7.8d}$ for rf-plasma-oxidized barriers²¹² have been reported, where d is the oxide thickness in nm. In the latter case, a junction with a critical current density of 10 $\mu\text{A}/\mu\text{m}^2$ implies an oxide barrier thickness of 1.3 nm. The fabrication of the barrier is critical; even small parameter variations may cause large deviations in junction characteristics, leading easily to a large spread of the critical current and to a substantial run-to-run variability.

The Nb-oxide tunnel barrier has a complex structure, containing suboxides NbO_x in addition to the bulk Nb₂O₅; these can increase leakage and reduce the critical current. It has been shown that during the pre-cleaning of the Nb surface before oxidation with an Ar plasma discharge or an Ar ion beam, remanent gases in the vacuum system and from the photoresist form a niobium oxycarbide (NbO_xC_y) transition layer between Nb and Nb₂O₅. Because of this layer, the tunnel barrier is better defined and the formation of oxides other than Nb₂O₅ is reduced, yielding a lower subgap leakage current. In addition, the diffusion of oxygen into Nb, which lowers the critical temperature, is decreased.²⁵⁸⁻²⁶¹ A small amount of carbon from the residual gases or from the methane deliberately let in is therefore essential for the formation of high-quality junctions. On the other hand, large concentrations of impurities would deteriorate the junction quality. Also the use of high ion energies, necessary for good cleaning, damages the Nb surface and heats it, leading to less well-controlled oxidation.

As discussed above, oxide junctions have several inherent difficulties. Therefore, they are being replaced by all-refractory junctions with aluminium or magnesium oxide barriers. For example, the V_m parameter, defined as the resistance at 2 mV times the critical current, is almost invariably larger than 30 mV, compared to 20 mV for oxide-barrier junctions; values even as large as 70 mV have been reported.²⁶² Furthermore, the critical current spread in junctions fabricated with self-aligned processes is small; in experiments with 100 junctions connected in series, the maximum deviations of the critical current from the mean were found to be only a few percent.^{236,263}

The Nb base electrode is usually covered with a thin (<10 nm) layer of Al.²⁶⁴ Alternatively, a NbN base electrode and/or a Mg layer may be used. The surface is then oxidized thermally or with an ion beam. This results in a more uniform oxide than the randomly-oriented polycrystalline thermal oxide.²⁶⁵ The oxide does not, however, extend through the Al or Mg layer, leaving a metallic interface between the base electrode and the tunnel barrier. The oxide may then be covered with a thin Al or Mg layer before the deposition of the counter electrode; after the completion of the sandwich structure over the whole wafer area, the junction area is defined by anodization or etching. For details, see for example Ref. 234.

The thickness of the metal layer deposited before oxidation affects the junction quality. For Al layers thinner than 6 nm, it was found that a smaller V_m results, probably because of nonuniform thickness. In addition, the base electrode must be cooled adequately before the deposition of Al to prevent leakage currents due to Al diffused into Nb.²⁶³ Unoxidized Mg has a greater tendency to diffuse into the base electrode than Al; MgO does, however, provide a better substrate for epitaxial growth of the NbN counter electrode than Al₂O₃ does.²⁶⁵ The lattice constant of the MgO barrier can also be adjusted to match that of the NbN by adding Ca.²⁶⁶ Films of Al₂O₃ and MgO have also been electron-beam evaporated and sputtered on the base electrode.²⁶⁷⁻²⁷¹

In addition to aluminium and magnesium oxides, several other barrier materials, such as tantalum oxide²³⁶ and silicon,^{272,273} have been tested. TaO_x seems more stable during annealing than Al₂O₃ and MgO. Amorphous silicon barriers with low leakage are obtained only with hydrogenation; although the results are comparable to those of the other artificial barriers, higher 1/f noise seems to result,²⁷⁴ whereas the low-frequency noise of Al₂O₃ junctions is small, at 1 Hz only of the order of 1 ppm/Hz^{1/2} of the critical current.²⁷⁵

5.4. Discussion

Proper optimization of SQUIDs is, of course, only possible if the critical parameters can be accurately controlled. Fabrication technology poses a number of constraints, including minimum linewidths and conductor separations, required film thicknesses for proper step coverage, feasible critical current densities and specific junction capacitances, and sheet resistances of resistor films. All these technology-dependent constraints limit the range of possible junction capacitances, parasitic capacitances, and inductances for the SQUID.

The optimization of the SQUIDs usually leads to very small dimensions. On the other hand, in integrated magnetometers the area of the flux-collecting coil and the base length of the gradiometers should be made

large. Thus only a few devices can be fabricated on a single wafer, and the yield of the fabrication process becomes critical.

6. SQUIDS MADE OF HIGH-TEMPERATURE SUPERCONDUCTORS

6.1. General

The Josephson effect and quantum interference in the high- T_c superconducting materials have been reported by several laboratories.²⁷⁶⁻²⁸⁰ These materials have some new properties that may be relevant to SQUID design: 1) extremely short coherence lengths, with several consequences: a) glassy nature of superconductivity leads to slowly decaying magnetization at low fields and a spin-glass-like state at higher field, b) low pinning forces allow flux creep, which creates a lot of low-frequency noise, particularly in thin-film devices, c) rough surface structures prevent construction of tunnel junctions; 2) anisotropy and twin boundaries: the conductivity is highest in the plane perpendicular to the c axis of the perovskite crystal structure; this may cause difficulties with monocrystalline or epitaxial structures, but new possibilities for devices are created; 3) granularity of superconductivity in bulk samples and in polycrystalline thin films; phase-locked Josephson junctions between the grains lead to fluctuations of current paths and to formation of Josephson vortices with non-reversible characteristics of microwave absorption; 4) lower critical current densities than in conventional superconducting materials, mostly because of the granular structure and the flux creep; 5) low density of normal current carriers, i.e., a reduced quasiparticle current compared to metallic superconductors; 6) difficulties in machining the bulk samples; and 7) sensitivity to moisture and air.

6.2. Examples of Existing High- T_c SQUIDS

Zimmerman *et al.*²⁷⁹ have reported a crack-junction rf SQUID made of YBaCuO. The device is a pellet with a 0.95-mm hole; a partial sawcut and a crack were made to break the loop. The Josephson effect was observed up to 81 K; at 75 K the equivalent flux-noise level was $4.5 \times 10^{-4} \Phi_0/\text{Hz}^{1/2}$. The geometric inductance of the SQUID was about 0.25 nH. The SQUID was driven with 27-MHz pump frequency; thus, Eq. (37) gives much better sensitivity at 75 K than was the case in this experiment. Possible explanations are flux motion in the material and the increased SQUID inductance due to modified current paths in the material, causing reduced $\partial \hat{V}_T / \partial \Phi_a$ according to Eq. (34). Repeated cycling was found to reduce $\partial \hat{V}_T / \partial \Phi_a$ further, indicating instabilities in the material.

Koch *et al.*²⁷⁶ made a polycrystalline YBaCuO thin-film dc SQUID using ion implantation for patterning. The transition temperature of the complete device was above 85 K. The grain size was optimized to give a high critical current density and to be sufficiently small for patterning. Because the critical current density depends on Josephson coupling between the grains, weak link behavior is observed in microbridges far larger than the superconducting coherence length of the material. The junctions were 17- μm wide weak links. The inductance of the SQUID loop was estimated to be 80 pH. SQUID behavior was observed up to about 74 K; however, the modulation depth decreased when this temperature was approached. The measured energy resolution was $\varepsilon \approx 3 \cdot 10^{-30} \text{ J/Hz}$ at 1 kHz and 40 K, and $\varepsilon \approx 2 \cdot 10^{-25} \text{ J/Hz}$ at 1 Hz and 77 K, increasing as $1/f$ at low frequencies (see Refs. 281–283). The lowest noise level of high- T_c dc SQUIDs to date was reported by Sandstrom *et al.*²⁸⁴; their SQUID was fabricated with photolithography on a single layer of low-current-density ($\sim 10^4 \text{ A/cm}^2$) film. The measured flux noise level was $3 \cdot 10^{-4} \Phi_0/\text{Hz}^{1/2}$ at 20 Hz and 77 K. The noise was completely $1/f$ dominated.

Chaudhari *et al.*²⁴⁹ have directly measured electrical and magnetic properties of grains and single boundaries between them, using large-grained polycrystalline films on a SrTiO₃ substrate. They measured the current-voltage characteristics for the grain boundary and found a step-like onset of normal resistance, which was frequently hysteretic. The characteristics were reminiscent of tunneling through a junction with small β_c . The grain boundaries were found to consist of regions of good and poor Josephson coupling. Using laser-patterning, a dc SQUID with constrictions was constructed. It was suggested that grain boundaries in the constrictions formed the junctions.

dc SQUIDs patterned on epitaxial film of YBaCuO have been reported in Ref. 282. A complete loop without weak links did not show any SQUID response at any temperature although the films contained many twins. Twins are not Josephson elements in the same sense as grain boundaries; the phase difference across the twin boundary is not sufficient to limit the critical current of the loop. SQUID behavior appeared after damaging the loop by weakening an already existing twin or other structural defect in the film. The SQUID worked at 74 K; however, the noise level could not be measured because of the high contact resistance.

The possibility to improve the microwave SQUID in rf attenuation measurements by taking advantage of the low density of normal current carriers and the high normal resistance of the YBaCuO Josephson junction at 4.2 K has been demonstrated.¹¹³ A point-contact junction was adjusted in a waveguide. Two important improvements were achieved: 1) the high characteristic frequency $\omega_c = R/L$ (see Sec. 3.4) makes a sensitivity of

$4 \cdot 10^{-6} \Phi_0/\text{Hz}^{1/2}$ possible with $\omega_p = 2\pi \times 10 \text{ GHz}$, and 2) the small quasiparticle current in the SQUID loop improves the accuracy of rf attenuation measurements by reducing nonlinear shielding effects. The use of YBaCuO in some applications at 4.2 K can be of great importance.

6.3. Noise in High- T_c SQUIDs

All the high- T_c SQUIDs studied so far have had much higher noise levels than expected on the basis of thermal noise alone (see Refs. 282, 285 and 286). Figure 28a shows the increase of flux noise as a function of temperature in rf SQUIDs with either $L = 0.25 \text{ nH}$ or 1.0 nH , using $f_p = 30 \text{ MHz}$ and 200 MHz ; the curves are derived from Eq. (37) by replacing α_{exp} by α given in Eq. (35). Since in practice α is higher than Eq. (35) predicts, the plotted curves are lower limits for the flux noise. When the thermal energy approaches ΔE of Eq. (33), quantum interference will disappear; increased noise results. The upper limit for the inductance is plotted in the inset of Fig. 28a. Because the optimal inductance of a SQUID at 77 K is below 0.1 nH , practical rf SQUIDs with tightly coupled input coils are difficult to construct from the ceramic materials. In Fig. 28b, the temperature dependence of the flux noise in the dc SQUID is depicted. The curves are constructed on the basis of simulations discussed in Sec. 4.1.5. $\langle \Phi_n^2 \rangle^{1/2}$ is seen to deviate clearly from the \sqrt{T} -dependence at higher temperatures; in this respect, dc and rf SQUIDs are similar.

It is interesting to compare the curves of Fig. 28 with measured behavior. While the noise level of the rf SQUID of Zimmerman *et al.*²⁷⁹ can be accounted for by a somewhat higher inductance than calculated from the geometrical dimensions, the dc SQUIDs fabricated at IBM²⁸² exhibit at least one order of magnitude more flux noise at 40 K than predicted by Fig. 28b; at 77 K the flux noise level is almost three orders of magnitude above that at 1 Hz. The increased temperature, besides affecting the parameters of the device, clearly brings in extra noise sources, making the temperature dependence more complicated than depicted in Fig. 28.

High- T_c thin films have strong $1/f$ -form excess noise up to kHz frequencies. The noise apparently arises from local fluctuations of flux,^{283,287-292} and it can be described by thermally activated hopping of vortices among pinning sites in the film.^{7,283,293-295} On the basis of a simplified hopping model for flux creep, an energy sensitivity of 10^{-27} J/Hz at 77 K for $L = 200 \text{ pH}$ at 1 Hz is predicted,²⁸¹ corresponding relatively well to experimental results. The enhanced flux creep is a consequence of the short coherence length, an inherent property of high- T_c materials. Furthermore, the inductance of the device can be much higher than calculated from the geometry because of percolation of current paths.²⁹⁶⁻²⁹⁸ Critical current densities of high- T_c films are affected by flux creep at high applied fields.^{292,295}

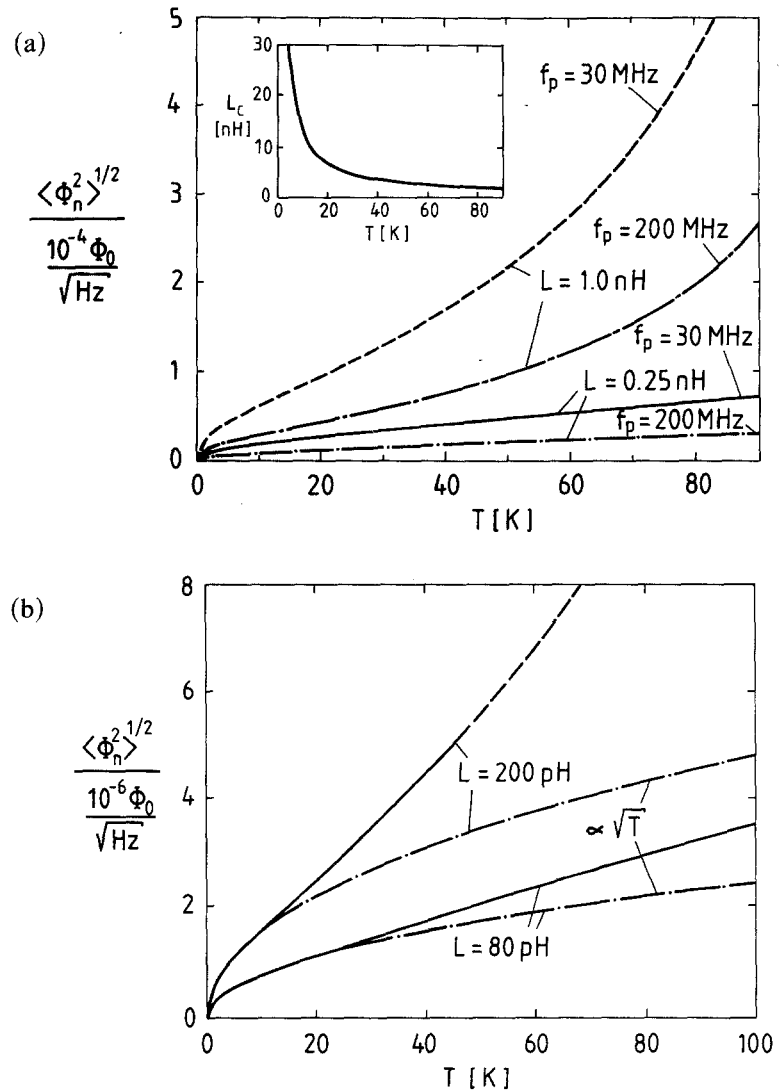


Fig. 28. (a) Flux noise $\langle \Phi_n^2 \rangle^{1/2}$ of different rf SQUIDS as a function of temperature, calculated from Eqs. (35) and (37). For the solid line, $L = 0.25 \text{ nH}$ and $f_p = 30 \text{ MHz}$; for the dash-dotted line $L = 0.25 \text{ nH}$ and $f_p = 200 \text{ MHz}$; for the dashed line $L = 1.0 \text{ nH}$ and $f_p = 30 \text{ MHz}$; for the chain-dashed line $L = 1.0 \text{ nH}$ and $f_p = 200 \text{ MHz}$. The inset presents the critical value of the inductance L_c as a function of T . (b) The optimized $\langle \Phi_n^2 \rangle^{1/2}$ for dc SQUIDS with $C = 1 \text{ pF}$ and $L = 80$ and 200 pH , obtained from simulations (see Sec. 4.1.5). The solid lines present simulated values; the dash-dotted lines show the \sqrt{T} -approximation for the temperature dependence. The dashed section of the upper curve is an extrapolation.

Even if the problem of these extra noise sources can be solved, the designers of high- T_c dc SQUIDs must face the necessary requirement for low-noise operation: $L \ll 100$ pH.

6.4. Discussion

The development of reliable high- T_c SQUIDs depends especially on the solution of two problems: 1) how to fabricate reliable, reproducible, and well-controllable junctions, and 2) how to avoid excess noise due to flux creep. With new materials it is also difficult to control the SQUID parameters; therefore, SQUIDs with a single junction are preferred in the first applications. High- T_c SQUIDs do not pose as strict requirements on the preamplifier noise temperature as conventional SQUIDs because their intrinsic noise is higher. With cooled preamplifiers, the intrinsic noise level of rf SQUIDs can be reached. For construction of practical devices, the SQUIDs themselves are not enough; many other components, such as superconducting wires and contacts, must be made. Although the low-frequency applications of high- T_c materials do not look very promising because of flux creep, R-SQUID noise thermometers and microwave SQUIDs for the measurement of rf power are candidates for high- T_c applications.

7. ELECTRONICS

7.1. General

In applications where a SQUID is used to monitor a low-frequency magnetic field, a flux-modulation technique is almost invariably used.^{299,300} As shown in Fig. 6, square-wave modulation of $\Phi_0/2$ peak-to-peak amplitude is applied to the SQUID and the output signal is detected by a demodulator circuit; the output is proportional to the deviation of the low-frequency flux from a half-multiple of Φ_0 . The phase detection scheme is applicable to all types of SQUIDs; it helps to eliminate some sources of low-frequency noise such as EMFs, drifts in the junction critical current and in SQUID parameters, and $1/f$ noise from preamplifiers. Furthermore, the detected signal is usually fed back through a resistor and a coupling coil to the SQUID ring. Since the high-gain feedback loop tends to maintain a constant flux in the SQUID, the feedback voltage is proportional to the external flux. The periodic SQUID response is thus converted to a linear one, which is independent of the amplifier gain. In general, well-designed lock-in electronics does not increase the system flux noise, but in SQUIDs with complex ΦV characteristics some loss in sensitivity may result.

The feedback electronics can lock the intrinsic flux at any multiple of Φ_0 . However, a strong external signal may kick the system from one stable

point of operation to another, resulting in a change of the output voltage. Evidently, the higher the feedback gain, the better the system can screen the SQUID loop from an external flux. The increase of the open-loop gain is ultimately limited by the modulation frequency; the feedback loop may become unstable if the gain is increased and the output of the demodulator circuit is not filtered before feeding the signal back to the SQUID ring. In rf SQUIDs the modulation frequency must be less than the bandwidth of the tank circuit. It is, however, limited in practice by the bandwidth of the lock-in circuit. In dc SQUIDs the increase of amplifier noise with frequency limits the range of modulation frequencies. SQUID electronics operated in the lock-in mode is extensively discussed in Refs. 86, 301 and 302; only the most important features will be mentioned here.

Usually, the feedback loop contains an integrator (PI controller), yielding a feedback gain $G(\omega) \approx j\omega_{\text{mod}}/\omega$; the maximum rate of flux change (slew rate) is limited to the order of $\Phi_0\omega_{\text{mod}}$ but loop stability is easily attained.⁸⁶ By increasing the frequency dependence of the feedback gain, $G(\omega) \approx j(\omega_{\text{mod}}/\omega)^\delta$, a higher slew rate can be achieved, but then the stability against variations in the loop parameters is impaired.³⁰¹ A loop filter with $\delta = 1.5$ produces a phase shift of 135°. The realization of such a filter requires, however, many components. In quiet conditions, for example inside a magnetically shielded room, a conventional PI controller is sufficient to ensure proper operation but in geomagnetic applications special attention must be paid to the feedback electronics. In multichannel applications the electronics should contain a special unit to rebalance any SQUID after the loss of lock.

The low-frequency readout circuits for different SQUIDs are usually very similar. However, the rest of the electronics may differ significantly. Next, special features of electronics for various SQUIDs are briefly discussed.

7.2. rf SQUID in the Hysteretic Mode

The electronics of the hysteretic rf SQUID is shown in Fig. 29. In this case the tank circuit impedance, and thus also the signal bandwidth, is strongly affected by energy dissipation in the SQUID. However, the loaded tank circuit impedance is related to the dissipation of the unloaded tank circuit and to the input impedance of the preamplifier. Optimal noise characteristics require that $R_{\text{opt}} \approx \alpha_{\text{exp}} R_T$, where α_{exp} is the slope of the staircase pattern (see Fig. 9), R_{opt} is the optimal source impedance of the preamplifier, and R_T is the effective tank-circuit resistance. If R_T is limited by the input impedance of the amplifier, the above condition may be difficult to satisfy. This problem is aggravated if a cooled preamplifier is used.⁹⁷ The

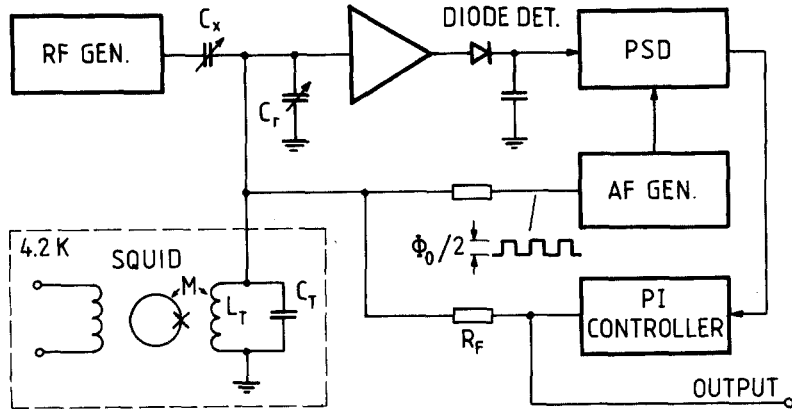


Fig. 29. Block diagram of read-out electronics suitable for hysteretic and nonhysteretic rf SQUIDS. The resonance frequency of the tank circuit is adjusted with C_r and the amplitude of the rf excitation with C_x . The hysteretic rf SQUID is operated at resonance and the variation in flux is then converted into the amplitude modulation of the tank circuit voltage; the diode detector is commonly used.

low output impedance of the hysteretic rf SQUID can be profitably utilized by increasing the flux-modulation frequency and thus constructing a device with a high slew rate.

A sufficiently high negative input impedance of a parametric amplifier used for read-out may cause the tank circuit to oscillate. The amplitude will grow until quantum jumps start to dissipate energy, and the SQUID will become self-biased on the first plateau. Ehnholm *et al.*³⁰³ realized such a readout scheme by using a varactor bridge up-converter. The use of a parametric amplifier is quite complicated; thus an improvement in sensitivity is most easily achieved by increasing the pump frequency or by replacing the room temperature preamplifier by a cooled FET amplifier.

7.3. rf SQUID in the Nonhysteretic Regime

Unlike the hysteretic SQUID, the output impedance of the inductive SQUID may become extremely high. Since the impedance is proportional to the inductance of the tank circuit, it can be easily matched to the preamplifier. As discussed in Sec. 3.2.2, the strong interaction between the SQUID and the tank circuit may increase the effective transfer frequency, but also the output impedance increases. Since \mathcal{F} depends also on bias conditions, noise optimization is very difficult. The narrow signal bandwidth limits the maximum flux-modulation frequency; thus the L-SQUID is unsuitable for high-slew-rate applications.

Since a resistive rf SQUID is usually operated in the dispersive mode, most of the problems are common with the inductive SQUID. As shown

in Sec. 3.5.3, the sensitivity of the R-SQUID noise thermometer is fundamentally dependent on the noise temperature of the preamplifier; a cooled amplifier significantly improves this noise thermometer.

7.4. Microwave SQUID

A well-matched microwave SQUID tends to pick up thermal noise from room temperature circuits and from the preamplifier; thus the input circuits, the directional coupler, the circulator, and the attenuator through which the pump signal is fed should be cooled. In principle, the signal bandwidth is very high, but the flux-modulation frequency may be limited by the narrow bandwidth of the low-noise microwave amplifier. Anyhow, the microwave SQUID with a high flux-modulation frequency and with fast feedback circuits is the right choice for high-slew-rate applications. A balanced mixer can be tuned sensitive to phase or amplitude of the reflected microwave power; this construction is thus more flexible than a diode detector. A readout circuit of the microwave SQUID can be constructed in a variety of ways; one simple receiver, including an audio-frequency flux modulator and a demodulator, is shown in Fig. 30. A circulator and an attenuator are placed at 4.2 K to reduce the amount of noise reaching the Josephson junction from the room-temperature microwave oscillator. The noise level of the M-SQUID, limited by T_A (see Sec. 3.4), can be significantly improved with a cooled preamplifier: noise temperatures of cooled commercial high-electron-mobility transistors (HEMTs) are about 5–30 K at 10 GHz.^{304,305}

7.5. dc SQUID

Since the output impedance of a typical dc SQUID is only a few ohms, a transformer is required to match it to the optimal input impedance, a few kilo-ohms, of a low-noise JFET amplifier. The modulation frequency must be high enough to avoid $1/f$ noise from the preamplifier but low enough to exclude input current noise, which increases drastically with frequency. Many switching transistors with a large gate area provide excellent noise characteristics for reasonable source impedances and are ideal for dc SQUIDs.

The low output impedance can be increased by feeding the signal through a cooled inductor into a capacitor set in parallel with the preamplifier,³⁰⁶ or by using an ordinary tuned transformer (with or without a ferrite core) immersed in liquid helium.³⁰⁷ The transformer is preferable since increased output capacitance reduces the bandwidth of the reactive transforming circuit. Wellstood *et al.*³⁰⁸ improved the slew rate by adding a transformer at room temperature and increasing the modulation frequency up to 500 kHz.

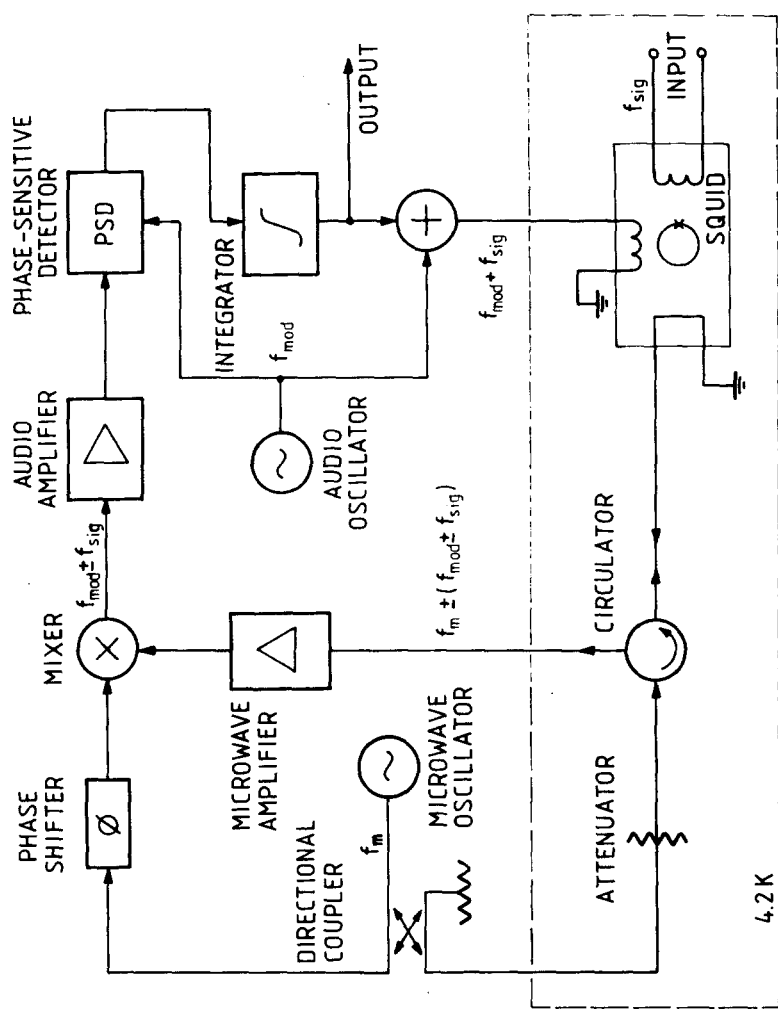


Fig. 30. Block diagram of rf SQUID electronics operated at high frequencies. The reflected power is directed through the cooled circulator into the preamplifier. The cooled attenuator prevents room temperature noise from entering the Josephson junction.

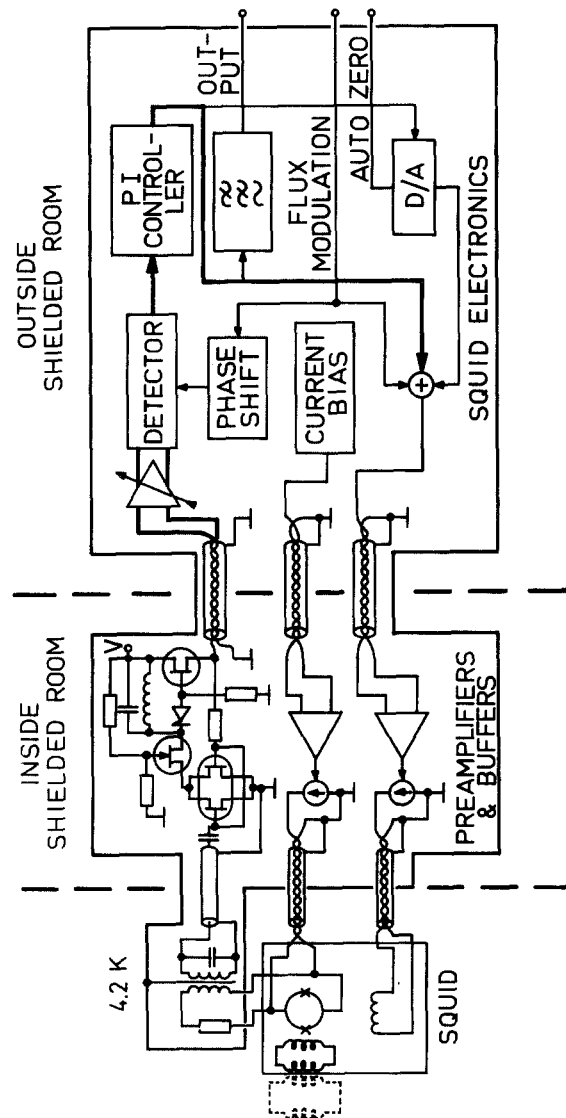


Fig. 31. Block diagram of dc SQUID electronics based on phase-sensitive detection.¹⁸⁹

A dc-SQUID readout circuit is depicted in Fig. 31. The signal from the SQUID is fed through a cooled resonant transformer into the preamplifier consisting of two FETs in parallel (Toshiba SK146). A demodulator circuit contains, in addition to the switching circuit, also an integrator and a sample-and-hold circuit, which can effectively attenuate the modulation frequency and its harmonics without introducing a phase shift at signal frequencies. The output of the demodulator is fed via a PI controller and the transconductance amplifier back to the modulation coil. The electronics is operated at 100 kHz and the cooled input circuits are designed to transform a 10- Ω SQUID impedance to 4 k Ω , which is optimal for the amplifier stage. The noise temperature of the amplifier is as low as 2 K at 100 kHz. Since the dynamic range of the dc SQUID may be extremely high, the feedback circuit must be designed with appropriate care. In Fig. 31, current sources prevent conductance fluctuations in wires and in contacts from adding noise when the system is operated with large feedback currents.

1/f noise in SQUIDs can be reduced by reversing the bias current synchronously with flux modulation.^{309,310} This scheme complicates the electronics and is thus not very tempting in devices where the simultaneous operation of many SQUIDs is required. Elegant current modulation schemes, with effective reduction of low-frequency noise, are discussed by Foglietti *et al.*³¹¹ and by Drung *et al.*³¹²

The rapid progress of instruments with multiple channels has given an impact to the development of integrated and cooled read-out circuits.^{313,314} The voltage across several series-connected SQUIDs modulated at different frequencies can be recorded by a single SQUID, and a demodulation circuit at room temperature can separate different channels.³¹⁴ Unfortunately, the circuits presented in the literature increase the noise level; by placing extra filters between the SQUIDs and the read-out electronics the aliasing effect can be avoided but a cooled multichannel unit becomes more complex. Another approach is to integrate the SQUID together with an A/D converter and a feedback circuit on a single cryogenic chip; the SQUID output voltage can be converted into digital form at low temperatures, for example, with a hysteretic dc SQUID as a comparator.^{312,315,316} An integrated SQUID magnetometer with a cryogenic feedback circuit has recently been reported by Fujimaki *et al.*³¹⁶

8. COMPARISON OF DIFFERENT TYPES OF SQUIDS: PERFORMANCE LIMITS

8.1. Main Features

The main features of different types of SQUIDs, except for the R-SQUID, are summarized in Table I. The values for the flux-to-voltage

transfer function, the forward transfer frequency, and the energy sensitivity include also expressions for the ultimate limit, possible only under ideal conditions. Typical values of the energy sensitivity for rf SQUIDS are calculated by assuming that the noise is limited by the preamplifier; ε is then obtained by dividing the amplifier noise temperature by the forward

TABLE I.
Comparison of Different Types of SQUIDS^a

Type of SQUID	Hysteretic rf SQUID	Nonhysteretic rf SQUID	Microwave	dc SQUID
$\frac{\delta V}{\delta \Phi_a}$	typ. $\frac{\omega_p}{k} \left(\frac{L_T}{L} \right)^{1/2}$ ($18 \mu\text{V}/\Phi_0$)	$\frac{1}{2} \omega_p \beta_L k Q_T \left(\frac{L_T}{L} \right)^{1/2}$ ($2 \mu\text{V}/\Phi_0$)	—	$\omega_c/2$ ($6 \mu\text{V}/\Phi_0$)
	lim. $\frac{\omega_c}{k} \left(\frac{L_T}{L} \right)^{1/2}$ ($900 \mu\text{V}/\text{Hz}^{1/2}$)	∞ (∞)	—	$\omega_c/2$ ($6 \mu\text{V}/\Phi_0$)
Forward transfer frequency \mathcal{F}	typ. $2\omega_p(1-\alpha)$ ($2\pi \cdot 30 \text{ MHz}$)	$\frac{1}{2}\omega_p \beta_L^2 k^2 Q_T$ ($2\pi \cdot 0.6 \text{ MHz}$)	$\omega_p/8$ ($2\pi \cdot 1.3 \text{ GHz}$)	$\omega_c/\sqrt{2}$ ($2\pi \cdot 0.7 \text{ GHz}$)
	lim. $2\omega_c(1-\alpha)$ ($2\pi \cdot 2 \text{ GHz}$)	∞ (∞)	$\omega_p/8$ ($2\pi \cdot 1.3 \text{ GHz}$)	$\omega_c/\sqrt{2}$ ($2\pi \cdot 0.7 \text{ GHz}$)
Energy sensitivity ε	typ. $k_B T_A / \omega_p$ ($1 \cdot 10^{-29} \text{ J/Hz}$)	$2k_B T_A / (\omega_p \beta_L k^2 Q_T)$ ($2 \cdot 10^{-27} \text{ J/Hz}$)	$2k_B T_A / \omega_p$ ($1 \cdot 10^{-31} \text{ J/Hz}$)	$8k_B T / \omega_c$ ($7 \cdot 10^{-32} \text{ J/Hz}$)
	lim. $1.5k_B T_B L^{1/2} / \omega_c$ ($2 \cdot 10^{-32} \text{ J/Hz}$)	$3k_B T / (\omega_c \beta_L)$ ($5 \cdot 10^{-32} \text{ J/Hz}$)	$4k_B T / \omega_c$ ($4 \cdot 10^{-32} \text{ J/Hz}$)	$8k_B T / \omega_c$ ($7 \cdot 10^{-33} \text{ J/Hz}$)
Bandwidth	$\omega_p/(2\alpha Q_T)$ ($2\pi \cdot 3 \text{ MHz}$)	$\omega_p/2Q_T$ ($2\pi \cdot 600 \text{ kHz}$)	$<\omega_c$ ($2\pi \cdot 1 \text{ GHz}$)	$\sim 0.2 \omega_{\text{mod}}$ ($2\pi \cdot 20 \text{ kHz}$)
Slew rate	high ($20 \Phi_0/\mu\text{sec}$)	moderate ($4 \Phi_0/\mu\text{sec}$)	very high ($10^4 \Phi_0/\mu\text{sec}$)	moderate ($0.1 \Phi_0/\mu\text{sec}$)
Forward parameters	well defined	poorly defined	—	well defined
SQUID structure	simple	simple	complex	complex
Preamplifier	simple	complex (low noise)	complex (high frequency)	simple
Main electronics	intermediate	intermediate	intermediate	simple
Multichannel applications	suitable	not suitable	possible	most suitable
Applications	biomagnetism metrology physics	physics	metrology	biomagnetism gravitation metrology physics

^aExplanations: L , SQUID inductance (0.2 nH); L_T , tank circuit inductance (10 nH); R , SQUID shunt resistance (1.3Ω); Q_T , tank circuit Q-value (100); α , rf SQUID step slope (0.2); k , coupling coefficient (0.2); β_L , $2\pi L I_c / \Phi_0$, where I_c is the critical current (0.5 for nonhysteretic and 3 for a hysteretic SQUID); ω_p , pump frequency ($2\pi \cdot 20 \text{ MHz}$ for ac SQUIDS, $2\pi \cdot 10 \text{ GHz}$ for M-SQUIDS); ω_c , R/L , the characteristic frequency ($2\pi \cdot 1 \text{ GHz}$); T , temperature (4.2 K); T_A , amplifier noise (100 K for ac SQUIDS, 300 K for M-SQUIDS).

transfer frequency. The ultimate limit for the hysteretic rf SQUID is achieved if $\omega_p \approx \omega_c$ and if the contribution of the preamplifier is made negligible; the limit was obtained from Eq. (38) with $\beta_L = 3$. In the nonhysteretic SQUID, thermal noise can be minimized by tuning the SQUID near the point of infinite gain; the value in Table I is from Eq. (36) with $\beta_L = 0.5$. The M-SQUID can, in principle, be operated in the hysteretic mode, but if $\omega_p > \omega_c$, it behaves more like a nonhysteretic SQUID. Since the M-SQUID can be realized and operated in a variety of ways, and, because it is not thoroughly analyzed in the literature, no definite lower limit is given in Table I. The typical value of the forward transfer frequency of the M-SQUID is obtained from Ref. 106, where the quasiparticle conductance is omitted; the upper limit is from Ref. 113, where the noise is estimated in the regime $\omega_p \gg \omega_c$ and the transmission line is assumed to be matched to the quasiparticle conductance. As Table I indicates, the characteristic frequency of the SQUID ring limits the SQUID performance. None of the SQUIDs can have lower noise than that produced by a resistive loop, $\epsilon = 2k_B T / \omega_c$, or lower than the quantum limit $\epsilon = \hbar/2$ (see Refs. 43, 96, 317–319). The numerical values given within parentheses are estimates for typical SQUIDs; ω_c for the state-of-the-art dc SQUIDs is somewhat higher than in Table I.

The characteristic frequency of the SQUID loop seems to limit the noise performance of all types of SQUIDs. Proper damping of the junction capacitance fixes the value of the shunt resistor; thus the reduction of both junction and loop dimensions is the key to low-noise devices. The autonomous dc SQUID nearly meets the quantum limit; however, in practice this is difficult because of parasitic capacitances and stray inductances associated with the coupling circuits. In principle, quantum-limited SQUIDs are possible, if top quality fabrication technology is available.

8.2. Fundamental Constraints of the SQUID Response

On the basis of thermal activation, the condition for the voltageless supercurrent in the junction is that the Josephson coupling energy $I_c \Phi_0 / (2\pi) \geq k_B T$, i.e., the lifetime of the voltageless state³²⁰ must be long compared to the time over which the small currents are detected. Thus, $I_c \geq 2\pi k_B T / \Phi_0$.

Another limit for SQUID performance arises from the thermal flux noise Φ_n due to dissipative elements in the SQUID loop, as demonstrated in Sec. 6.3. A high-flux noise, $\langle \Phi_n^2 \rangle^{1/2} \geq \Phi_0/2$, masks the response of the SQUID, i.e., one period in Eq. (8). Because the noise energy of the system is $\langle \Phi_n^2 \rangle / (2L) \sim k_B T$, the SQUID response is observed only if $L \leq \Phi_0^2 / (8k_B T)$.

8.3. Practical Constraints Set by Electronics

The maximum rate of change of flux a SQUID system can follow depends on both input and output circuits. The SQUID is usually operated

with lock-in electronics; the slew rate then depends on the ability of the feedback loop to track the signal without loss of lock; in general, the slew rate cannot exceed $\Phi_0\omega_{\text{mod}}$.

The signal bandwidth of the nonhysteretic SQUID is determined by the effective Q -value of the tank circuit, which in the low- g_L limit is somewhat less than the unloaded value, but becomes infinite in the high- g_L limit. The effective Q -value of the hysteretic SQUID is reduced by energy dissipation due to the hysteretic loop; therefore, the bandwidth and the slew rate are inversely proportional to the fractional slope of the voltage plateaus α . In the microwave SQUID, the bandwidth depends substantially on the impedance-matching circuit, and it can in some cases even approach the pump frequency. The slew rate of the dc SQUID is limited to moderate values in practice, because the flux-modulation frequency cannot be increased without loss of sensitivity.

As discussed above, a broadband preamplifier with negligible noise contribution is difficult to construct; the problem is avoided only in high- T_c SQUIDs. If a large signal bandwidth and a high slew rate are crucial, a microwave SQUID or a dc SQUID with a cooled preamplifier is appropriate. In Table I some numerical examples are given, omitting the possible limits caused by the lock-in electronics; only the dc SQUID is assumed to be read out via an audio-frequency transformer of 10-kHz bandwidth.

Realization of low-noise hysteretic rf-SQUID magnetometers is probably easiest: the forward parameters are well under control, the performance is not susceptible to small changes in the inductance or the critical current, and the electronics is simple. At 20 MHz, the usual operating frequency, extra resonances or parasitic capacitances do not cause severe difficulties. In the nonhysteretic SQUID, adjustment of the parameters is critical. Low-noise characteristics are achieved only with a cooled preamplifier and high-frequency operation, or by tuning the SQUID parameters close to the point of infinite gain. The microwave SQUID requires a low-capacitance junction and a special circuit to match the transmission line to the junction impedance. In addition, a low-noise preamplifier for the M-SQUID is rather expensive for practical applications. Although the electronics of the dc SQUID is easy to realize, a well-behaved, low-noise device may become complicated, since the complex dynamics requires a careful design of the coupling circuits. The simple structure of the rf SQUID and the low-noise performance of the dc SQUID with cheap electronics are the main reasons for their popularity; these features are especially important when several SQUIDs are operated simultaneously.

8.4. 1/f Noise

Low-frequency applications of SQUIDs are limited by 1/ f noise, which is associated with the quality of the device, scaling inversely with component

size.^{321,322} All SQUID elements are potential sources of $1/f$ noise: junctions, shunt resistors, the SQUID loop, and the input circuits. Some results^{283,290,310,323} indicate that the SQUID loop made of low-quality superconductor material can be the origin of the $1/f$ noise; however, most measurements^{310,311} point towards the Josephson junctions themselves. Flux creep and flow in superconducting thin films^{281,283,290} and electron traps in the junction barriers^{324–326} are *de facto* connected to the noise rise at low frequencies. In both these cases a superposition of Lorentzian spectra (see Refs. 327–329) is suggested to give rise to the $1/f$ -like behavior. Thermal fluctuations are also proposed to be related to the $1/f$ noise,^{330,331} as verified in some special experiments.³³² None of the present theories can, however, explain the scale invariance of the spectral form: thus the origin of the $1/f$ noise in the SQUIDs is still an open question. The ultimate limit of the low-frequency noise cannot be estimated on the basis of existing models; the measured values at 1 Hz vary from $2 \cdot 10^{-7} \Phi_0/\text{Hz}^{1/2}$ in dc SQUIDs with high-quality tunnel junctions¹⁹⁵ to $10^{-3} \Phi_0/\text{Hz}^{1/2}$ in high- T_c dc SQUIDs.²⁷⁶

Low-frequency fluctuations of junction critical currents are a substantial source of $1/f$ flux noise, especially in dc SQUIDs. Their contribution can, however, be eliminated by synchronous modulation of the bias current with flux modulation.^{192,309,311,312} On the contrary, the real low-frequency flux noise entering the SQUID via the loop materials, the shunt resistors, or the junctions cannot be wiped out; thus the high- T_c materials, owing to low flux pinning forces, are hardly suitable for SQUIDs in low-frequency applications.²⁸²

9. APPLICATIONS

9.1. Biomagnetic Applications

Currently, the largest area of SQUID applications is biomagnetism, the study of magnetic fields generated in living systems.^{333,334} Cellular activity in muscles and in neurons often involves large enough ion currents to give rise to detectable magnetic fields outside the body. Thus, the operation of the nervous system, the heart, and other muscles can be investigated completely noninvasively, with no mechanical contact to the body. In addition, the field produced by magnetic contaminants in the body can be used to determine the amount and distribution of foreign materials.^{335–338} Diamagnetic or paramagnetic tissues modify externally applied fields; this effect has been used to measure iron overload in the liver.³³⁹

Biomagnetic fields of interest range from about 10^{-13} T produced by cerebral activity to 10^{-9} T produced by lung contaminants. For most biomagnetic measurements, sensitive SQUID magnetometers are necessary and one must carefully shield against external disturbances.

Neuromagnetism, the study of neural functions by the measurement of magnetic fields, is currently the branch of biomagnetism attracting most interest.³⁴⁰⁻³⁴³ Magnetoencephalography (MEG) is closely related to electroencephalography (EEG): both are produced by the same cerebral events. The advantage of MEG is that magnetic fields are not much distorted by the irregularities of the skull. Therefore, one can determine locations of brain activity more accurately with MEG than with EEG.

Figure 32 shows the seven-channel SQUID magnetometer at the Helsinki University of Technology.³⁴⁴ The device was realized with dc SQUIDs provided by IBM.¹⁹⁵ Each channel has a flux transformer in the first-order gradiometer configuration so as to be insensitive to homogeneous fields. In Fig. 33, magnetic fields evoked by auditory stimuli are shown as recorded with the seven-channel magnetometer.³⁴⁵ From the field pattern, the location, orientation, and amplitude of the underlying cerebral current source can be estimated.

Although MEG has already proven capable of bringing unique information about nervous activity, it is not yet clear what its diagnostic value will be; clinical experiments are just beginning as multichannel magnetometers become available. MEG and EEG are the only noninvasive tools to study the real-time operation of the brain. EEG is already in routine use in hospitals, but it is not capable of revealing locations of brain activity with sufficient precision. In addition to spatial accuracy, one advantage of magnetic measurements is that the patient can be studied without time-consuming preparation. In EEG, it may take an hour to attach 32 electrodes to the scalp.

While MEG is a valuable new tool for basic studies of the brain, magnetic measurements of the heart are expected to be useful only if they bring clinically significant information. Because the need to diagnose the heart function is very common and very important, cardiomagnetism has a potentially important future, although a breakthrough is still to be made. Currently, most magnetic heart measurements are analyzed in a similar fashion with ECG, with no attempt to determine source locations. Pathological heart activity can be located only with an uncertainty of about 2 cm.^{346,347} One of the obstacles to the determination of the spatial distribution of heart activity is that the conductivity geometry of the heart and its surroundings is very complicated and difficult to take into account.³⁴⁸⁻³⁵⁰ In addition to the improvement of methods to utilize the spatial information in MCG, the development of arrays of SQUID magnetometers for cardiomagnetism is essential for the acceptance of MCG in hospital use.

For a more thorough discussion on the biomagnetic measurements, especially utilizing multiple simultaneous recordings, see Chapter 3 of the companion paper.¹⁵

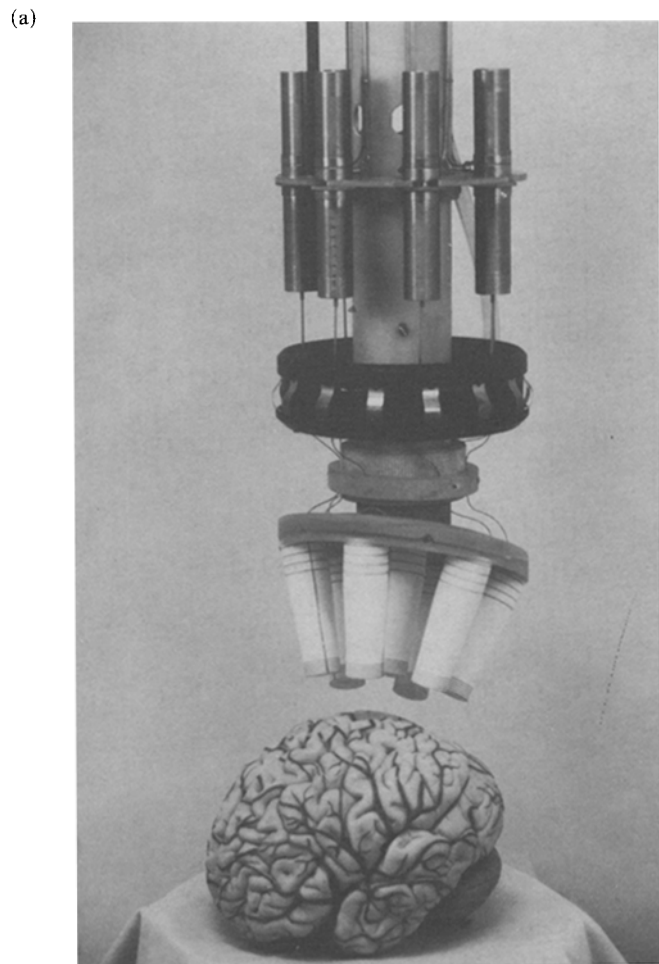


Fig. 32. The Helsinki seven-channel gradiometer,³⁴⁴ which uses SQUIDs made by IBM.¹⁹⁵ (a) Sensor coils shown at a typical distance from a model brain. (b) Mechanical construction and coil configuration (see next page).

9.2. Metrology

Precision measurements and the absolute realization of units often require sensitive null detectors and amplifiers; the SQUID is widely used in such applications. In Secs. 3.4 and 3.5, the measurement of rf attenuation and the determination of the absolute temperature have been discussed already. Attenuation measurements are based on the periodic response of

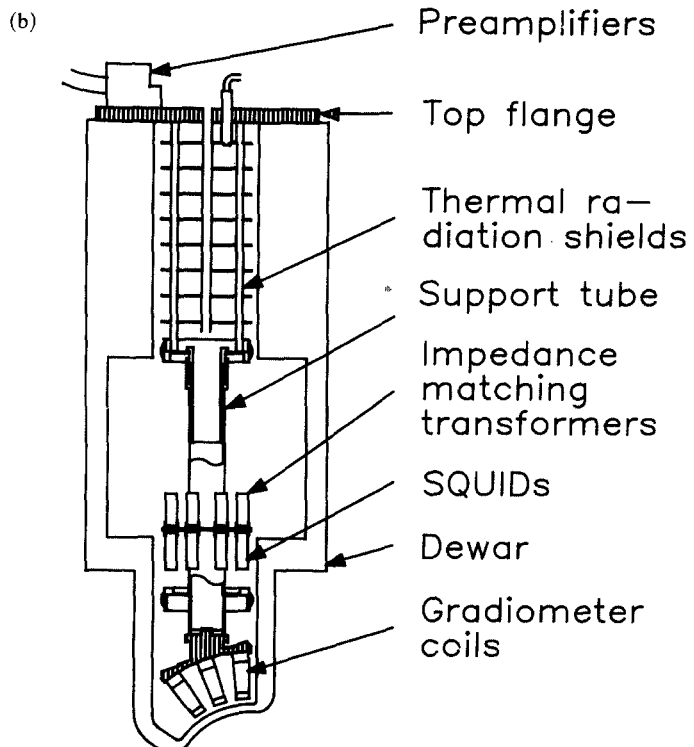


Fig. 32. Continued.

the SQUID to an external flux, while in temperature measurements, the parametric up-conversion efficiency of the R-SQUID or the high sensitivity of the dc SQUID is utilized. There is a wide range of applications where the high sensitivity of the SQUID is taken advantage of, as is extensively discussed by Gallop³ and by Petley.³⁵¹ The SQUID has very low input impedance at low frequencies and, therefore, it is suitable for voltage measurements only if the source impedance is low; a voltage drop across a metal block, a metallic or a superconducting contact etc.,³⁵²⁻³⁵⁵ and a voltage between two Josephson junctions can be accurately measured with a SQUID.³⁵⁶

In the highly reproducible Josephson voltage standards, SQUIDs act as null detectors to balance the output of the resistive voltage divider to the output voltage generated by the Josephson junction.^{99,357-362} The same SQUID is usually used as a magnetic sensor in a Cryogenic Current Comparator (CCC),³⁶³⁻³⁶⁶ which, in turn, can be used to calibrate the ratio of the voltage divider. The CCC is excellent for the measurements of ratios

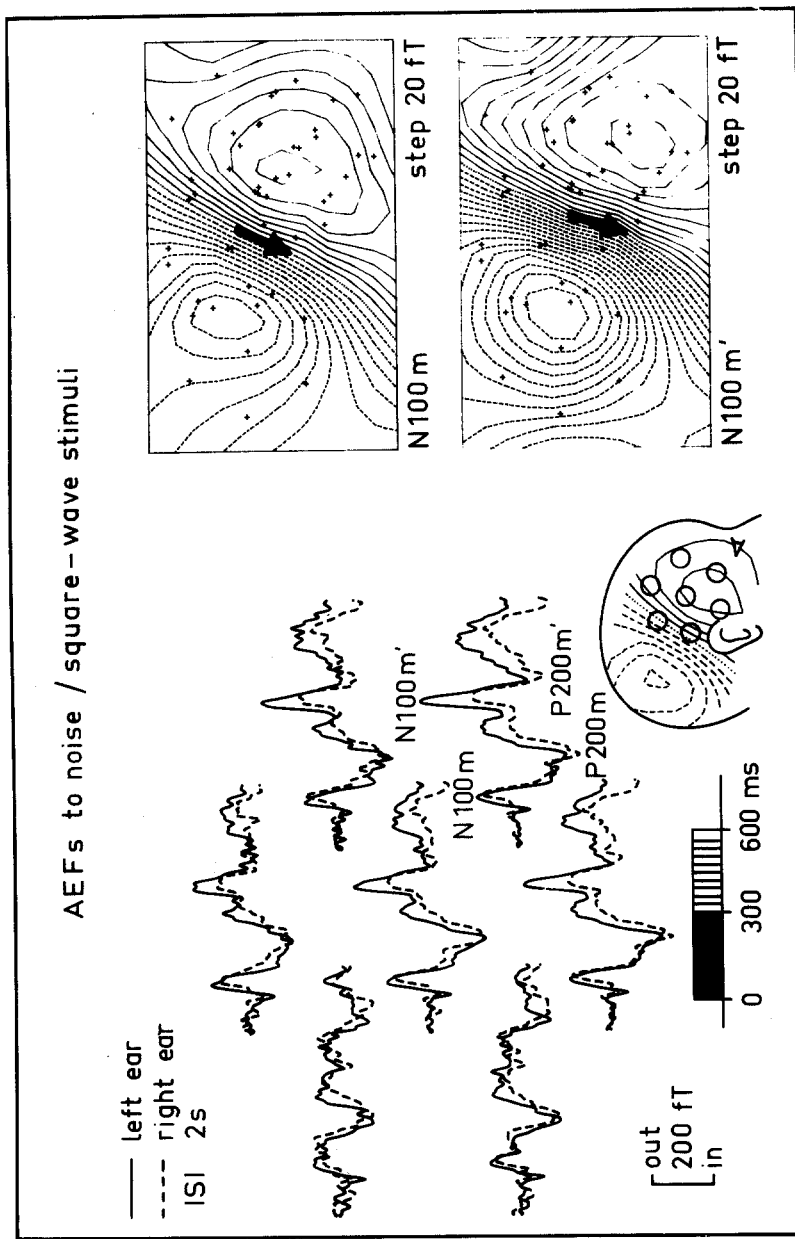


Fig. 33. Responses evoked by sound stimuli to the left ear (solid lines) and to the right ear (dashed), as recorded with the Helsinki 7-channel SQUID magnetometer.³⁴⁵ The stimulus begins with band-limited white noise (marked black on the time axis) and ends with a 250-Hz square-wave tone (vertical-line shading). The display passband is 0.05–45 Hz; 120 responses were averaged to improve the signal-to-noise ratio. The locations of the seven first-order gradiometers are shown as circles on the head profile. On the right, magnetic field isocontour maps are shown for the deflections that occur approximately 100 ms after the beginning of the noise burst (N100m) and after the transition from noise to square wave (N100m'). The separation between the isocontour lines is 20 fT.

of room temperature resistors and for transferring the precision of the quantum-Hall resistance down to the one-ohm level.³⁶⁷⁻³⁷¹ The quantum-Hall experiments benefit, in particular, from the high sensitivity and the low ratio error of the CCC, since only a very low current can be fed through a Hall component. Although demonstrated to work well up to 10 kHz,³⁷² the CCCs are usually operated at low frequencies.

Figure 34 shows the principle of the one-to-one cryogenic current comparator. Because of the superconductivity of the shield, the inner surface of the infinitely long superconducting tube must carry the resultant of the two currents I_1 and I_2 , flowing in opposite directions. The current returns evenly distributed on the outer surface and, therefore, carries no information on the position of the current-carrying wires. The SQUID sensing the flux, usually via a flux transformer, is in balance only when the two currents are equal. Bending one end of the tube inside the other end and thus avoiding the end effect, a practical, so called overlapped-type comparator can be formed.³⁶⁵ Such a device,⁹⁹ with a sensitivity of $0.1 \text{ nA/Hz}^{1/2}$, is depicted in Fig. 34b. In this instrument the flux leaking to the window of the bent tube is transferred to the rf SQUID via a planar flux transformer. The shields of the CCC can be constructed in a variety of ways and, in principle, the inductance can be increased with iron cores. The toroidal comparator with special coaxial windings is demonstrated to be convenient in ac ratio measurements since it produces a lower parasitic capacitance across the ratio windings.³⁷² It can also be used to measure or to stabilize a charged-particle beam directed through a window of the toroid.³⁷³

A SQUID can be used to establish a digital current scale, but nonlinear effects restrict its use in practice. The dc current and thus also the voltage appearing across the cryogenic resistor can, however, be stabilized very accurately by a SQUID.^{374,375} A stable voltage source is very useful in calibrating electrochemical standard cells by a Josephson array³⁷⁶⁻³⁷⁸ or in maintaining the voltage between Josephson measurements. Coupling several SQUIDs together, voltage pulses can be detected by a sampling technique, or very fast A/D converters can be realized.³⁷⁹

SQUIDs have an important role in determining fundamental constants. We have already mentioned the Josephson voltage standard, which can measure $h/2e$, and the quantum-Hall effect, which can determine the fine-structure constant α .³⁶⁷ The ampere and thus $h/2e$ can be defined by levitating a superconducting mass by a current-carrying coil.³⁸⁰⁻³⁸³ In these measurements a SQUID can be used to measure or stabilize the current. There are also experiments and proposals for determining the gyromagnetic ratio of the proton γ_p ,^{384,385} the effective mass of the electron m_e ,^{386,387} or the ratio e/m_e ³⁸⁸ with SQUID magnetometers.

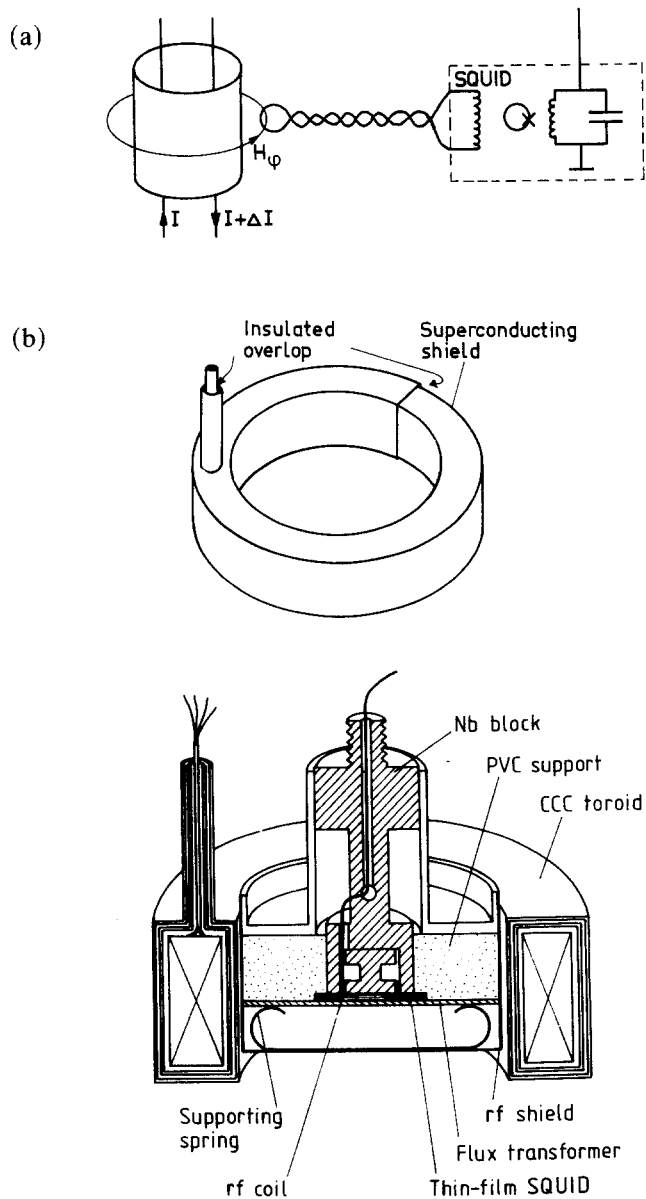


Fig. 34. (a) Principle of the cryogenic current comparator (CCC). The SQUID detects the magnetic field generated by the current ΔI flowing on the outer surface of the long superconducting tube. (b) A realization⁹³ of CCC.

9.3. Other Applications

9.3.1. *Geomagnetism*

Geomagnetic research and surveying are two major applications of SQUID magnetometers. The low noise obtainable even with compact detection coils, the large dynamic range, the wide frequency band that starts from dc, and the selectivity to specific field or gradient components are the main advantages of SQUID systems. However, the need of liquid helium may cause problems at remote observation sites that are often necessary in geomagnetic studies; large dewars are needed to allow long maintenance-free operation. Small, closed-cycle cryocoolers would be most welcome, but they must not cause magnetic or mechanical disturbances to the measurement, which must be performed without shielding. The sensitivity of SQUIDs to rf interference and mechanical vibrations complicates their field use. Besides, the high cost of multi-SQUID systems is perhaps the main factor limiting their use in geomagnetism.

Since the signals of interest are often only small variations, superposed on large field fluctuations that are not relevant to the particular event under study, the slew rate and the dynamic range must be high. The electronics must meet these criteria in the frequency range of several tens of kHz, to ensure operation without losing flux lock. In addition, since the signals of interest extend to very low frequencies, low $1/f$ noise, and stable operation, free from flux jumps and drifts, are required. A compact integrated magnetometer with a high slew rate, intended specifically for geomagnetic studies, has been introduced by Wellstood *et al.*³⁰⁸

In geomagnetic studies, usually three SQUIDS are required to measure all components of the magnetic field. Measurements of the magnetic field gradient tensor may also be performed to detect possible anomalies in the Earth's field; a gradiometer gives a strong signal when the sensor is moved over the anomaly.

In magnetotelluric studies, the magnetic and electric fields, caused by incident electromagnetic waves, are measured simultaneously near the ground. These waves, typically from 10^{-4} to 100 Hz, are generated by ionospheric and thunderstorm activity. From the measured field components, as functions of frequency, the impedance tensor $Z(\omega)$ can be determined. Because of noise, the estimates of $Z(\omega)$ are, however, unreliable. To overcome this problem, a remote reference measurement is carried out simultaneously,³⁸⁹ or an artificial variable-frequency electromagnetic source is used.³⁹⁰ In the latter method, a reference signal is transmitted to the measurement station for lock-in detection. The reference measurement site senses mainly naturally-occurring geomagnetic fluctuations, which in this controlled-source paradigm constitute noise; this background scales roughly

as $1/f$ below 1 Hz, easily outweighing the signal.

The measurements of remanent magnetization or magnetic susceptibility of rock samples was perhaps the first application of SQUIDs to geological studies. In paleomagnetism one investigates the history of the Earth's magnetic field; another important area of interest is the identification of magnetic phases in samples. In both cases, a dewar with room temperature access to the sample volume is needed; the devices have a coil to generate a magnetizing field and pickup coils to measure the remanent field components in the axial and transverse directions.

Use of SQUID magnetometers in geophysics has been reviewed in detail by Clarke.³⁹¹ Several applications have been proposed and some feasibility studies made, although no full-scale tests have been carried out. These include the detection of stress changes in the ground prior to earthquakes,³⁹² detection of Schumann resonances in the ionosphere,³⁹³ and locating artificially induced fractures in the ground that are made to enhance oil or gas flow to a collecting borehole in weakly permeable rock regions. In addition to the measurement of the Earth's magnetic field, SQUIDs are used in gravimeters to detect anomalies. Geomagnetic magnetometers have been made commercially by BTI³⁰⁹, CTF, and Cryogenic Consultants, Ltd.*

9.3.2. Accelerometers, Gravimeters, Displacement Sensors

Very small displacements and accelerations can be detected with the help of a superconducting proof mass, suspended by springs or by magnetic levitation to allow free movement with respect to a coil, which is part of a closed superconducting circuit. The current flowing through the coil, monitored by a SQUID, becomes a very sensitive function of the distance to the proof mass. In practical devices, the test mass is usually a superconducting diaphragm, and the coils are flat, as in the original work of Paik.³⁹⁴ Several proof masses and coil sets connected to different SQUIDs may be arranged to measure the sum and difference phases of acceleration, gravitational gradient tensor components, angular accelerations, etc. The devices are applied for detecting anomalies and for measuring the gradient tensor to improve inertial navigation (see, for example, Refs. 395 and 396); sensitivities better than $10^{-9} \text{ sec}^{-2}/\text{Hz}^{1/2}$ can be achieved. These instruments have been used for sensing the movements of gravitational wave antennae (see, for example, Refs. 397 and 398) and for measuring transmitter movements in Mössbauer spectroscopy with subatomic precision, of the order of $10^{-15} \text{ m}/\text{Hz}^{1/2}$.³⁹⁹ Besides this inductance-modulated technique, piezoelectric and capacitive sensing with SQUIDs as preamplifiers have been used in gravitational wave antennae as well.^{400,401}

*CTF Systems, Inc., Port Coquitlan, British Columbia, Canada V3C1M9. Cryogenic Consultants, Ltd., Metrostore Building, 231 The Vale, London W3 7QS.

9.3.3. Monopole Detectors

SQUIDs have been used to detect magnetic monopoles that are predicted by grand unification theories. A monopole passing through a superconducting loop changes the enclosed flux by $2\Phi_0$, providing a signal that is independent of mass or velocity. So far, only one candidate event has been reported,⁴⁰² recorded with a four-turn 5-cm diameter coil; later, the same group reported a coincidence detector with three orthogonal 71-cm² coils:⁴⁰³ a monopole passing through the device should be detected by all loops. In a period of 150 days, however, no monopole events were found.

A monopole detector should have as large an area as possible to enhance the probability for the passage of a monopole; then, however, ambient field variations have to be very carefully eliminated. SQUID sensors with stable operation and freedom from flux trapping are required; the pickup coils are usually operated inside superconducting and metal shields.

The immunity to spurious signals can be further enhanced by using gradiometers. Planar high-order gradiometric sensors⁴⁰⁴ provide adequate rejection of external disturbances in ambient fields of the order of 1 μT .^{404,405} The planar sensors of IBM^{406–408} have six independent coils covering each face of a parallelepiped; a monopole passing through the detector causes a signal in exactly two of the six coils. The dc SQUID detector reported recently⁴⁰⁸ has dimensions of 26 × 26 × 380 cm³. The Stanford group has constructed an octagonal-shaped detector with eight independent 17 × 521 cm² gradiometers.⁴⁰⁹

All the devices have been operated several hundreds of days; the null results imply an observed upper limit of $1.5 \times 10^{-8} \text{ m}^{-2} \text{ sr}^{-1} \text{ sec}^{-1}$ (90% confidence level) for the magnetic monopole flux.⁴⁰⁸ This is still three orders of magnitude higher than the theoretically predicted Parker bound.⁴¹⁰ With the high- T_c superconductors, it might be possible to fabricate very large sensor arrays with which the theoretical bound could be reached in a couple of years. However, 1/f noise and flux creep in these ceramic superconductors may severely limit their use.

9.3.4. Other Physical Experiments

Many rather nonstandard applications of SQUIDs have been reviewed in detail by Cabrera⁴¹¹ and by Fairbank,⁴¹² and recently by Odehnal.⁴¹³ Often very small signals are monitored, requiring ultralow-noise SQUIDs.

SQUIDs have found much use in ultralow-temperature physics experiments as detectors of susceptibility and in NMR measurements. SQUIDs were first used to measure the average magnetization of the sample (longitudinal mode), both in swept-frequency, continuous-wave (cw) mode and in pulsed excitation.⁴¹⁴ In low-frequency NMR, SQUIDs are superior to conventional amplifiers; below a few hundred kHz increased noise

significantly limits the bandwidth of FET amplifiers. SQUIDs have been employed for static susceptibility and continuous-wave measurements, for example, to find the antiferromagnetic transition of copper nuclei, occurring at 60 nK in zero field.⁴¹⁵ The SQUID is also suitable for detecting the ac component of the magnetization (transversal mode), using cw^{303,416,417} or pulsed excitation.⁴¹⁸ In the latter experiment, the free induction decay signal frequency was below 50 kHz. Recording of FID signals at 2 MHz⁴¹⁹ as well as NQR signals at 30 MHz,⁴²⁰⁻⁴²² using a dc SQUID preamplifier, have been demonstrated.

SQUID NMR is, however, susceptible to flux trapping and flux creep in μ -metal and superconducting shields. This can be a real problem in many cryostats since often strong magnetic fields are used, for example, for cooling by adiabatic nuclear demagnetization.⁴¹⁵

NMR on ³He samples, with SQUID detection and field stabilization by means of a superconducting shield, allows the construction of accurate gyroscopes; the angles through which the gyro has rotated can be found by integrating the frequency shifts from the free precession magnetometer, providing a readout of the absolute magnetic field as well.⁴²³ A gyroscope may also be constructed from a rotating superconducting body inside a SQUID pickup loop; the spinning body generates a London magnetic moment whose precession is sensed as a flux change in the pickup loop.

From the numerous proposals for use of SQUID magnetometers in basic physics, we take only one additional example: the superconductive gyroscope to measure effects caused by its motion through the Earth's curved, static spacetime geometry and by the Earth's rotation, dragging the local inertial frames along with it, as predicted by the general theory of relativity.⁴²⁴⁻⁴²⁷ In a 660-km high polar orbit around the Earth, the geodetic and frame-dragging effects are expected to be 6.6 arc-sec/yr and 0.042 arc-sec/yr, respectively. To reach a sensitivity of $3 \cdot 10^{-4}$ arc-sec/yr, a rotor with a homogeneity better than $3 \cdot 10^{-7}$ and a surface deviation from sphericity less than 20 nm peak-to-valley is required. If these conditions can be met, the principal source of error in the gyroscope readout is the SQUID; a very low $1/f$ noise is necessary. The signal is modulated at 1.67 mHz since the spacecraft, together with the gyroscope, rolls around an axis directed to a guide star with a period of 10 minutes. To reach an integration time of $\ll 5$ hr, an energy sensitivity of $3 \cdot 10^{-29}$ J/Hz at 1.67 mHz is necessary. The spacecraft for this experiment is planned to be launched in 1995.

10. CONCLUSIONS

During the last few years, understanding of Josephson devices, particularly SQUIDs, has increased significantly as a consequence of the general interest in nonlinear dynamics. The different parameters and parasitic

elements of SQUIDs are now understood sufficiently well for systematic design and device optimization. The fabrication technology of thin-film SQUIDs has also greatly improved, all-refractory-material junctions have increased the reproducibility of the devices and lowered the low-frequency noise. There are, however, many challenges in the development of SQUIDs for multichannel instruments, in applying new high- T_c materials, and in constructing thin-film circuits with higher degree of integration.

The ultimate sensitivity of both single- and double-junction SQUIDs is limited by the characteristic frequency $\omega_c = R/L$ of the SQUID loop. The sensitivity of an optimized dc SQUID is limited primarily by two parameters determined by the fabrication process: loop inductance and junction capacitance. Both should be minimized; thus the fabrication of low-noise SQUIDs requires good resolution in patterning. In the case of rf SQUIDs, the sensitivity is limited by the pump frequency and preamplifier noise; the requirements for fabrication are not as strict as for dc SQUIDs.

The most important difference between single- and double-junction SQUIDs is that the latter are self-pumped devices, requiring no external high-frequency tank circuit. Thus the dc SQUID can be operated with much simpler electronics than the rf SQUID. On the other hand, the autonomous nature of the dc SQUID makes it very sensitive to external resonant circuits coupled to its dynamics: the problem of coupling the signal coil to the dc SQUID has found a satisfactory solution only recently. The geometrical dimensions of an optimized dc SQUID must meet strict conditions to control the different noise sources.

High- T_c materials have opened new possibilities by increasing the operating temperature of SQUIDs. However, they have introduced some completely new problems. Because of the extremely short coherence length, a conventional junction structure is not possible, and increased flux creep reduces the critical current of the junctions and creates a very high noise level. The models presented in this article are valid for the high- T_c SQUIDs except that there are additional phenomena, such as flux creep, that must be incorporated in the models. The short coherence length can prevent the application of high- T_c materials for certain devices; at low frequencies flux motion can completely ruin their sensitivity.

Difficulties in the use of SQUIDs can be overcome; excellent sensitivity can be achieved also in practical devices. SQUIDs have undoubtedly found their place as scientific instruments. One of the most promising applications is the noninvasive detection of biomagnetic signals from the human brain and the heart; the scope of clinical applications of the method is still unknown. The use of SQUIDs in precision metrology is natural, and a variety of other applications exist where the outstanding properties of SQUIDs as low-frequency magnetic sensors could be utilized.

ACKNOWLEDGMENTS

We thank Juhani Kurkijärvi, Olli V. Lounasmaa, Milan Odehnal, and Pekka Somervuo for suggestions and criticism; Risto Mutikainen and Jorma Salmi for sharing their views on fabrication technology; Hannu Sipola for reviewing the manuscript. Financial support of Telecommunications Laboratories of Posts and Telecommunications of Finland, SITRA and TEKES foundations, and the Academy of Finland is acknowledged.

REFERENCES

1. A. Barone and G. Paterno, *Physics and Applications of the Josephson Effect* (Wiley, New York, 1982).
2. T. Van Duzer and C. W. Turner, *Principles of Superconductive Devices and Circuits* (Elsevier North-Holland, New York, 1981).
3. J. C. Gallop, *Metrologia* **18**, 67 (1982).
4. K. K. Likharev, *Dynamics of Josephson Junctions and Circuits* (Gordon and Breach, New York, 1986).
5. O. V. Lounasmaa, *Experimental Principles and Methods Below 1 K* (Academic Press, New York, 1974).
6. L. Solymar, *Superconductive Tunnelling and Applications* (Chapman and Hall, London, 1972).
7. M. Tinkham, *Introduction to Superconductivity* (McGraw-Hill, New York, 1975).
8. R. C. Jaklevic, J. Lambe, A. H. Silver, and J. E. Mercereau, *Phys. Rev. Lett.* **12**, 159 (1964).
9. R. C. Jaklevic, J. Lambe, J. E. Mercereau, and A. H. Silver, *Phys. Rev. A* **140**, 1628 (1965).
10. J. Clarke, *Philos. Mag.* **13**, 115 (1966).
11. J. Clarke, W. M. Goubau, and M. B. Ketchen, *J. Low Temp. Phys.* **25**, 99 (1976).
12. C. D. Tesche and J. Clarke, *J. Low Temp. Phys.* **29**, 301 (1977).
13. A. H. Silver and J. E. Zimmerman, *Phys. Rev.* **157**, 317 (1967).
14. J. G. Bednorz and K. A. Müller, *Z. Phys. B* **64**, 189 (1986).
15. R. Ilmoniemi, J. Knuutila, T. Ryhänen, and H. Seppä, in *Progress in Low Temperature Physics*, Vol. XII, D. Brewer, ed. (Elsevier, New York, 1989).
16. J. Bardeen, L. N. Cooper, and J. R. Schrieffer, *Phys. Rev.* **108**, 1175 (1957).
17. B. D. Josephson, *Phys. Lett.* **1**, 251 (1962).
18. V. Ambegaokar and A. Baratoff, *Phys. Rev. Lett.* **10**, 486 (1963), erratum; *Phys. Rev. Lett.* **11**, 104 (1963).
19. B. D. Josephson, *Rev. Mod. Phys.* **36**, 216 (1964).
20. B. D. Josephson, *Adv. Phys.* **14**, 419 (1965).
21. P. W. Anderson and J. M. Rowell, *Phys. Rev. Lett.* **10**, 230 (1963).
22. J. M. Rowell, P. W. Anderson, and D. E. Thomas, *Phys. Rev. Lett.* **10**, 334 (1963).
23. J. M. Rowell, *Phys. Rev. Lett.* **11**, 200 (1963).
24. B. N. Taylor and E. Burstein, *Phys. Rev. Lett.* **10**, 14 (1963).
25. C. J. Adkins, *Philos. Mag.* **8**, 1051 (1963).
26. N. F. Pedersen, T. F. Finnegan and D. N. Langenberg, in *Proceedings of the 13th International Conference on Low Temperature Physics*, Boulder, Vol. 3, K. D. Timmerhaus, W. J. O'Sullivan, and E. F. Hammel, eds. (Plenum, New York, 1972), p. 268.
27. C. M. Falco, W. H. Parker and S. E. Trullinger, *Phys. Rev. Lett.* **31**, 933 (1973), erratum; *Phys. Rev. Lett.* **31**, 1476 (1973).
28. J. M. Rowell, *IEEE Trans. Magn.* **MAG-23**, 380 (1987).
29. N. F. Pedersen and K. Saemark, *Physica (Utrecht)* **69**, 572 (1973).
30. D. A. Vincent and B. S. Deaver, Jr., *Phys. Rev. Lett.* **32**, 212 (1974).
31. J. Hansma, *J. Appl. Phys.* **44**, 4191 (1973).
32. M. Nisenoff, *Rev. Phys. Appl.* **5**, 21 (1970).

33. R. Rifkin, D. A. Vincent, B. S. Deaver, Jr., and P. K. Hansma, *J. Appl. Phys.* **47**, 2645 (1976).
34. S. N. Erné, H. Luther, and H. J. Scheer, in *SQUID '80, Superconducting Quantum Interference Devices and Their Applications*, H. D. Hahlbohm and H. Lübbig, eds. (Walter de Gruyter, Berlin, 1980), p. 109.
35. S. N. Erné and H. Luther, *J. Appl. Phys.* **52**, 2918 (1981).
36. D. E. McCumber, *J. Appl. Phys.* **7**, 3113 (1968).
37. W. C. Stewart, *Appl. Phys. Lett.* **12**, 277 (1968).
38. J. Kurkijärvi and V. Ambegaokar, *Phys. Lett.* **31A**, 314 (1970).
39. J. A. Ketoja, J. Kurkijärvi, and R. K. Ritala, *Phys. Lett.* **105A**, 425 (1985).
40. H. A. Kramers, *Physica* **7**, 284 (1940).
41. V. Ambegaokar and B. I. Halperin, *Phys. Rev. Lett.* **22**, 1364 (1969).
42. R. F. Voss, *J. Low Temp. Phys.* **42**, 151 (1981).
43. V. V. Danilov, K. K. Likharev, and A. B. Zorin, *IEEE Trans. Magn.* **MAG-19**, 572 (1983).
44. H. Seppä, *J. Appl. Phys.* **55**, 1578 (1984).
45. R. J. Soulen, Jr. and D. Van Vechten, *Phys. Rev. B* **36**, 239 (1987).
46. W. C. Scott, *Appl. Phys. Lett.* **17**, 166 (1970).
47. W. C. Stewart, *J. Appl. Phys.* **45**, 452 (1974).
48. K. Matsuo, *Suppl. Prog. Theor. Phys.* **69**, 301 (1980).
49. A. B. Zorin, K. K. Likharev, and S. I. Turovets, *IEEE Trans. Magn.* **MAG-19**, 629 (1983).
50. R. E. Harris, *J. Appl. Phys.* **48**, 5188 (1977).
51. R. I. Gayley, *J. Appl. Phys.* **52**, 1411 (1981).
52. V. K. Semenov, A. A. Odintsov and A. B. Zorin, in *SQUID '85, Superconducting Quantum Interference Devices and Their Applications*, H. D. Hahlbohm and H. Lübbig, eds. (Walter de Gruyter, Berlin, 1985), p. 71.
53. H. Kratz and W. Jutzi, *IEEE Trans. Magn.* **MAG-23**, 731 (1987).
54. W. Jutzi, E. Crocoll and J. Marz, *Jpn. J. Appl. Phys.* **26-3**, 1589 (1987).
55. M. J. Stephen, *Phys. Rev. Lett.* **21**, 1629 (1968).
56. M. J. Stephen, *Phys. Rev.* **182**, 531 (1969).
57. M. J. Stephen, *Phys. Rev.* **186**, 393 (1969).
58. D. J. Scalapino, in *Proceedings of the Symposium on the Physics of Superconducting Devices*, B. S. Deaver, Jr. ed. (University of Virginia Press, Charlottesville, 1968).
59. A. J. Dahm, A. Denestein, D. N. Langenberg, W. H. Parker, D. Rogovin, and D. J. Scalapino, *Phys. Rev. Lett.* **22**, 1416 (1969).
60. D. Rogovin and D. J. Scalapino, *Ann. Phys.* **86**, 1 (1974).
61. K. K. Likharev, *Rev. Mod. Phys.* **51**, 101 (1979).
62. Y. Aharonov and D. Bohm, *Phys. Rev.* **115**, 485 (1959).
63. R. G. Chambers, *Phys. Rev. Lett.* **5**, 3 (1960).
64. M. Büttiker, in *SQUID '85, Superconducting Quantum Interference Devices and Their Applications*, H. D. Hahlbohm and H. Lübbig, eds. (Walter de Gruyter, Berlin, 1985), p. 529.
65. R. A. Webb, S. Washburn, C. P. Umbach, and R. B. Laibowitz, in *SQUID '85, Superconducting Quantum Interference Devices and Their Applications*, H. D. Hahlbohm and H. Lübbig, eds. (Walter de Gruyter, Berlin, 1985), p. 561.
66. A. van der Ziel, *J. Appl. Phys.* **19**, 999 (1948).
67. L. A. Blackwell and K. L. Kotzebue, *Semiconductor-Diode Parametric Amplifiers* (Prentice-Hall, Englewood Cliffs, New Jersey, 1961).
68. K. K. N. Chang, *Parametric and Tunnel Diodes* (Prentice-Hall, Englewood Cliffs, New Jersey, 1964).
69. S. N. Erné, H.-D. Hahlbohm, and H. Lübbig, *J. Appl. Phys.* **47**, 5440 (1976).
70. V. V. Danilov, K. K. Likharev, and O. V. Snigirev, in *SQUID '80, Superconducting Quantum Interference Devices and Their Applications*, H. D. Hahlbohm and H. Lübbig, eds. (Walter de Gruyter, Berlin, 1980), p. 473.
71. I. M. Dmitrenko, G. M. Tsoi, V. I. Shnyrkov, and V. V. Kartsovnik, *J. Low Temp. Phys.* **49**, 417 (1982).
72. H. A. Notarys, R. H. Wang, and J. E. Mercereau, *Proc. IEEE* **61**, 79 (1973).
73. D. Pascal and M. Sauzade, *J. Appl. Phys.* **45**, 3085 (1974).
74. R. A. Buhrman and L. D. Jackel, *IEEE Trans. Magn.* **MAG-13**, 879 (1977).

75. O. H. Soerensen, *J. Appl. Phys.* **47**, 5030 (1976).
76. A. Callegari and B. S. Deaver, Jr., *J. Appl. Phys.* **48**, 5328 (1977).
77. V. I. Shnyrkov, V. A. Khlus, and G. M. Tsoi, *J. Low Temp. Phys.* **39**, 477 (1980).
78. M. Nisenoff and S. Wolf, *Phys. Rev. B* **12**, 1712 (1975).
79. T. A. Fulton, L. N. Dunkleberger, and R. C. Dynes, *Phys. Rev. B* **6**, 855 (1972).
80. B. V. Vasilev, V. V. Danilov, and K. K. Likharev, *IEEE Trans. Magn.* **MAG-11**, 743 (1975).
81. R. A. Buhrman, in *SQUID '76, Superconducting Quantum Interference Devices and Their Applications*, H. D. Hahlbohm and H. Lübbig, eds. (Walter de Gruyter, Berlin, 1977), p. 395.
82. G. J. Ehnholm, *J. Low Temp. Phys.* **29**, 1 (1977).
83. J. E. Zimmerman, P. Thiene, and J. T. Harding, *J. Appl. Phys.* **41**, 1572 (1970).
84. J. E. Mercereau, *Rev. Phys. Appl.* **5**, 13 (1970).
85. W. W. Webb, *IEEE Trans. Magn.* **MAG-8**, 51 (1972).
86. R. P. Giffard, R. A. Webb, and J. C. Wheatley, *J. Low Temp. Phys.* **6**, 533 (1972).
87. J. Clarke, *Proc. IEEE* **61**, 8 (1973).
88. L. D. Jackel and R. A. Buhrman, *J. Low Temp. Phys.* **19**, 201 (1975).
89. M. B. Simmonds and W. H. Parker, *J. Appl. Phys.* **42**, 38 (1971).
90. J. Kurkijärvi, *Phys. Rev. B* **6**, 832 (1972).
91. J. Kurkijärvi and W. W. Webb, in *Proceedings of the 1972 Applied Superconductivity Conference* (IEEE, New York, 1972), p. 581.
92. J. Kurkijärvi, *J. Appl. Phys.* **44**, 3729 (1973).
93. A. V. Gusev and V. N. Rudenko, *Zh. Eksp. Teor. Fiz.* **72**, 1217 (1977).
94. J. Hough, J. R. Pugh, W. A. Edelstein, and W. Martin, *J. Phys. E* **10**, 993 (1977).
95. J. N. Hollenhorst and R. P. Giffard, *J. Low Temp. Phys.* **39**, 477 (1980).
96. J. Kurkijärvi, *J. Low Temp. Phys.* **45**, 37 (1981).
97. H. Ahola, G. J. Ehnholm, S. T. Islander, and B. Rantala, XXth Congress Ampere, Tallinn (1978).
98. A. Hoffman and B. Buchholz, *J. Phys. E* **17**, 1035 (1984).
99. H. Seppä, P. Immonen, and J. Räihä, *IEEE Trans. Instrum. Meas.* **IM-37**, 2 (1988).
100. A. P. Long, T. D. Clark, and R. J. Prance, *Rev. Sci. Instrum.* **51**, 8 (1980).
101. R. J. Prance, A. P. Long, T. D. Clark, and F. Goodall, *J. Phys. E* **15**, 101 (1982).
102. R. Keränen and J. Kurkijärvi, *J. Low Temp. Phys.* **65**, 279 (1986).
103. R. A. Kamper and M. B. Simmonds, *Appl. Phys. Lett.* **20**, 270 (1972).
104. J. M. Pierce, J. E. Opfer, and L. H. Rorden, *IEEE Trans. Magn.* **MAG-11**, 599 (1975).
105. H. Kanter and F. L. Vernon, Jr., *IEEE Trans. Magn.* **MAG-13**, 389 (1977).
106. J. N. Hollenhorst and R. P. Giffard, *IEEE Trans. Magn.* **MAG-15**, 474 (1979).
107. A. P. Long, T. D. Clark, R. J. Prance, and M. G. Richards, *Rev. Sci. Instrum.* **50**, 1376 (1979).
108. F. J. Rachford and J. Cukauskas, *Appl. Phys. Lett.* **35**, 881 (1979).
109. H. Seppä, *IEEE Trans. Instrum. Meas.* **32**, 253 (1983).
110. O. G. Vendik, Yu. N. Gorin, and M. G. Stepanova, *Pis'ma Zh. Tekh. Fiz.* **9**, 1007 (1983).
111. L. S. Kuzmin, K. K. Likharev, V. V. Migulin, E. A. Polunin, and N. A. Simonov, in *SQUID '85, Superconducting Quantum Interference Devices and Their Applications*, H. D. Hahlbohm and H. Lübbig, eds. (Walter de Gruyter, Berlin, 1985), p. 1029.
112. A. D. Smith, R. W. Simon, J. F. Durch, R. D. Sandell, and A. H. Silver, *IEEE Trans. Magn.* **MAG-23** 1079 (1987).
113. T. Ryhänen and H. Seppä, *IEEE Trans. Magn.* **MAG-25**, 881 (1989).
114. H. K. Olsson and T. Claeson, *J. Appl. Phys.* **64**, 5234 (1988).
115. R. A. Kamper, C. A. Simmonds, C. A. Hoer and R. T. Adain, *Proc. IEEE* **61**, 121 (1973).
116. B. W. Petley, K. Morris, R. W. Yell, and R. N. Clarke, *Electron. Lett.* **12**, 237 (1976).
117. D. B. Sullivan, R. T. Adain, and N. V. Frederick, *Proc. IEEE* **66**, 454 (1978).
118. R. A. Kamper and J. E. Zimmerman, *J. Appl. Phys.* **42**, 132 (1971).
119. R. J. Soulen, Jr. and H. Marshak, *Cryogenics* **7**, 408 (1980).
120. R. J. Soulen, Jr., R. L. Rusby, and D. Van Vechten, *J. Low Temp. Phys.* **40**, 553 (1980).
121. J. G. Park and A. Vaidya, *IEEE Trans. Magn.* **MAG-17**, 845 (1981).
122. A. H. Silver, R. D. Sandell, and J. Z. Wilcox, *IEEE Trans. Magn.* **MAG-19**, 625 (1983).
123. H. Seppä, *J. Appl. Phys.* **55**, 1572 (1984).
124. S. N. Erné and H. Luther, *PTB-Mitteilungen* **94**, 989 (1984).

125. M. Van Veldhuizen and H. A. Fowler, *Phys. Rev. B* **31**, 5805 (1985).
126. R. L. Peterson, *J. Appl. Phys.* **52**, 7321 (1981).
127. K. K. Likharev and V. K. Semenov, *Zh. Eksp. Teor. Fiz.* **15**, 625 (1972), *JETP Lett.* **15**, 442 (1972).
128. R. P. Giffard, P. F. Michelson, and R. J. Soulen, Jr., *IEEE Trans. Magn.* **MAG-15**, 276 (1979).
129. R. J. Soulen, Jr., D. Van Vechten, and H. Seppä, *Rev. Sci. Instrum.* **53**, 1355 (1982).
130. H. Seppä, *J. Low Temp. Phys.* **62**, 329 (1986).
131. R. A. Webb, R. P. Giffard, and J. C. Wheatley, *J. Low Temp. Phys.* **13**, 383 (1973).
132. M. L. Roukes, R. S. Germain, M. R. Freeman, and R. C. Richardson, in *Proceedings of the 17th International Conference on Low Temperature Physics LT-17*, U. Eckern, A. Schmid, W. Weber, and H. Wühl, eds. (North-Holland, Amsterdam, 1984), p. 1177.
133. S. N. Erné, H. Koch, and H. Luther, in *SQUID '85, Superconducting Quantum Interference Devices and Their Applications*, H. D. Hahlbohm and H. Lübbig, eds. (Walter de Gruyter, Berlin, 1985), p. 165.
134. J. E. Zimmerman and A. H. Silver, *Phys. Rev.* **141**, 367 (1966).
135. J. Clarke and T. A. Fulton, *J. Appl. Phys.* **40**, 4470 (1969).
136. J. Clarke, *IEEE Trans. Electron Dev.* **ED-27**, 1896 (1980).
137. J. M. Jaycox and M. B. Ketchen, *IEEE Trans. Magn.* **MAG-17**, 400 (1981).
138. M. B. Ketchen, *IEEE Trans. Magn.* **MAG-17**, 387 (1981).
139. M. B. Ketchen, W. M. Goubau, J. Clarke, and G. B. Donaldson, *J. Appl. Phys.* **49**, 4111 (1978).
140. M. B. Ketchen and J. M. Jaycox, *Appl. Phys. Lett.* **40**, 736 (1982).
141. C. D. Tesche, *J. Low Temp. Phys.* **47**, 385 (1982).
142. P. Carelli and V. Foglietti, *J. Appl. Phys.* **53**, 7592 (1982).
143. B. Muhlfelder, J. A. Beall, M. W. Cromar, R. H. Ono, and W. W. Johnson, *IEEE Trans. Magn.* **MAG-21**, 427 (1985).
144. K. Enpuku, K. Sueoka, K. Yoshida, and F. Irie, *J. Appl. Phys.* **57**, 1691 (1985).
145. V. J. de Waal and T. M. Klapwijk, *Appl. Phys. Lett.* **41**, 669 (1982).
146. J. Knuutila, A. Ahonen, and C. Tesche, *J. Low Temp. Phys.* **68**, 269 (1987).
147. D. Drung and W. Jutzi, in *SQUID '85, Superconducting Quantum Interference Devices and Their Applications*, H. D. Hahlbohm and H. Lübbig, eds. (Walter de Gruyter, Berlin, 1985), p. 807.
148. H. Seppä and T. Ryhänen, *IEEE Trans. Magn.* **MAG-23**, 1083 (1987).
149. E. Ben-Jacob and Y. Imry, *J. Appl. Phys.* **52**, 6806 (1981).
150. J. A. Ketoja, J. Kurkijärvi, and R. K. Ritala, *Phys. Rev. B* **30**, 3757 (1984).
151. J. A. Ketoja, J. Kurkijärvi, T. Ryhänen, and H. Seppä, *Phys. Rev. B* **35**, 404 (1987).
152. A. Th. A. M. de Waele and R. de Bruyn Ouboter, *Physica* **41**, 225 (1968).
153. R. L. Peterson and D. G. McDonald, *J. Appl. Phys.* **54**, 992 (1983).
154. C. Hilbert and J. Clarke, *J. Low Temp. Phys.* **61**, 237 (1985).
155. A. D. Wentzell and M. I. Freidlin, *Russian Math. Surveys* **25**, 1 (1970).
156. M. I. Freidlin and A. D. Wentzell, *Random Perturbations of Dynamical Systems* (Springer, New York, 1984).
157. E. Ben-Jacob, D. J. Bergman, Y. Imry, B. J. Matkowsky, and Z. Schuss, *J. Appl. Phys.* **54**, 6533 (1983).
158. E. Ben-Jacob, D. J. Bergman, B. J. Matkowsky, and Z. Schuss, in *SQUID '85, Superconducting Quantum Interference Devices and Their Applications*, H. D. Hahlbohm and H. Lübbig, eds. (Walter de Gruyter, Berlin, 1985), p. 219.
159. J. Kurkijärvi, in *SQUID '85, Superconducting Quantum Interference Devices and Their Applications*, H. D. Hahlbohm and H. Lübbig, eds. (Walter de Gruyter, Berlin, 1985), p. 377.
160. I. O. Kulik, *Zh. Eksp. Teor. Fiz.* **37**, 157 (1967).
161. Y. Imry and P. M. Marcus, *IEEE Trans. Magn.* **MAG-13**, 868 (1977).
162. J. J. P. Bruines, V. J. de Waal, and J. E. Mooij, *J. Low Temp. Phys.* **46**, 383 (1982).
163. V. J. de Waal, P. Schrijner, and R. Llurba, *J. Low Temp. Phys.* **54**, 215 (1984).
164. R. Leoni, P. Carelli, and V. Foglietti, *Phys. Rev. B* **35**, 400 (1987).
165. S. Chandrasekhar, *Rev. Mod. Phys.* **15**, 1 (1943).

166. H. Risken and H. D. Vollmer, *Phys. Lett.* **69A**, 387 (1979).
167. H. D. Vollmer and H. Risken, *Z. Phys. B* **34**, 313 (1979).
168. Y. Imry and L. S. Schulman, *J. Appl. Phys.* **49**, 749 (1978).
169. E. Ben-Jacob, D. J. Bergman, Z. Schuss, *Phys. Rev. B* **25**, 519 (1982).
170. C. D. Tesche, *J. Low Temp. Phys.* **44**, 119 (1981).
171. H. Risken, *The Fokker-Planck Equation* (Springer-Verlag, New York, 1984).
172. Z. Schuss, *SIAM J. Review* **22**, 119 (1980).
173. H. Suhl, *Phys. Rev. Lett.* **60**, 473 (1988).
174. F. Sharifi, J. L. Gavilano, and D. J. van Harlingen, *Phys. Rev. Lett.* **61**, 742 (1988).
175. C. Grebogi, E. Ott, and J. A. Yorke, *Phys. Rev. Lett.* **50**, 935 (1983).
176. J. Guckenheimer and P. Holmes, *Nonlinear Oscillations, Dynamical Systems, and Bifurcations of Vector Fields* (Springer-Verlag, New York, 1983).
177. A. J. Lichtenberg and M. A. Lieberman, *Regular and Stochastic Motion* (Springer-Verlag, New York, 1983).
178. E. Ben-Jacob, D. J. Bergman, B. J. Matkowsky and Z. Schuss, *Phys. Rev. A* **26**, 2805 (1982).
179. M. R. Beasley, D. D'Humieres and B. A. Huberman, *Phys. Rev. Lett.* **50**, 1328 (1983).
180. R. L. Kautz, *J. Appl. Phys.* **58**, 424 (1985).
181. R. L. Kautz, *Phys. Lett.* **125A**, 315 (1987).
182. R. L. Kautz, *Phys. Rev. A* **38**, 2066 (1988).
183. J. E. Zimmerman, *J. Appl. Phys.* **42**, 4483 (1971).
184. M. S. Gupta, *Phys. Rev. A* **18**, 2725 (1978).
185. M. S. Gupta, *Proc. IEEE* **70**, 788 (1982).
186. Y. Netzer, *Proc. IEEE* **62**, 404 (1974).
187. Y. Netzer, *Proc. IEEE* **69**, 728 (1981).
188. J. H. Claassen, *J. Appl. Phys.* **46**, 2268 (1975).
189. J. Knuutila, M. Kajola, H. Seppä, R. Mutikainen, and J. Salmi, *J. Low Temp. Phys.* **71**, 369 (1988).
190. R. F. Voss, R. B. Laibowitz, A. N. Broers, S. I. Raider, C. M. Knoedler, and J. M. Viggiano, *IEEE Trans. Magn.* **MAG-17**, 395 (1981).
191. M. W. Cromar and P. Carelli, *Appl. Phys. Lett.* **38**, 723 (1981).
192. R. H. Koch, D. J. Van Harlingen, and J. Clarke, *Appl. Phys. Lett.* **38**, 380 (1981).
193. D. J. Van Harlingen, R. H. Koch, and J. Clarke, *Appl. Phys. Lett.* **41**, 197 (1982).
194. R. T. Wakai and D. J. Van Harlingen, *Appl. Phys. Lett.* **49**, 593 (1986).
195. C. D. Tesche, K. H. Brown, A. C. Callegari, M. M. Chen, J. H. Greiner, H. C. Jones, M. B. Ketchen, K. K. Kim, A. W. Kleinsasser, H. A. Notarys, G. Proto, R. H. Wang, and T. Yogi, *IEEE Trans. Magn.* **MAG-21**, 1032 (1985).
196. G. D. Vendelin, *Microwave Journal* **13**, 63 (1970).
197. J. R. James and A. Henderson, *IEEE Journal on Microwaves, Optics and Acoustics* **3**, 205 (1979).
198. A. Longacre, Jr., *J. Appl. Phys.* **50**, 6451 (1979).
199. C. Hilbert and J. Clarke, *J. Low Temp. Phys.* **61**, 263 (1985).
200. R. S. Germain, M. L. Roukes, M. R. Freeman, R. C. Richardson, and M. B. Ketchen, in *Proceedings of the 17th International Conference on Low Temperature Physics LT-17*, U. Eckern, A. Schmid, W. Weber, and H. Wühl, eds. (North-Holland, Amsterdam, 1984), p. 203.
201. J. M. Martinis and J. Clarke, *J. Low Temp. Phys.* **65**, 459 (1986).
202. T. Ryhänen and H. Seppä, (1989), to be published.
203. R. Ilmoniemi, R. Hari, and K. Reinikainen, *Electroenceph. Clin. Neurophysiol.* **58**, 467 (1984).
204. H. J. Paik, R. H. Mathews, and M. G. Castellano, *IEEE Trans. Magn.* **MAG-17**, 404 (1981).
205. K. Enpuku, T. Muta, K. Yoshida, and F. Irie, *J. Appl. Phys.* **58**, 1916 (1985).
206. K. Enpuku and K. Yoshida, *J. Appl. Phys.* **59**, 1714 (1986).
207. K. Enpuku, K. Yoshida, and S. Kohjiro, *J. Appl. Phys.* **60**, 4218 (1986).
208. H. Koch, in *SQUID '85, Superconducting Quantum Interference Devices and Their Applications*, H. D. Hahlbohm and H. Lübbig, eds. (Walter de Gruyter, Berlin, 1985), p. 773.
209. P. Carelli and V. Foglietti, *IEEE Trans. Magn.* **MAG-19**, 299 (1983).
210. P. Carelli and V. Foglietti, *IEEE Trans. Magn.* **MAG-21**, 424 (1985).

211. B. Muhlfelder, W. Johnson, and M. W. Cromar, *IEEE Trans. Magn.* **MAG-19**, 303 (1983).
212. R. F. Broom, S. I. Raider, A. Oosenbrug, R. E. Drake, and W. Walter, *IEEE Trans. Electron Dev.* **ED-27**, 1998 (1980).
213. S. I. Raider, *IEEE Trans. Magn.* **MAG-21**, 110 (1985).
214. G. Hawkins and J. Clarke, *J. Appl. Phys.* **47**, 1616 (1976).
215. E. E. Latta and M. Gasser, *J. Appl. Phys.* **54**, 1115 (1983).
216. R. J. P. Bain and G. B. Donaldson, *IEEE Trans. Magn.* **MAG-21**, 543 (1985).
217. A. I. Braginski, in *Extended Abstracts of the 1987 International Superconductivity Electronics Conference ISEC'87* (Japan Society of Applied Physics, Tokyo, 1987), p. 63.
218. M. K. Wu, J. R. Ashburn, C. J. Torng, P. H. Hor, R. L. Meng, L. Gao, Z. J. Huang, Y. Q. Wang, and C. W. Chu, *Phys. Rev. Lett.* **58**, 908 (1987).
219. H. Maeda, Y. Tanaka, M. Fukutomi, and T. Asano, *Jpn. J. Appl. Phys.* **27**, L209 (1988).
220. S. S. P. Parkin, V. Y. Lee, E. M. Engler, A. I. Nazzal, T. C. Huang, G. Gornam, R. Savoy, and R. Beyers, *Phys. Rev. Lett.* **60**, 2539 (1988).
221. C. C. Torardi, M. A. Subramanian, J. C. Calabrese, J. Gopalakrishnan, K. J. Morrissey, T. R. Flippen, U. Chowdhry, and A. W. Sleight, *Science* **240**, 631 (1988).
222. D. Estève, J. M. Martinis, C. Urbina, M. H. Devoret, G. Collin, P. Monod, M. Ribault, and A. Revcolevschi, *Europhys. Lett.* **3**, 1237 (1987).
223. A. Inoue, K. Takeuchi, H. Ito, A. Nakayama, and S. Naito, *Jpn. J. Appl. Phys.* **26**, L1211 (1987).
224. Y. Higashino, T. Takahashi, T. Kawai, and S. Naito, *Jpn. J. Appl. Phys.* **26**, L1211 (1987).
225. H. Tanabe, S. Kita, and T. Kobayashi, in *Extended Abstracts of the 1987 International Superconductivity Electronics Conference ISEC '87* (Japan Society of Applied Physics, Tokyo, 1987), p. 397.
226. P. H. Wu, Q. H. Cheng, S. Z. Yang, J. Chen, Y. Li, Z. M. Ji, J. M. Song, H. X. Lu, X. K. Gao, J. Wu, and X. Y. Zhang, in *Extended Abstracts of the 1987 International Superconductivity Electronics Conference ISEC '87* (Japan Society of Applied Physics, Tokyo, 1987), p. 392.
227. M. Murakami, E. Alessandrini, and K. Kim, *J. Appl. Phys.* **56**, 2068 (1984).
228. M. Murakami, E. Alessandrini, and K. Kim, *J. Appl. Phys.* **56**, 2076 (1984).
229. H. Yamada and A. Ishida, *J. Vac. Sci. Technol.* **16**, 875 (1979).
230. S. Kosaka, A. Shoji, M. Ayoagi, Y. Sakamoto, F. Shinoki, and H. Hayakawa, *IEEE Trans. Magn.* **MAG-23**, 1389 (1987).
231. S. A. Reible, *IEEE Trans. Magn.* **MAG-17**, 303 (1981).
232. M. Chen and R. Wang, *J. Vac. Sci. Technol.* **A1**, 708 (1983).
233. R. E. Lee, *J. Vac. Sci. Technol.* **16**, 164 (1979).
234. M. Gurvitch, M. A. Washington, and H. A. Huggins, *Appl. Phys. Lett.* **42**, 472 (1983).
235. A. Shoji, F. Shinoki, S. Kosaka, M. Ayoagi, and H. Hayakawa, *Appl. Phys. Lett.* **41**, 1097 (1982).
236. S. Morohashi, S. Hasuo, and T. Yamaoka, *Appl. Phys. Lett.* **48**, 254 (1986).
237. H. Kroger, L. Smith, and D. Jillie, *Appl. Phys. Lett.* **39**, 280 (1981).
238. J. C. Villegier, L. Vieux-Rochaz, M. Goniche, P. Renard, and M. Vabre, *IEEE Trans. Magn.* **MAG-21**, 498 (1985).
239. M. Yuda, K. Kuroda, and J. Nakano, *Jpn. J. Appl. Phys.* **26**, L166 (1987).
240. L. Yu, C. Berry, R. Drake, K. Li, R. Patt, M. Radparvar, S. Whiteley, and S. Faris, *IEEE Trans. Magn.* **MAG-23**, 1476 (1987).
241. J. H. Magerlein, *IEEE Trans. Magn.* **MAG-17**, 286 (1981).
242. L. Young, *Anodic Oxide Films* (Academic Press, New York, 1971).
243. R. F. Broom, A. Oosenbrug, and W. Walter, *Appl. Phys. Lett.* **37**, 237 (1980).
244. A. W. Kleinsasser and R. A. Buhrman, *Appl. Phys. Lett.* **37**, 841 (1980).
245. A. Tugwell, C. M. Pegrum, G. B. Donaldson, and M. Wicks, *IEEE Trans. Magn.* **MAG-23**, 676 (1987).
246. H. Koch, in *Extended Abstracts of the 1987 International Superconductivity Electronics Conference ISEC '87* (Japan Society of Applied Physics, Tokyo, 1987), p. 281.
247. I. Ishida, S. Tahara, and Y. Wada, *Appl. Phys. Lett.* **53**, 316 (1988).
248. S. Nagasawa, H. Tsuge, and Y. Wada, *IEEE Electron. Dev. Lett.* **9**, 414 (1988).

249. P. Chaudhari, J. Mannhart, D. Dimos, C. C. Tsuei, J. Chi, M. M. Oprysko, and M. Scheuermann, *Phys. Rev. Lett.* **60**, 1653 (1988).
250. J. H. Greiner, *J. Appl. Phys.* **42**, 5151 (1971).
251. W. Schroen, *J. Appl. Phys.* **39**, 2671 (1968).
252. J. Salmi, J. Knuutila, H. Seppä, and P. Immonen, *Thin Solid Films* **126**, 77 (1985).
253. R. Herwig, in Proceedings of the 17th International Conference on Low Temperature Physics, U. Eckern, A. Schmid, W. Weber, and H. Wühl, Eds. (North-Holland, Amsterdam, 1984), p. 209.
254. S. S. Pei and R. B. van Dover, *Appl. Phys. Lett.* **44**, 703 (1984).
255. A. W. Kleinsasser, *J. Appl. Phys.* **57**, 2575 (1985).
256. J. Salmi, J. Knuutila, and R. Mutikainen, in *Erosion and Growth of Solids Stimulated by Atom and Ion Beams*, G. Kiriaikidis, G. Carter, and J. L. Whitton, eds. (Martinus Nijhoff Publishers, Dordrecht, 1986), p. 366.
257. J. C. Villegier and G. Matheron, in *SQUID '80, Superconducting Quantum Interference Devices and Their Applications*, H. D. Hahlbohm and H. Lübbig, eds. (Walter de Gruyter, Berlin, 1980), p. 381.
258. W. J. Gallagher, S. I. Raider, and R. E. Drake, *IEEE Trans. Magn.* **MAG-19**, 807 (1983).
259. S. I. Raider and R. E. Drake, *IEEE Trans. Magn.* **MAG-17**, 299 (1981).
260. S. I. Raider, R. W. Johnson, T. S. Kuan, R. E. Drake, and R. A. Pollak, *IEEE Trans. Magn.* **MAG-19**, 803 (1983).
261. T. S. Kuan, S. I. Raider, and R. E. Drake, *J. Appl. Phys.* **53**, 7464 (1982).
262. T. Imamura, H. Hoko, and S. Hasuo, in *Extended Abstracts of the 1987 International Superconductivity Electronics Conference ISEC '87* (Japan Society of Applied Physics, Tokyo, 1987), p. 57.
263. A. Nakayama, A. Inoue, and Y. Okabe, in *Extended Abstracts of the 1987 International Superconductivity Electronics Conference ISEC '87* (Japan Society of Applied Physics, Tokyo, 1987), p. 301.
264. J. M. Rowell, M. Gurvitch, and J. Geerk, *Phys. Rev. B* **24**, 2278 (1981).
265. J. Talvacchio, J. R. Gavaler, A. I. Braginski, and M. A. Janocko, *J. Appl. Phys.* **58**, 4638 (1985).
266. J. Talvacchio and A. I. Braginski, in *Extended Abstracts of the 1987 International Superconductivity Electronics Conference ISEC '87* (Japan Society of Applied Physics, Tokyo, 1987), p. 309.
267. H. Asano, K. Tanabe, O. Michikami, M. Igarashi, and M. Beasley, *Jpn. J. Appl. Phys.* **24**, 289 (1985).
268. A. Shoji, M. Aoyagi, S. Kosaka, F. Shinoki, and H. Hayakawa, *Appl. Phys. Lett.* **46**, 1098 (1985).
269. J. B. Barner and S. T. Ruggiero, *IEEE Trans. Magn.* **MAG-23**, 854 (1987).
270. M. Radparvar, M. Berry, R. Drake, S. Faris, S. Whiteley, and L. Yu, *IEEE Trans. Magn.* **MAG-23**, 1480 (1987).
271. J. Talvacchio and A. I. Braginski, *IEEE Trans. Magn.* **MAG-23**, 859 (1987).
272. E. J. Cukauskas, M. Nisenoff, D. W. Jillie, H. Kroger, and L. N. Smith, *IEEE Trans. Magn.* **MAG-19**, 831 (1983).
273. E. J. Cukauskas, W. L. Carter, and M. Nisenoff, in *Extended Abstracts of the 1987 International Superconductivity Electronics Conference ISEC '87* (Japan Society of Applied Physics, Tokyo, 1987), p. 314.
274. C. T. Rogers, R. A. Buhrman, W. J. Gallagher, S. Raider, A. W. Kleinsasser, and R. L. Sandstrom, *IEEE Trans. Magn.* **MAG-23**, 1658 (1987).
275. B. Savo, F. C. Wellstood, and J. Clarke, *Appl. Phys. Lett.* **50**, 1757 (1987).
276. R. H. Koch, C. P. Umbach, G. J. Clark, P. Chaudhari, and R. B. Laibowitz, *Appl. Phys. Lett.* **51**, 200 (1987).
277. H. Nakane, T. Nishino, M. Hirano, K. Takagi, and U. Kawabe, in *Extended Abstracts of the 1987 International Superconductivity Electronics Conference ISEC '87* (Japan Society of Applied Physics, Tokyo, 1987), p. 411.
278. I. Iguchi, A. Sugishita, and M. Yanagisawa, *Jpn. J. Appl. Phys.* **26**, L1021 (1987).
279. J. E. Zimmerman, J. A. Beall, M. W. Cromar, and R. H. Ono, *Appl. Phys. Lett.* **51**, 617 (1987).

280. C. M. Pegrum, G. B. Donaldson, A. H. Carr, and A. Hendry, *Appl. Phys. Lett.* **51**, 1364 (1987).
281. R. H. Koch and A. P. Malozemoff, in *Proceedings of a Conference on High Performance SQUID Systems* (Stanford University, Stanford, 1988).
282. R. H. Koch, C. P. Umbach, M. M. Oprysko, J. D. Mannhart, B. Bumble, G. J. Clark, W. J. Gallagher, A. Gupta, A. Kleinsasser, R. B. Laibowitz, R. B. Sandstrom, and M. R. Scheuermann, *Physica C* **153–155**, 1685 (1988).
283. M. J. Ferrari, M. Johnson, F. C. Wellstood, J. Clarke, P. A. Rosenthal, R. H. Hammond, and M. R. Beasley, *Appl. Phys. Lett.* **53**, 695 (1988).
284. R. L. Sandstrom, W. J. Gallagher, T. R. Dinger, R. H. Koch, R. B. Laibowitz, A. W. Kleinsasser, R. J. Gambino, B. Bumble, and M. F. Chisholm, *Appl. Phys. Lett.* **53**, 444 (1988).
285. R. H. Koch and P. Chaudhari, *Nature* **332**, 682 (1988).
286. J. Clarke and R. H. Koch, *Science* **242**, 217 (1988).
287. E. Tjukanov, R. W. Cline, R. Krahn, M. Hayden, M. W. Reynolds, W. N. Hardy, J. F. Carolan, and R. C. Thompson, *Phys. Rev. B* **36**, 7244 (1987).
288. J. C. Gallop, C. D. Langham, W. J. Radcliffe, and W. B. Roys, *Phys. Lett.* **128A**, 222 (1988).
289. Y. Yeshurun and A. P. Malozemoff, *Phys. Rev. Lett.* **60**, 2202 (1988).
290. M. J. Ferrari, M. Johnson, F. C. Wellstood, J. Clarke, P. A. Rosenthal, R. H. Hammond, and M. R. Beasley, *IEEE Trans. Magn.* **MAG-25**, 806 (1989).
291. P. Rosenthal, R. H. Hammond, M. R. Beasley, R. Leoni, Ph. Lerch, and J. Clarke, *IEEE Trans. Magn.* **MAG-25**, 973 (1989).
292. J. Mannhart, P. Chaudhari, D. Dimos, C. C. Tsuei, and T. R. McGuire, *Phys. Rev. Lett.* **61**, 2476 (1988).
293. P. W. Anderson, *Phys. Rev. Lett.* **9**, 309 (1962).
294. Y. B. Kim, *Rev. Mod. Phys.* **36**, 39 (1964).
295. M. Tinkham, *Helv. Phys. Acta* **61**, 443 (1988).
296. J. Kuzník, M. Odehnal, S. Šafrata and J. Endal, *J. Low Temp. Phys.* **69**, 313 (1987).
297. R. Tichý, M. Odehnal, V. Petříček, S. Šafrata, E. Pollert, J. Kamarád, J. Hejtmánek, O. Smrková, and D. Sýkorová, *J. Low Temp. Phys.* **70**, 187 (1988).
298. N. García, S. Vieira, A. M. Baro, J. Tornero, M. Pazos, L. Vázquez, J. Gómez, A. Aguiló, S. Bourgeal, A. Buendía, M. Hortal, M. A. López de la Torre, M. A. Ramos, R. Villar, K. V. Rao, D.-X. Chen, J. Nogues, and N. Karpe, *Z. Phys. B* **70**, 9 (1988).
299. R. L. Forgacs and A. Warnick, *IEEE Trans. Instrum. Meas.* **IM-15**, 113 (1966).
300. R. L. Forgacs and A. Warnick, *Rev. Sci. Instrum.* **38**, 214 (1967).
301. R. P. Giffard, in *SQUID '80, Superconducting Quantum Interference Devices and Their Applications*, H. D. Hahlbohm and H. Lübbig, eds. (Walter de Gruyter, Berlin, 1980), p. 445.
302. C. Rillo, D. Veldhuis, and J. Flokstra, *IEEE Trans. Instrum. Meas.* **IM-36**, 770 (1987).
303. G. J. Ehnholm, J. P. Ekström, M. T. Loponen, and J. K. Soini, *Cryogenics* **19**, 673 (1979).
304. K. H. G. Duh, M. W. Pospieszalski, W. F. Kopp, P. Ho, A. A. Jabra, P.-C. Chao, P. M. Smith, L. F. Lester, J. M. Ballingall, and S. Weinreb, *IEEE Trans. Electron Dev.* **ED-35**, 249 (1988).
305. M. W. Pospieszalski, S. Weinreb, R. D. Norrod, and R. Harris, *IEEE Trans. Microwave Theory Tech.* **MMT-36**, 552 (1988).
306. J. Clarke, W. M. Goubau, and M. B. Ketchen, *Appl. Phys. Lett.* **27**, 155 (1975).
307. V. V. Danilov, K. K. Likharev, D. V. Snigiriev, and E. S. Soldatov, *IEEE Trans. Magn.* **MAG-13**, 240 (1977).
308. F. C. Wellstood, C. Heiden, and J. Clarke, *Rev. Sci. Instrum.* **55**, 952 (1984).
309. Biomagnetic Technologies, Inc., 4174 Sorrento Valley Boulevard, San Diego, CA 92121.
310. R. H. Koch, J. Clarke, W. M. Goubau, J. M. Martinis, C. M. Pegrum, and D. J. Van Harlingen, *J. Low Temp. Phys.* **51**, 207 (1983).
311. V. Foglietti, W. J. Gallagher, M. B. Ketchen, A. W. Kleinsasser, R. H. Koch, S. I. Raider, and R. L. Sandstrom, *Appl. Phys. Lett.* **49**, 1393 (1986).
312. D. Drung, E. Crocoll, R. Herwig, M. Neuhaus, and W. Jutzi, *IEEE Trans. Magn.* **MAG-25**, 1034 (1989).

313. H. Furukawa, M. Katayama, H. Emoto, and K. Shirae, in *Proceedings of the 6th Sensor Symposium*, S. Kataoka, ed. (Institute of Electrical Engineers of Japan, Tsukuba, 1986), p. 319.
314. K. Shirae, H. Furukawa, M. Katayama, and T. Katayama, in *Biomagnetism '87*, K. Atsumi, M. Kotani, S. Ueno, T. Katila, and S. J. Williamson, eds. (Tokyo Denki University Press, Tokyo, 1987).
315. D. Drung, *Cryogenics* **26**, 623 (1986).
316. N. Fujimaki, H. Tamura, T. Imamura, and S. Hasuo, *IEEE Trans. Electron Dev.* **ED-35**, 2412 (1988).
317. A. Widom, *J. Low Temp. Phys.* **37**, 449 (1979).
318. A. Widom, T. D. Clark, and G. Megaloudis, *Phys. Lett.* **76A**, 163 (1980).
319. R. F. Voss, *Appl. Phys. Lett.* **38**, 182 (1981).
320. T. A. Fulton and L. N. Dunkleberger, *Phys. Rev. B* **9**, 4760 (1974).
321. P. Dutta and P. M. Horn, *Rev. Mod. Phys.* **53**, 497 (1981).
322. M. B. Weissman, *Rev. Mod. Phys.* **60**, 537 (1988).
323. R. H. Koch, J. Clarke, J. M. Martinis, W. M. Goubau, C. M. Pegrum, and D. J. Van Harlingen, *IEEE Trans. Magn.* **MAG-19**, 449 (1983).
324. R. H. Koch, in *Noise in Physical Systems and 1/f Noise*, M. Savelli, G. Lecoy, and J.-P. Nougier, eds., (Elsevier, New York, 1983), p. 377.
325. C. T. Rogers and R. A. Buhrman, *IEEE Trans. Magn.* **MAG-21**, 126 (1985).
326. C. T. Rogers and R. A. Buhrman, *Phys. Rev. Lett.* **55**, 859 (1985).
327. J. Bernamont, *Ann. Phys. (Leipzig)* **7**, 71 (1937).
328. A. L. McWhorter, in *Semiconductor Surface Physics*, R. H. Kingston, ed., (University of Pennsylvania Press, Philadelphia, 1957), p. 207.
329. P. Dutta, P. Dimon, and P. M. Horn, *Phys. Rev. Lett.* **43**, 646 (1979).
330. R. F. Voss and J. Clarke, *Phys. Rev. B* **13**, 556 (1976).
331. H. Seppä, T. Ryhänen, and J. Kurkijärvi, *Phys. Rev. B*, to be published.
332. S. Hashiguchi, in *Proceedings of the Ninth International Conference on Noise in Physical Systems*, C. M. Van Vliet, ed. (World Scientific, Toronto, 1987), p. 315.
333. K. Atsumi, M. Kotani, S. Ueno, T. Katila, and S. J. Williamson, eds., *Biomagnetism '87* (Tokyo Denki University Press, Tokyo, 1988).
334. S. J. Williamson, G. L. Romani, L. Kaufman, and I. Modena, eds., *Biomagnetism: An Interdisciplinary Approach*, Vol. 66 of *NATO Advanced Science Institutes Series. Series A: Life Sciences* (Plenum, New York, 1983).
335. D. Cohen, *Science* **180**, 745 (1973).
336. D. N. Paulson, R. Toussaint, R. L. Fagaly, and S. E. Robinson, *IEEE Trans. Magn.* **MAG-23**, 1315 (1987).
337. R. J. Ilmoniemi, S. J. Williamson, and W. E. Hostetler, in K. Atsumi, M. Kotani, S. Ueno, T. Katila, and S. J. Williamson, eds., *Biomagnetism '87*, (Tokyo Denki University Press, Tokyo, 1988), p. 182.
338. K. Kalliomäki, P.-L. Kalliomäki, K. Aittoniemi, and M. Moilanen, in *Biomagnetism: An Interdisciplinary Approach* S. J. Williamson, G.-L. Romaini, L. Kaufman, and I. Modena, eds. (Plenum, New York, 1983), p. 545.
339. G. M. Brittenham, D. E. Farrell, J. W. Harris, E. S. Feldman, E. H. Danish, W. A. Muir, J. H. Tripp, and E. M. Bellon, *New Engl. J. Med.* **307**, 1671 (1982).
340. R. Hari and R. J. Ilmoniemi, *CRC Critical Rev. in Biomed. Eng.* **14**, 93 (1986).
341. G.-L. Romani and L. Narici, *Med. Progr. Technol.* **11**, 123 (1986).
342. S. J. Williamson, L. Kaufman, and D. Brenner, *J. Appl. Phys.* **50**, 2418 (1979).
343. D. Cohen, *Science* **175**, 664 (1972).
344. J. Knuutila, S. Ahlfors, A. Ahonen, J. Hällström, M. Kajola, O. V. Lounasmaa, V. Vilkman, and C. Tesche, *Rev. Sci. Instrum.* **58**, 2145 (1987).
345. S.-L. Joutsiniemi, *Acta Neurol. Scand.* **78**, 337 (1989).
346. S. N. Erné, *Med. Biol. Eng. Comput.* **23 (S2)**, 1447 (1985).
347. T. Katila, R. Maniewski, M. Mäkipää, J. Nenonen, and P. Siltanen, *Phys. Med. Biol.* **32**, 125 (1987).
348. B. M. Horacek, *IEEE Trans. Magn.* **MAG-9**, 440 (1973).
349. B. N. Cuffin and D. B. Geselowitz, *IEEE Trans. Biomed. Eng.* **BME-24**, 242 (1977).

350. W. T. Miller, III and D. B. Geselowitz, *Circulation Res.* **43**, 301 (1978).
351. B. W. Petley, in *Quantum Metrology and Fundamental Physical Constants*, P. H. Cutler and A. A. Lucas, eds (Plenum, New York, 1983), p. 293.
352. A. Davidson, *Appl. Phys. Lett.* **38**, 721 (1981).
353. J. A. Rowlands and S. B. Woods, *Rev. Sci. Instrum.* **47**, 795 (1976).
354. D. J. Van Harlingen, D. F. Heidel, and J. C. Garland, *Phys. Rev. B* **21**, 1842 (1980).
355. G. Pickett, *Phys. Rev. Lett.* **47**, 134 (1981).
356. J.-S. Tsai, A. K. Jain, and J. E. Lukens, *Phys. Rev. Lett.* **51**, 316 (1983).
357. D. B. Sullivan, *Rev. Sci. Instrum.* **43**, 499 (1972).
358. I. K. Harvey, *Metrologia* **12**, 47 (1976).
359. R. F. Dziuba, B. F. Field, and T. F. Finnegan, *IEEE Trans. Instrum. Meas.* **IM-23**, 264 (1974).
360. V. Kose, F. Melcert, W. Engelland, H. Fack, B. Fuhrmann, P. Gutmann, and P. Warnecke, *IEEE Trans. Instrum. Meas.* **IM-23**, 271 (1974).
361. J. C. Gallop and B. W. Petley, *IEEE Trans. Instrum. Meas.* **IM-23**, 267 (1974).
362. D. Andreone, E. Arri, G. Boella, and G. C. Marullo, *IEEE Trans. Instrum. Meas.* **IM-25**, 512 (1976).
363. I. K. Harvey, *Rev. Sci. Instrum.* **43**, 1626 (1972).
364. I. K. Harvey and H. C. Collins, *Rev. Sci. Instrum.* **44**, 1700 (1973).
365. D. B. Sullivan and R. F. Dziuba, *Rev. Sci. Instrum.* **45**, 517 (1974).
366. K. Grohmann, H. D. Hahlbohm, H. Lübbig, and H. Ramin, *IEEE Trans. Instrum. Meas.* **IM-23**, 261 (1974).
367. K. von Klitzing, G. Dorda, and M. Pepper, *Phys. Rev. Lett.* **45**, 494 (1980).
368. F. Delahaye, *IEEE Trans. Instrum. Meas.* **IM-27**, 426 (1978).
369. H. Seppä, IEEE Cat. 80 CH 1497-7 IM, CPEM Dig., p. 172 (1980).
370. A. Hartland, in *Proceedings of the Precision Measurement and Fundamental Constants II*, Vol. 617 (National Bureau of Standards, Washington D.C., 1982), p. 543.
371. F. Delahaye and D. Reymann, *IEEE Trans. Instrum. Meas.* **IM-34**, 316 (1985).
372. K. Grohmann and D. Hechtfischer, *IEEE Trans. Instrum. Meas.* **IM-33**, 91 (1984).
373. K. Grohmann, D. Hechtfischer, and J. Jakschik, in *SQUID '76, Superconducting Quantum Interference Devices and Their Applications*, H. D. Hahlbohm and H. Lübbig, eds. (Walter de Gruyter, Berlin, 1977), p. 311.
374. S. N. Erné and H. Luther, *IEEE Trans. Instrum. Meas.* **IM-24**, 345 (1975).
375. K. Weyand, *IEEE Trans. Instrum. Meas.* **IM-29**, 324 (1980).
376. R. L. Kautz, *Appl. Phys. Lett.* **36**, 386 (1980).
377. R. L. Kautz and G. Costabile, *IEEE Trans. Magn.* **MAG-17**, 780 (1981).
378. J. Niemeyer, J. H. Hinken, and W. Meier, *IEEE Trans. Instrum. Meas.* **IM-33**, 311 (1984).
379. R. E. Harris and C. A. Hamilton, in *AIP Conference Proceedings*, Vol. 44, B. Deaver, ed. (1978), p. 448.
380. D. B. Sullivan and N. V. Frederick, *IEEE Trans. Magn.* **MAG-13**, 396 (1977).
381. J. C. Gallop, in *SQUID '76, Superconducting Quantum Interference Devices and Their Applications*, H. D. Hahlbohm and H. Lübbig, eds. (Walter de Gruyter, Berlin, 1977), p. 267.
382. J. C. Gallop, *J. Phys. B* **11**, L93 (1978).
383. F. Shiota and K. Hara, *IEEE Trans. Instrum. Meas.* **IM-36**, 271 (1987).
384. R. Meserve, *J. Appl. Phys.* **39**, 2598 (1968).
385. E. R. Williams and P. T. Olsen, *IEEE Trans. Instrum. Meas.* **IM-27**, 467 (1978).
386. B. N. Taylor, W. H. Parker, and D. N. Langenberger, *Rev. Mod. Phys.* **41**, 375 (1969).
387. B. Cabrera, S. Benjamin, and J. T. Anderson, *Physica* **107B**, 19 (1981).
388. S. B. Felch, B. Cabrera, J. Tate, and J. T. Anderson, in *Proceedings of the 17th International Conference on Low Temperature Physics LT-17*, U. Eckern, A. Schmid, W. Weber, and H. Wühl, eds. (North-Holland, Amsterdam, 1984), p. 923.
389. T. D. Gamble, W. M. Goubau, and J. Clarke, *Geophysics* **44**, 959 (1979).
390. M. Wilt, N. E. Goldstein, M. Stark, J. R. Haught, and H. F. Morrison, *Geophysics* **48**, 1090 (1983).
391. J. Clarke, *IEEE Trans. Magn.* **MAG-19**, 288 (1983).
392. P. V. Czipott, and W. N. Podney, *IEEE Trans. Magn.* **MAG-23**, 465 (1987).

393. Z. Janu, M. Odehnal, V. Petříček, and R. Tichý, in *SQUID '85, Superconducting Quantum Interference Devices and Their Applications*, H. D. Hahlbohm and H. Lübbig, eds. (Walter de Gruyter, Berlin, 1985), p. 885.
394. H. J. Paik, *J. Appl. Phys.* **47**, 1168 (1976).
395. H. J. Paik, E. R. Mapoles, and K. Y. Wang, in *Future Trends in Superconductive Electronics*, B. S. Deaver, Jr., C. M. Falco, J. H. Harris, and S. A. Wolf, eds. (American Institute of Physics, New York), 1978), p. 166.
396. A. B. Colquhoun, N. A. Lockerbie, and G. B. Donaldson, in *SQUID '85, Superconducting Quantum Interference Devices and Their Applications*, H. D. Hahlbohm and H. Lübbig, eds. (Walter de Gruyter, Berlin, 1985), p. 1191.
397. J. F. Kos, R. Barton, and B. Ramadan, *J. Appl. Phys.* **48**, 3193 (1977).
398. M. S. McAshan, W. M. Fairbank, P. F. Michelson, and R. C. Taber, *Physica* **107B**, 23 (1981).
399. E. Ikonen, P. Karp, T. Katila, and K. Riski, *J. Phys. E* **16**, 875 (1983).
400. J. F. Kos, *J. Appl. Phys.* **49**, 955 (1978).
401. C. Cosmelli, P. Carelli, M. G. Castellano, and V. Foglietti, *IEEE Trans. Magn.* **MAG-23**, 454 (1987).
402. B. Cabrera, *Phys. Rev. Lett.* **48**, 1378 (1982).
403. B. Cabrera, M. Taber, R. Gardner, and J. Bourg, *Phys. Rev. Lett.* **51**, 1933 (1983).
404. C. D. Tesche, C. C. Chi, C. C. Tsuei, and P. Chaudhari, *Appl. Phys. Lett.* **43**, 384 (1983).
405. J. Incandela, M. Campbell, H. Frisch, S. Somalwar, M. Kuchnir, and H. R. Gustafson, *Phys. Rev. Lett.* **53**, 2067 (1984).
406. C. C. Chi, C. D. Tesche, C. C. Tsuei, P. Chaudhari, and S. Bermon, in *Monopole '83*, J. L. Stone, ed. (Plenum, New York, 1984), p. 451.
407. S. Bermon, P. Chaudhari, C. C. Chi, C. D. Tesche, and C. C. Tsuei, *Phys. Rev. Lett.* **55**, 1850 (1985).
408. S. Bermon, *IEEE Trans. Magn.* **MAG-23**, 441 (1987).
409. M. E. Huber, B. Cabrera, M. A. Taber, and R. D. Gardner, *Jpn. J. Appl. Phys.* **26-3**, 1687 (1987).
410. M. S. Turner, E. N. Parker, and T. J. Bogdan, *Phys. Rev. D* **26**, 1296 (1982).
411. B. Cabrera, in *Future Trends in Superconductive Electronics*, B. S. Deaver, Jr., C. M. Falco, J. H. Harris, and S. A. Wolf, eds. (American Institute of Physics, New York), p. 73 (1978).
412. W. M. Fairbank, *Physica* **109 & 110B**, 1404 (1982).
413. M. Odehnal, *Sov. J. Low Temp. Phys.* **11**, 1 (1985).
414. R. A. Webb, *Rev. Sci. Instrum.* **48**, 1585 (1977).
415. M. T. Huiku, T. A. Jyrkkiö, J. M. Kyynäräinen, M. T. Loponen, O. V. Lounasmaa, and A. S. Oja, *J. Low Temp. Phys.* **62**, 433 (1986).
416. M. Kohl, M. Odehnal, V. Petříček, and R. Tichý, in *SQUID '85, Superconducting Quantum Interference Devices and Their Applications*, H. D. Hahlbohm and H. Lübbig, eds. (Walter de Gruyter, Berlin, 1985), p. 879.
417. M. Kohl, M. Odehnal, V. Petříček, R. Tichý, and S. Šafrata, *J. Low Temp. Phys.* **72**, 319 (1988).
418. A. K. M. Wennberg, L. J. Friedman, and H. M. Bozler, in *Proceedings of the 17th International Conference on Low Temperature Physics LT-17*, U. Eckern, A. Schmid, W. Weber, and H. Wühl, eds. (North-Holland, Amsterdam, 1984), p. 265.
419. M. R. Freeman, R. S. Germain, R. C. Richardson, M. L. Roukes, W. J. Gallagher, and M. B. Ketchen, *Appl. Phys. Lett.* **48**, 300 (1986).
420. T. Sleator, E. L. Hahn, C. Hilbert, and J. Clarke, *Phys. Rev. Lett.* **55**, 1742 (1985).
421. T. Sleator, E. L. Hahn, M. B. Heaney, C. Hilbert, and J. Clarke, *Phys. Rev. Lett.* **57**, 2756 (1986).
422. C. Hilbert, J. Clarke, T. Sleator, and E. L. Hahn, *Appl. Phys. Lett.* **47**, 637 (1985).
423. R. Adams, S. P. Potts, J. C. Gallop, and W. J. Radcliffe, in *SQUID '80, Superconducting Quantum Interference Devices and Their Applications*, H. D. Hahlbohm and H. Lübbig, eds. (Walter de Gruyter, Berlin, 1980), p. 509.
424. C. W. F. Everitt, W. M. Fairbank, and W. O. Hamilton, in *Relativity*, M. Carmeli, S. I. Fickler, and L. Witten, eds. (Plenum, New York, 1970), p. 145.

425. C. W. Misner, K. S. Thorne, and J. A. Wheeler, *Gravitation* (Freeman, San Francisco, 1973), p. 1117.
426. J. P. Turneaure, C. W. F. Everitt, B. W. Parkinson, J. T. Anderson, D. Bardas, W. S. Cheung, D. B. DeBra, W. M. Fairbank, R. A. Farnsworth, D. Gill, R. Hacker, G. M. Keiser, J. A. Lipa, J. M. Lockhart, R. A. Van Patten, R. Parmely, R. H. Vassar, and L. S. Young, in *Proceedings of the Fourth Marcel Grossman Meeting On General Relativity*, R. Ruffini, ed. (North-Holland, Amsterdam, 1986), p. 411.
427. J. P. Turneaure, C. W. F. Everitt, B. W. Parkinson, D. Bardas, J. V. Breakwell, S. Buchman, W. S. Cheung, D. E. Davidson, D. B. DeBra, W. M. Fairbank, S. Feteih, D. Gill, R. Hacker, G. M. Keiser, J. M. Lockhart, B. Muhlfelder, R. Parmley, X. Qin, M. Taber, R. A. Van Patten, Y. M. Xiao, and P. Zhou, in *Proceedings of the XXVII COSPAR Symposium on Relativistic Gravitation, Espoo, July 18-29, 1988*, in press.
428. H. Koch, in *Sensors—A Comprehensive Book Series in Eight Volumes*, W. Göbel, J. Hesse, and J. N. Zemel, eds. (VCH Verlagsgesellschaft, Weinheim, 1989); in *Magnetic Sensors*, R. Boll and K. J. Overshott, eds. (VCH Verlagsgesellschaft, Weinheim, 1989), chap. 9.